SNAP THROUGH OF LARGE SHIELD DRIVEN TUNNELS

RESERVE CAPACITY

T.G. van der Waart van Gulik

SNAP THROUGH OF LARGE SHIELD DRIVEN TUNNELS
RESERVE CAPACITY
Main report

T.G. van der Waart van Gulik
1259210

Delft University of Technology
Faculty of Civil Engineering and Geosciences
Section of Concrete Structures and Structural Mechanics
Stevinweg 1
2628 CN Delft

Gemeentewerken Rotterdam
Ingenieursbureau - Civiele Constructies
Galvanistraat 15
3029 AD Rotterdam

Graduation committee

prof. dr. ir. J.C. Walraven	TU Delft
dr. ir. P.C.J. Hoogenboom	TU Delft
dr. ir. C.B.M. Blom	Gemeentewerken Rotterdam / TU Delft
ir. L.J.M. Houben	TU Delft

Rotterdam, December 2010

PREFACE

The research presented in this report is the graduation thesis to obtain my master’s degree in Civil Engineering at Delft University of Technology in the Netherlands. Most work for this thesis was performed at the engineering office of Gemeentewerken Rotterdam.

The main objective of the study was to discover whether or not large shield driven tunnels are more sensitive to snap through than smaller ones. A physical and geometrical non-linear model was used to analyse this subject. Additionally, during this research unexpected but interesting results concerning the segmental thickness were discovered. Moreover, a useful practical procedure to analyse snap through was developed.

To me, it was a nice challenge to analyse snap through, which is a quite unknown mechanical problem for shield driven tunnels.

I would like to thank the engineering office of Gemeentewerken Rotterdam for giving me the opportunity to conduct research at the company. Prior to this research, during the internship at Museumpark as well as during the graduation period, I had a great time.

I would like to thank the members of my graduation committee for their useful comment, which resulted in a higher quality level.

Especially I would like to thank Kees Blom for his personal guidance on the subject and enjoyable informal conversations where he turned out to be a true consultant in general.

Finally, I thank my girlfriend and family for their support and understanding.

Tim van der Waart

SUMMARY

Until the 1990's the commonly used Dutch tunnelling methods were the cut and cover methods and the immersed tunnels. At the same time the Dutch government decided that shield driven tunnelling has a high potential in the crowded Dutch area.

Tunnelling in soft ground conditions with a high water table (like in the Netherlands) generally employs a shield with excavation wheel as standard practice for the purpose of providing a safe working environment for the tunnellers, and for achieving more effective and efficient tunnel excavation. The entire tunnelling operation is done by a TBM (Tunnel Bore Machine).

In 1964 Schulze and Duddeck described ring behaviour of shield driven tunnels by a collection of graphs. These graphs are used to design a shield driven tunnel. The method assumes that the tunnel remains circular and equilibrium of forces is guaranteed at all time. The failure criterion is based on the bending moment capacity. Blom [4] showed that a shield driven tunnel will not collapse after formation of a plastic hinge. Finally, the tunnel becomes unstable as a result of large deformations. This is a very explosive and dangerous failure mechanism which is called snap through. The current design method is only valid if reaching the bending moment capacity is decisive. Since snap through probably becomes more critical in case of large tunnel diameters, the question remains: *"Are shield driven tunnels with large diameters more sensitive to snap through than smaller ones?"*

To answer this question, a physical and geometrical non-linear model was used to analyse different segmented rings surrounded by soil. This model takes into account soil loading, soil support, cracking of segments, yielding of reinforcement and deformations of segments and longitudinal joints. To increase bending moments and trigger snap through, the ovalisation loading is increased by small steps. This was done to find out which mechanism is decisive.

The situation concerning snap through is worse than Blom [4] predicted. The safety factor γ is close to one, instead of $\gamma = 3$ as Blom predicted for the BRT (Botlek Railway Tunnel). However, for different diameters, the γ value varies to some extent. If $\gamma = 1$, it means that snap through and reaching the bending moment capacity occur at the same time. Therefore, a closer look at practical design methods is needed. It turned out that a linear elastic calculation always provides safe results. When non-linear longitudinal joints were added, it is more likely that the analysis provides unsafe results for tunnel diameters larger than 8 meter. Hence, shield driven tunnels with large diameters are more sensitive to snap through than smaller ones. A larger possibility exists that snap through takes place without any plastic hinge.

Secondly, snap through is also influenced by the segmental thickness. The safety factor γ is determined for many cases. Again a closer look at practical design methods is needed, since the reserve capacity is close to the critical point for snap through ($\gamma = 1$) or even smaller. It turned out that a linear elastic calculation provides safe results if $d_{seg} > D_i/40$. When non-linear longitudinal joints were included, the analysis only provides safe results for the interval $1/38 < d_{seg}/D_i < 1/22$. If the segmental thickness over the internal diameter ratio does not fulfil these requirements, the corresponding analysis could provide unsafe results. Additionally, it was possible to determine the optimal segmental thickness. This research part confirms the correctness of the empirical design rule to determine the segmental thickness in relation to the radius. Materials are used most efficient if $d_{seg} \approx D_i/22$.

Despite the wrong results, one can conclude that a linear elastic calculation provides safest results. More awareness of reality is required for everyone who takes into account non-linear longitudinal joints. Since it is not unthinkable that snap through is the decisive failure mechanism, it is very dangerous if one realises that practical methods to analyse a shield driven tunnel will not notice this failure mechanism. The tunnel design is probably based on the wrong criterion.

It takes a lot of time to determine the real load bearing capacity by using the advanced model mentioned above. Therefore, a simple model to analyse snap through is developed.
The model provides qualitative knowledge about the character of snap through and the load bearing capacity influenced by the soil, the segments, the longitudinal joints and the radius of the tunnel. The model is able to indicate quantitative whether or not the tunnel is stable. After calibrating the simple model, it was possible to develop a practical procedure to predict the right snap through inducement and corresponding load bearing capacity in no time.

SAMENVATTING

Tot de jaren 90 waren er in Nederland twee veel toegepaste tunnelmethodes: de zogenaamde ‘cut and cover’ methode en de zinktunnel. In diezelfde tijd bepaalde de Nederlandse overheid dat boortunnels veelbelovend waren in het dichtbevolkte Nederland.

Het maken van boortunnels in zachte grond met een hoge grondwaterstand (zoals in Nederland) vereist meestal een schild met een graafwiel als basisuitrusting. Naast het feit dat dit moet leiden tot een veilige werkomgeving voor de bouwvakkers, is het ook bedoeld om effectiever en efficiënter te ontgraven. Het gehele tunnelbouwproces wordt uitgevoerd met behulp van een TBM (tunnelboormachine).

In 1964 ontwierpen Schulze en Duddeck een aantal grafieken waarmee het gedrag van boortunnels (gemaakt met behulp van een schild) beschreven kon worden. Deze methode veronderstelt dat de tunnel rond blijft en dat krachtenevenwicht altijd gegarandeerd is. Het bezwijkcriterium is gebaseerd op het ontstaan van een plastisch moment in de lining. Blom [4] heeft laten zien dat een boortunnel niet instort na het ontstaan van een plastisch scharnier. Uiteindelijk zal de tunnel bezwijken door instabiliteit, ten gevolge van grote vervormingen. Dit zeer explosieve en gevaarlijke bezwijkmechanisme wordt doorklappen genoemd. De huidige ontwerpmethode is alleen geldig wanneer het bereiken van het plastisch moment ook maatgevend is. Het doorklapmechanisme wordt waarschijnlijk steeds kritischer wanneer tunnels een grotere diameter krijgen. De onderzoeksvraag is dan ook:
“Zijn boortunnels met een grote diameter gevoeliger voor doorklappen dan kleine boortunnels?”

Om deze vraag te kunnen beantwoorden is een fysisch en geometrisch niet lineair model gebruikt om verschillende gesegmenteerde ringen omgeven door grond te analyseren.
Dit model houdt rekening met grondbelasting, ondersteuning door de grond, scheuren van het beton, vloeien van de wapening en vervormingen van de segmenten en de langsvoegen. Om het buigend moment te verhogen en doorklappen te ‘prikkelen’ is de ovaliserende belasting stapsgewijs opgevoerd. Deze werkwijze is toegepast om te kunnen bepalen welk mechanisme maatgevend is.

De situatie met betrekking tot doorklappen is erger dan Blom [4] voorspelde. Hoewel de veiligheidsfactor γ varieert voor de verschillende onderzochte diameters, liggen wel al deze waardes relatief dicht bij één, in plaats van $\gamma = 3$ zoals Blom voorspelde voor de BRT (Botlek spoortunnel). Als $\gamma = 1$, dan klapt de tunnel door op moment dat ook een plastisch scharnier ontstaat. Daarom is het nodig om de praktische ontwerpmethodes nader te beschouwen. Het blijkt dat een lineair elastische berekening altijd voor veilige resultaten zorgt. Als er niet lineaire langsvoegen worden toegevoegd, dan is het meer aannemelijk dat de analyse resulteert in onveilige uitkomsten voor tunnels met een diameter groter dan 8 meter. Dus, boortunnels met grote diameters zijn gevoeliger voor doorklappen dan kleine boortunnels. De kans is groter dat doorklappen optreedt zonder dat er een plastisch scharnier ontstaan is.

Daarnaast wordt doorklappen ook beïnvloed door de dikte van de segmenten (lining). De veiligheidsfactor γ is bepaald voor veel verschillende gevallen. Ook nu is het noodzakelijk om de praktische ontwerpmethodes nader te beschouwen, aangezien de reserve capaciteit erg dicht bij het kritische punt voor doorklappen ligt, of er zelfs onder. Het blijkt dat een lineair elastische berekening altijd veilige resultaten geeft als $d_{seg} > D_i / 40$. Wanneer niet lineaire langsvoegen worden toegevoegd, dan blijkt dat de analyse alleen veilige resultaten geeft als voldaan wordt aan de voorwaarde: $1/38 < d_{seg} / D_i < 1/22$. Deze twee praktische analyses

kunnen onveilige uitkomsten geven als de verhouding tussen de dikte van het segment en de diameter niet voldoet aan de bijbehorende voorwaarde. Daarnaast heeft dit deel van het onderzoek ook geleid tot het vaststellen van de optimale dikte van de segmenten. De juistheid van de empirische vuistregel om de dikte van het segment te bepalen als ratio van de diameter is aangetoond. De materialen worden het meest efficiënt gebruikt als $d_{seg} \approx D_i/22$.

Ondanks de onjuiste resultaten kan er worden geconcludeerd dat de lineair elastische berekening de veiligste resultaten oplevert. Meer bewustzijn van de realiteit is noodzakelijk voor iedereen die niet lineaire langsvoegen meeneemt in de berekening. Omdat het in dit geval niet ondenkbaar is dat doorklappen het maatgevende bezwijkmechanisme van een boortunnel is, is het gevaarlijk om deze praktische methode te gebruiken, aangezien doorklappen niet opgemerkt wordt. In dit geval bestaat de kans dat het ontwerp van een boortunnel gebaseerd is op het verkeerde criterium.

Wanneer het hierboven beschreven geavanceerde computermodel gebruikt wordt, neemt het veel tijd in beslag om de maximale belasting die de constructie kan dragen te bepalen. Daarom is een eenvoudig model ontwikkeld om doorklappen van boortunnels te kunnen analyseren. Dit model levert kwalitatieve kennis over het karakter van het doorklappen en de maximaal opneembare belasting die beide worden beïnvloed door de grond, de segmenten, de langsvoegen en de radius van de tunnel. Dit model is kwantitatief in staat om aan te geven of een boortunnel al dan niet stabiel is. Na het kalibreren van dit eenvoudige model was het mogelijk om een praktische procedure te beschrijven waardoor de juiste aanleiding van doorklappen en bijbehorende maximale opneembare belasting kunnen worden bepaald in zeer korte tijd.

TABLE OF CONTENTS

1 INTRODUCTION

1.1 Introduction to shield driven tunnels

1.1.1 History

Until the 1990's the commonly used Dutch tunnelling methods were the cut and cover methods and the immersed tunnels. At the same time the Dutch government decided that shield driven tunnelling has a high potential in the crowded Dutch area. There are almost no surface disturbances by construction. The bored tunnel, and especially the shield tunnelling, was an addition to the traditional construction methods. Today's tunnelling practice shows that shield driven tunnelling is well-applicable in the Dutch soft grounds with high water tables. Tunnelling in soft ground conditions with a high water table (like in the Netherlands) generally employs a shield with excavation wheel as standard practice for the purpose of providing a safe working environment for the tunnellers, and for achieving more effective and efficient tunnel excavation.

1.1.2 Tunnelling process

Essential aspects of basic tunnelling operation is ground excavation coupled with immediate control of the tunnel face and ground around the tunnel periphery by effective support, followed by removal of the excavated ground and erection of the permanent system (the lining). This tunnelling operation is done by a TBM (Tunnel Bore Machine, figure 1.1). At the front of the TBM the soil is excavated by the cutter wheel. The soil is removed by means of a worm wheel and conveyer belt. The shield of the TBM is a conical shaped steel cylinder and is pushed forward by hydraulic rams (jacks) which counteract on the lining. The tail void should be promptly filled with pea gravel and/or grout in order to maintain effective ground control. Since the TBM diameter is larger than the tunnel diameter, grout must be injected to prevent soil movement towards the tunnel that causes soil disturbances and settlements to the environment. When the TBM has axially advanced over a distance of a ring width (generally 1.5 to 2 m) a space is available in which a new ring can be erected. Several jacks are released to provide space for a new segment of the ring. The erector lifts the segment towards its final position, where the jacks are released. When the segment is secured by bolts, the jacks elongate until the newly placed segment is clamped. In a sequence all new segments are erected and a new ring is built. At this moment, the excavation process starts over again. The segmental supply is arranged from the start shaft through the tunnel part that is already constructed by use of small-track trains or especially designed cargo trucks. At the rear of the TBM the segments are lifted by a crane and transported to the erector. On the next page, in figure 1.2, some shield tunnelling definitions are shown.

Figure 1.1 – Closed shield TBM with excavation wheel.

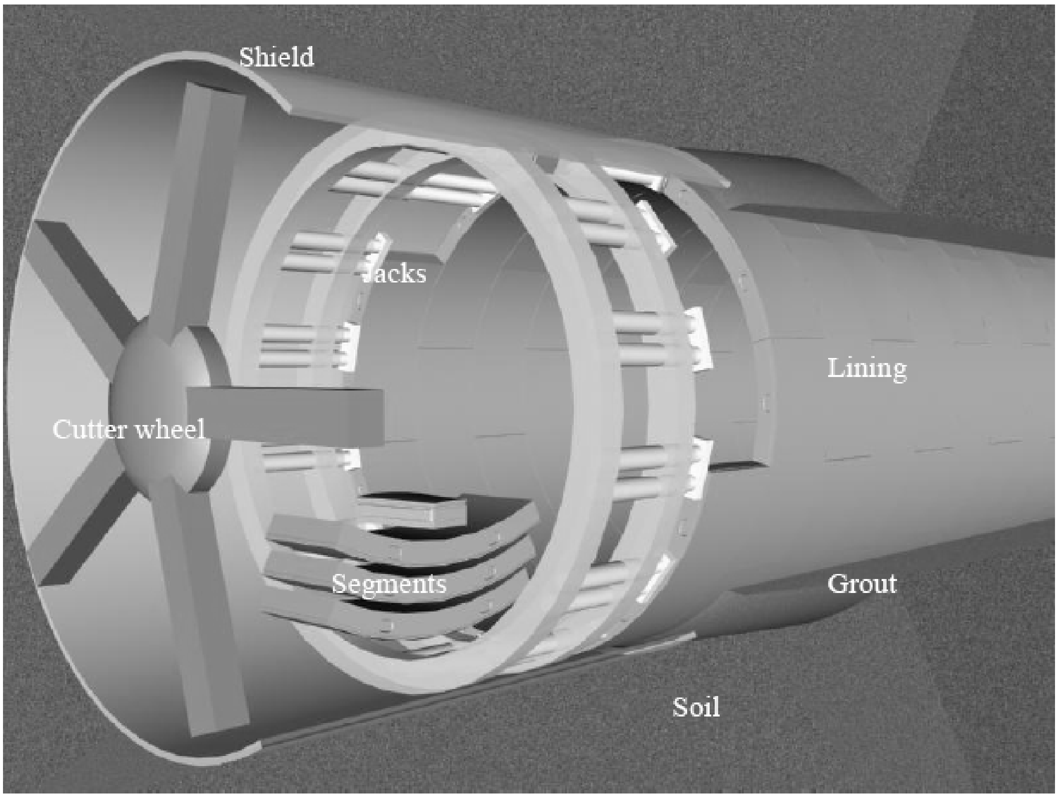

Figure 1.2 – Shield tunnelling definitions.

1.2 Problem description

In 1964 Schulze and Duddeck described ring behaviour of shield driven tunnels by a collection of graphs (figure 1.3 and 1.4). By means of these design graphs bending moments and normal forces could be retrieved for various depth projections of the tunnel and various ratios between the tunnel stiffness and soil stiffness.

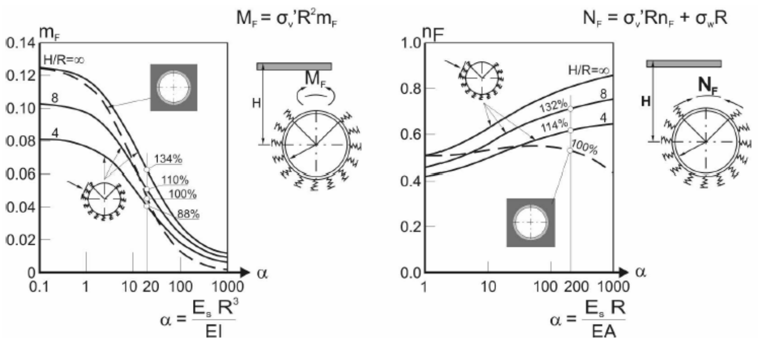

Figure 1.3 – Design diagrams for tangential bending moments and normal forces in case of bond (tangential support)

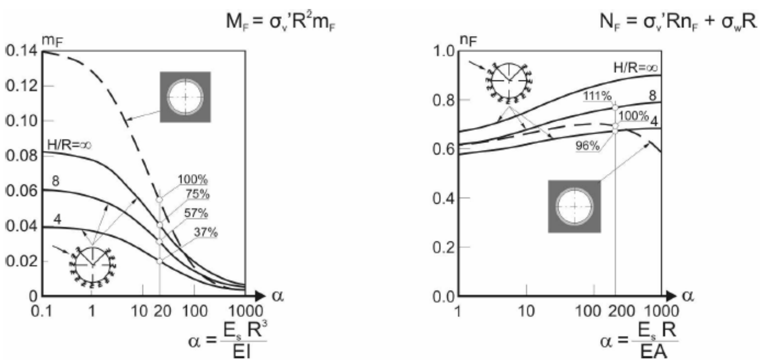

Figure 1.4 – Design diagrams for tangential bending moments and normal forces in case of no bond (no tangential support)

These design graphs are still used in practice. In practice a rule of thumb is used as well to determine the segmental thickness. This is an empirical “design rule”.

$$d_{seg} = \frac{1}{20} D_i$$

One twentieth times the tunnel’s internal diameter is a rule of thumb to calculate the segmental thickness, simply because it works very well. The design graphs presented by figure 1.3 and 1.4 in combination with this rule of thumb result in the required amount of reinforcement. A calculation of the cross-section in ultimate limit state results in the bending moment capacity, which is called the plastic moment ($M_{ULS} = M_p$). Nowadays, the bending moment capacity is still the failure criterion for a shield driven tunnel design ($M_{design} < M_p$).

This design method is based on the assumption that equilibrium is always guaranteed (no stability problems). According to this method, the ‘Ketel’ formula is always valid since the tunnel remains circular. Therefore, from a stability point of view the assumption is made that the tunnel is able to carry the normal force (hoop force) due to soil loading at all time. Since this method is based on a linear elastic (LE) calculation, one assumes that the results are always safe.

The question pops up whether or not these assumptions are right. Imagine the situation in which the tunnel can not carry the tangential normal force. The tunnel would collapse! A heavily deformed tunnel (not circular anymore) is a scenario in which the tunnel rings are not able to carry the normal force. This failure mechanism is called snap through (figure 1.5), which is introduced by Blom [4].

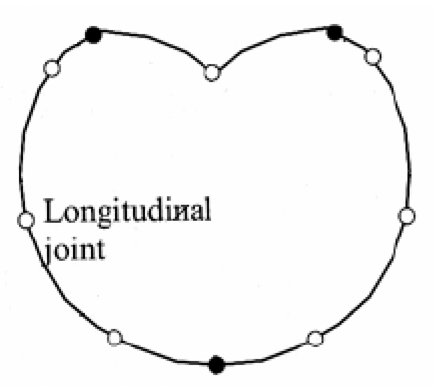

Figure 1.5 – Snap through

The real behaviour of a structure is normally less stiff than a linear elastic calculation presents. Hence, for a certain loading, the real deformation is much more than the linear elastic calculation presents. Figure 1.6 shows the real stiffness behaviour for a structure in general and the stiffness behaviour according to the linear elastic calculation method. The absolute maximum load for this structure is indicated by $F_{\max,reality}$ (big dot).

The next question comes up whether or not the hypothetical failure mechanism (figure 1.5) can occur in reality. And, immediately the third question arises: If snap through is a possible failure mechanism, is it also a decisive failure? Blom [4] elaborated a second order elasto-plastic calculation for the Botlek Railway Tunnel (BRT) with a more or less hypothetical loading case. He showed that snap through is a possible failure. The ring will not collapse after formation of the first plastic hinge. The load can be increased by a factor three before snap through occurs. Hence, the load bearing capacity of the structure is three times higher than the load corresponding to the formation of the first plastic hinge. One can conclude that snap through is a possible failure mechanism, but not decisive in this specific case (BRT).

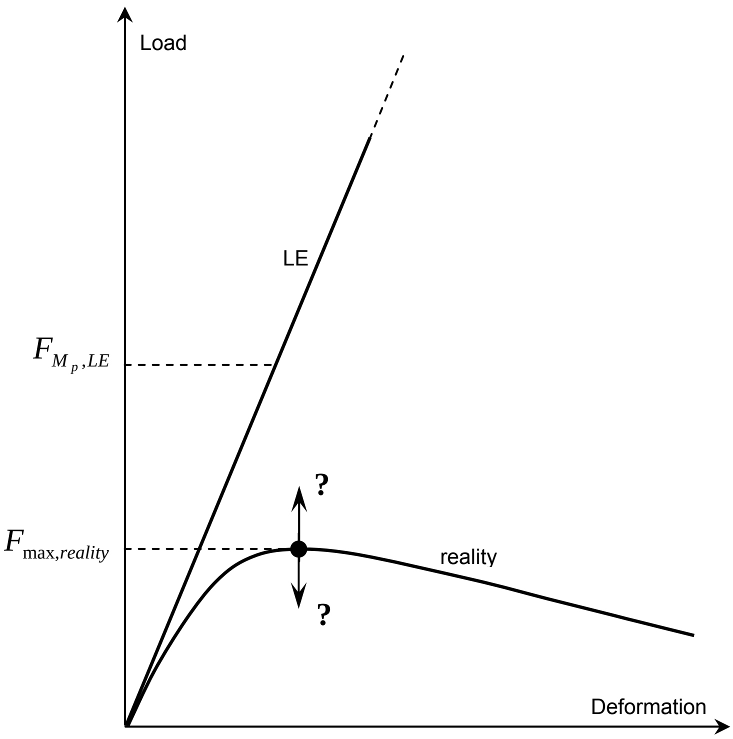

Figure 1.6 – Linear elastic vs real behaviour. This situation indicates danger, since $F_{max,reality} < F_{M_p,LE}$.

The corresponding literature study [7] presented the 'shape' of the soil loading. The total load is a superposition of the uniform loading σ_0 and the ovalisation loading σ_2. According to the design method mentioned above, bending moments were caused by the ovalisation loading only. By an arbitrary choice for σ_0 a certain value for σ_2 is needed to reach the bending moment capacity (M_p). Blom [4] chose an initial value for σ_0 arbitrarily and increased σ_0 as well as σ_2 in small steps to discover whether or not the bending moment capacity is reached at an earlier load stage than snap through ($\sigma_{2,M_p} < \sigma_{2,snap\ through}$?). Since the bending moment capacity is the failure criterion, this must be true, without consideration whether or not the values for σ_0 and σ_2 are realistic. If not, the design rules are not valid anymore (unsafe).

From the corresponding literature study [7] one can conclude that almost no knowledge about snap through of shield driven tunnels is available. Only Blom's [4] hypothetical loading case makes one aware of this failure, though it was not decisive.

In modern world everything becomes larger, also tunnel diameters. This development of decreasing curvatures makes the snap through case probably even more dangerous. One supposes that tunnels with larger diameters are more sensitive to snap through than smaller ones. When larger tunnels were built, at a certain moment the increasing horizontal diameter and normal force will execute the explosive failure of snap through before the first plastic hinge evolves ($\sigma_{2,snap\ through} < \sigma_{2,M_p}$, illustrated by figure 1.6). This mechanism does not warn the surrounding people for collapse; suddenly it happens.

1.3 Problem definition

Snap through of shield driven tunnels is a relatively "new and dangerous" failure mechanism and will probably be more critical when tunnel diameter increases. At some point it will be the decisive failure of a shield driven tunnel. The question remains: "*Are shield driven tunnels with large diameters more sensitive to snap through than smaller ones?*"

1.4 Objective

The objective of this research is to *discover whether or not large shield driven tunnels are more sensitive to snap through than smaller ones.*

1.5 Outline of this report

Chapter 1 briefly explained what a shield driven tunnel actually is. Moreover, a likely shortcoming of the design rules with respect to snap through is explained in paragraph 1.2. Chapter 2 briefly introduces some parameters which influence the structural behaviour of the tunnel. The research framework is given as well. Chapter 3 presents an explanation of the model which is used to study snap through. Actually, an explanation is given on how to find the real load bearing capacity of a shield driven tunnel. An illustration of this value is given in figure 1.6; $F_{\max,reality}$. All structural parts are described separately. Finally, a validation for the model concerning the concrete segments is given. Chapter 4 shows the results for the normal force, the bending moment and the relation between load and displacement. Afterwards, a clarification for these results is presented. Paragraph 4.4 describes the importance of analysing snap through in relation to the radius. Paragraph 4.5 explains the reserve capacity concerning engineering practice. The last paragraph of chapter 4 answers the research question mentioned in paragraph 1.3. Chapter 5 is about the most interesting parameter for a shield driven tunnel: the segmental thickness. This parameter is analysed similarly to the analysis in paragraph 4.4 and 4.5. Furthermore, the most efficient value for the segmental thickness related to the radius is determined. Chapter 6 is a simplification of the model explained in chapter 3. First, a simple model is developed. Secondly, the influence of several parameters on snap through will be analysed. Finally, a clear practical procedure to consider snap through is introduced. Chapter 7 gives an overall conclusion and recommendations from several perspectives. In the end, all references as well as five appendices which are directly or indirectly related to this research are presented.

Keywords: shield driven tunnel, snap through, reserve capacity, radius, segmental thickness.

2 SYSTEM BOUNDARIES

2.1 Parameters

Radius

The radius of the tunnel is the most important parameter for this research. If the radius of a tunnel increases, the curvature decreases. This probably implies that the lining becomes more sensitive to snap through failure.

Stiffness ratio between the soil and the concrete lining

A tunnel is mainly loaded by soil and water pressure. Since these loads differ around the ring, bending occurs, which causes ovalisation. Shield driven tunnels are very sensitive to this ovalisation pressure. Relatively small load differences in comparison with the uniform pressure bring on huge bending moments and deformations. The stiffness ratio between the soil and the concrete is highly important in this case. When the soil is relatively stiff it attracts more (ovalisation) load, which reduces the bending moment in the ring and increases the normal force. When the soil is relatively weak, it is just the other way around. Regardless the stiffness ratio, the ground at the sides of the tunnel will always have a positive influence on the ring behaviour. In case of ring support (by the surrounding soil), the ovalisation loading which causes the first plastic hinge, is seven times larger than in the case without support (40% versus 6% of the uniform loading, in both cases acting on a single segmented ring). If stability is not an issue, the compressive stresses become critical. This can be explained by the fact that the ring loses stiffness due to the plastic hinges. The soil becomes relatively stiff and starts to compensate the ovalisation loading and only normal forces remain. [8]

Compressive strength

If the compressive strength increases, the cross-section can sustain higher stresses. Therefore, the bending moment capacity increases. Since there is a positive correlation between the compressive strength and the Young's modulus, the Young's modulus will increase too. The stiffer cross-section will attract more forces from now. It turns out that if the capacity of the cross section increases, the bending moments increase even more. Hence, increasing the compressive strength has a negative influence on safety [1]. However, the bending moment capacity is reached at an earlier load stage. Therefore, there is less chance that snap through will occur as decisive failure.

Longitudinal joints

These joints are in between the segments and weaken the bending stiffness of the homogeneous ring. Janβen developed a method to describe the rotational stiffness of the longitudinal joints. As long as the stress due to the compressive normal force (hoop force) is larger than the maximum stress caused by bending moment, the rotational stiffness is constant and the joint is closed.

$$c_r = \frac{b l_t^2 E_c}{12} \qquad \text{under the condition that} \qquad \theta \leq \frac{2N}{E_c b l_t}$$

A gap will develop if the normal force is out of the neutral force centre. The developed tensile stresses due to the bending moments exceed the compression stresses due to the normal forces. If this is happening, a gap develops and the rotational stiffness will also depend on the rotation itself and becomes non-linear. The bending stiffness of the ring reduces even more.

$$c_r = \frac{9bl_tE_c\left(\frac{2M}{Nl_t}-1\right)^2}{8N}M \qquad \text{under the condition that} \qquad \theta > \frac{2N}{E_cbl_t}$$

It is obvious that the bending stiffness of a homogeneous ring also depends on the number of longitudinal joints (n). Every joint is a weak spot in the ring; more joints means less bending stiffness.

Angle of support
Since the ovalisation loading causes bending moments, the horizontal diameter increases (lying egg). Therefore, the soil at the sides of the tunnel is compressed and will support the tunnel rings. Since the ovalisation loading is dominant for the radial deformations, the points for which the sign of the deformation changes are about $45°$ above and below the sides of the ring. The ground supports the ring over an angle of approximately $90°$ at both sides. The angle of soil support is quite important since the soil (stiffness) has a lot of influence on structural behaviour of the ring.

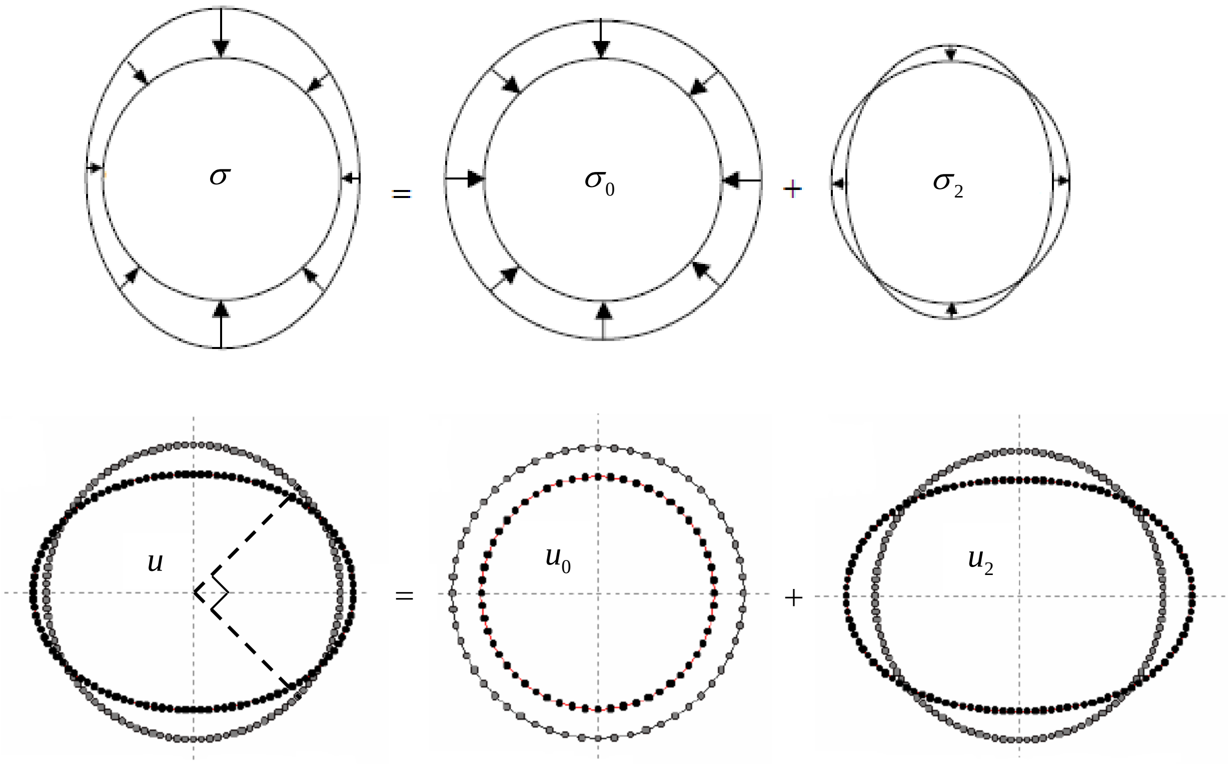

Figure 2.1 – Load on tunnel ring (upper part) and deformations of the tunnel ring due to the load (lower part).

Loading
The uniform loading (σ_0) causes normal forces ('hoop' forces). Due to these normal forces the ring shrinks a bit, but stays circular (see u_0 , figure 2.1). The ovalisation loading (σ_2) causes bending moments. Due to this load the ring starts to bend and gets an oval shape (see u_2 , figure 2.1). If the ovalisation loading increases, the horizontal diameter of the oval increases as well and simultaneously the curvatures at the top and bottom decrease. At a certain moment, snap through takes place (with or without plastic hinges). If the uniform loading increases too, the negative effect of the ovalisation loading reduces a bit, since there is extra pressure at the sides of the ring to maintain a circular shape. In order to study snap

through (real load bearing capacity) in relation to the failure criterion according to the current design rules, the uniform loading is constant (chosen arbitrarily) and the ovalisation loading increases stepwise.

2.2 Botlek Railway Tunnel (BRT)

This report has been written based on the recommendations of Groeneweg [6], Blom [4] and Consortium DC-COB [1]. Since Blom and Consortium DC-COB both considered the BRT to analyse the subject of snap through, the BRT configuration will be used again in order to answer the research question mentioned in paragraph 1.3. The radius will be varied several times to find out the influence on snap through. Three different tunnels will be studied: $r = 0.5r_{BRT}$, $r = r_{BRT}$, $r = 2r_{BRT}$. All parameters which depend on the radius change proportionally (table 4.1). To ensure consistency, the model created by Blom [3] is used partly in this research. The BRT is characterised by the parameters presented in table 2.1.

l_t	$0.170m$
b_{joint}	$1.388m$
n	7 segments
$D_{internal}$	$8.65m$
$d_{seg} \approx R/10$	$0.4m$
$b_{segment}$	$1.5m$
$\alpha_{bedding}$	$90°$
σ_0	$0.5MPa$
$\Delta\sigma_2$	$0.05MPa$
$\omega_0 = \omega_{0,\min}$	0.18%
E_{oed}	$38MPa$
Concrete strength	*B45*

Table 2.1 – Important BRT parameters

3 MODELLING OF RING BEHAVIOUR SURROUNDED BY SOIL

3.1 Introduction

The soil surrounding the tunnel has certain stiffness, just like the concrete lining itself. Stiff parts attract bending moments. Consequently the tunnel and soil will cooperate to bear all loads. These loads result from the soil's mass and ground water pressure surrounding the shield driven tunnel.

From literature [5] it is known that shear forces are of minor influence in a circular shield driven tunnel and will not turn out to be governing. Since the (combination of) tangential bending moments and tangential normal (or 'hoop') forces are governing for the structural behaviour in a ring, the focus of this research will be on these forces.

In 1964 Schulze and Duddeck described ring behaviour of shield driven tunnels by a collection of graphs. By means of those design graphs bending moments and normal forces could be retrieved for various depth projections of the tunnel and various ratios between the tunnel stiffness and soil stiffness. When computers developed and the time needed for more comprehensive calculations decreased, the creation of models especially designed for one tunnelling project grew popular. The main difference in the models created by now is the modelling of the soil. In finite element models, soil is normally introduced as a continuum around the tunnel lining. In more uncomplicated framework analyses the soil has been reduced to springs and loads representing the supporting and loading effects of the soil on the tunnel lining (paragraph 3.4). This model focuses on the tunnel structure only; the developments of deformations and stresses in the surrounding soil are omitted. Finite element models however are able to return these soil results as well.

Modelling of the tunnel lining itself can be realized by reducing the ring to a homogenous ring beam, a segmented single ring beam or a segmented double ring beam. The homogeneous ring beam is most simplified, but ignores peak moments which develop in the lining due to the presence of longitudinal joints and ring joints. It also ignores the large concentrated rotations in the longitudinal joint, which are important for the snap through behaviour. The segmented single ring beam model takes care of the longitudinal joints as well. This model is valid if no axial normal forces are present. Hence, no interaction between rings occurs via the contact areas in the ring joints. But, as a consequence of the masonry layout of the segments, the deformations of the adjoining rings will always differ, even when the loading on both rings is the same. Therefore, the so-called dowel and socket system is activated, resulting in very high stress spots that cause damage to the concrete. When segments damage, the rings are less connected and will act more like single rings. Since it takes very large deformations to activate the snap through mechanism [7], it is assumed that these deformations damage the segments so much, that no interaction between the rings is possible anymore. The segmented double ring beam model introduces the effects of both longitudinal joints and interacting ring joints in the calculation. However, the most appropriate way to answer the research question is using the segmented single ring beam model.

In the paragraphs 3.2, 3.3 and 3.4 the creation of a segmented single ring beam model with soil interaction represented by loads and springs will be described. This model focuses on the tunnel structure. Paragraph 3.5 is about the validation of the model for the reinforced concrete segments.

The software application Scia Engineer 2009.0 is used to process the framework analysis from this study.

3.2 Reinforced concrete tunnel segments

The geometry of the segments is represented by so-called beam elements. The span of these beams is projected in between the longitudinal joints at both ends. Since these elements are straight by definition, a maximum number of elements is connected to simulate the curved shape of the segments. This optimised geometry of 84 beam elements generates most accurate displacements and internal forces. To model the bending stiffness of the reinforced concrete segments, every beam element is extended by a non-linear rotational spring (figure 3.1). This spring is able to model cracking, plasticity of the concrete compressive zone and yielding of the reinforcement. The bending stiffness of the beam elements itself is extremely high. As usually, the axial stiffness is modelled by the beam elements. Hence, the beam elements have a very high moment of inertia, but a normal Young's modulus and normal cross-sectional area.

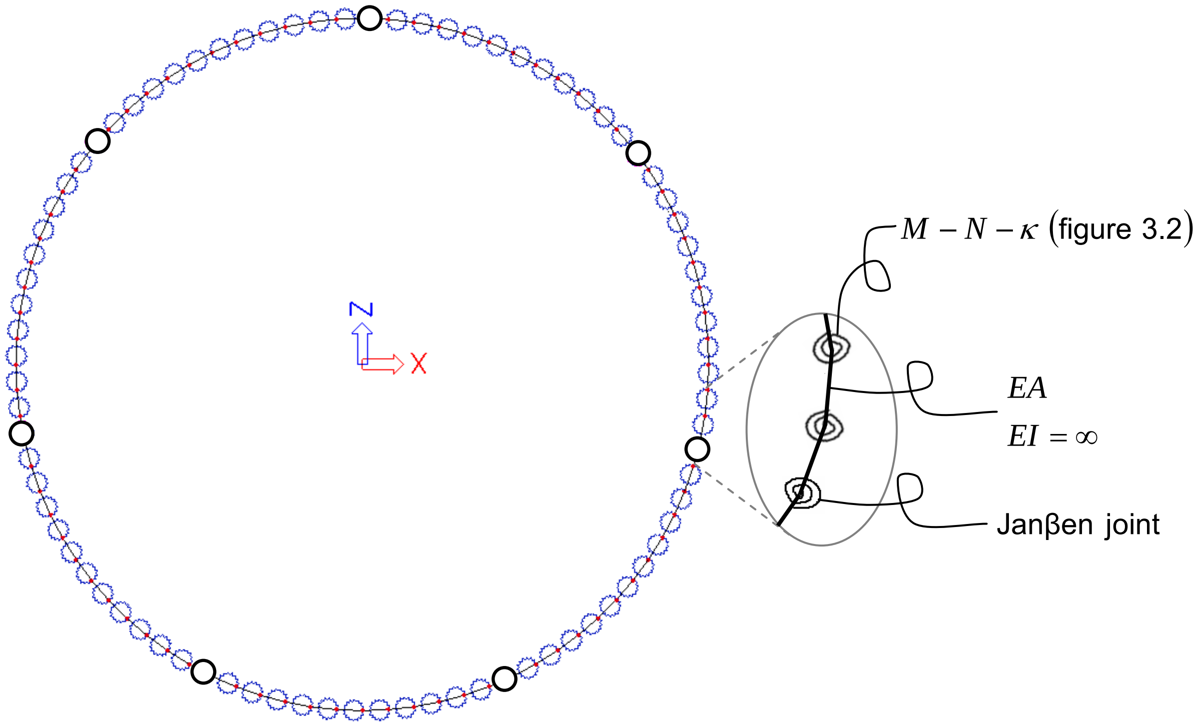

Figure 3.1 – Every beam element is extended by a rotational spring (blue circle). The black circles are Janβen joints.

With respect to this research, this framework analysis is the most time efficient way to model the reinforced concrete segments. The computational modelling is relatively easy and the calculation time is relatively low. During the calculation only iterations are necessary to take into account the geometrical non-linearity. The physical non-linearity is represented by the rotational springs. The adaptability of this model is very time efficient too. Almost any transformation of the model is possible by changing only a few numbers. Especially for this research, in which a lot of geometries must be analysed, it is required to use a time efficient and clear model like this.

Beam elements
The axial stiffness (EA) of the beam elements is defined by the Young's modulus and the cross-sectional area.

$$\left.\begin{aligned} E &= 22250 + 250 f'_{ck} = 22250 + 250 * 45 = 33500 N/mm^2 \\ A &= bh = 1000 * 400 = 400000 mm^2 = 0.4 m^2 \end{aligned}\right\} EA = 33500 * 400000 = 1.34 \cdot 10^{10}\, N$$

As mentioned before, the bending stiffness (EI) of the beam elements is extremely high since the moment of inertia is very high. The only way to obtain this, without changing the axial stiffness, is to find another combination of the segmental width and height, provided a cross-sectional area of $0.4m^2$. A very easy and practical solution is dividing the width by 10 and multiplying the height by 10. The moment of inertia is proportional with the height to the power three. Therefore, the bending stiffness increases with a factor: $1/10 * 10^3 = 100$. The next calculation is given to illustrate the possibility to obtain a relatively high bending stiffness without changing the axial stiffness.

$$I = \frac{1}{12} bh^3 = \frac{1}{12} * 1000 * 400^3 = 5.33 \cdot 10^9\, Nmm^4$$

Replaced by: $I = \frac{1}{12}\left(b/10\right)\left(10h\right)^3 = \frac{1}{12} * \left(1000/10\right) * \left(400 * 10\right)^3 = 5.33 \cdot 10^{11}\, Nmm^4$

$$A = bh = 1000 * 400 = 400000 mm^2 = 0.4 m^2$$

Replaced by: $A = \left(b/10\right)\left(10h\right) = \left(1000/10\right) * \left(400 * 10\right) = 400000 mm^2 = 0.4 m^2$

Non-linear rotational spring elements
The rotational springs represent the bending stiffness of the reinforced concrete segments. The cross-sectional parameters are very important in this case.

$$M = EI\kappa$$

This well-known constitutive equation is able to describe this behaviour in general. Since a non-linear constitutive relation is needed for this research, underneath a $M - \kappa$ diagram for a constant normal force is presented. This cross-section calculation will provide more understanding about the non-linear bending stiffness of the segments. In general a $M - N - \kappa$ comprises four straight lines. The break points of the line are characteristic situations.

- The concrete starts to crack (M_r and κ_r).
- The reinforcement starts to yield (M_y and κ_y).
- Plasticity starts to develop in the concrete compressive zone (M_c, κ_c, $\varepsilon_c = 1.75 \cdot 10^{-3}$).
- The ultimate limit state (M_{cu}, κ_{cu}, $\varepsilon_c = \varepsilon_{cu} = 3.5 \cdot 10^{-3}$).

By using the $M - N - \kappa$ diagram one is able to calculate the bending stiffness in every situation. The bending stiffness decreases when the load increases. The reason for this is the increasing crack pattern and yielding of the reinforcement at a certain moment. Especially in this case, four situations must be analysed to determine the $M - N - \kappa$ diagram.

1) The fibre with the highest tensile stress; $\sigma_c = 0N/mm^2$.

2) The reinforcement on the tensile side of the cross-section; $\sigma_{s1} = 0N/mm^2$.

3) The design value for the compressive strength has been reached ($\varepsilon_c = 1.75 \cdot 10^{-3}$).

4) The ultimate limit state of the compressive zone has been reached ($\varepsilon_{cu} = 3.5 \cdot 10^{-3}$).

The $M - N - \kappa$ diagram is carried out for the BRT for example. An elaboration is given in appendix C. The final result, the $M - N - \kappa$ diagram, is shown in figure 3.2. The rotational springs, which are added to every beam element, are based on figure 3.2. But, the input must be a $M - \theta$ relation (bending moment versus rotation). Therefore, κ is integrated over the length of one beam element.

To simulate the changing normal force, several calculations, all with a different constant normal force, will be performed. Reality is a combination of these calculations.

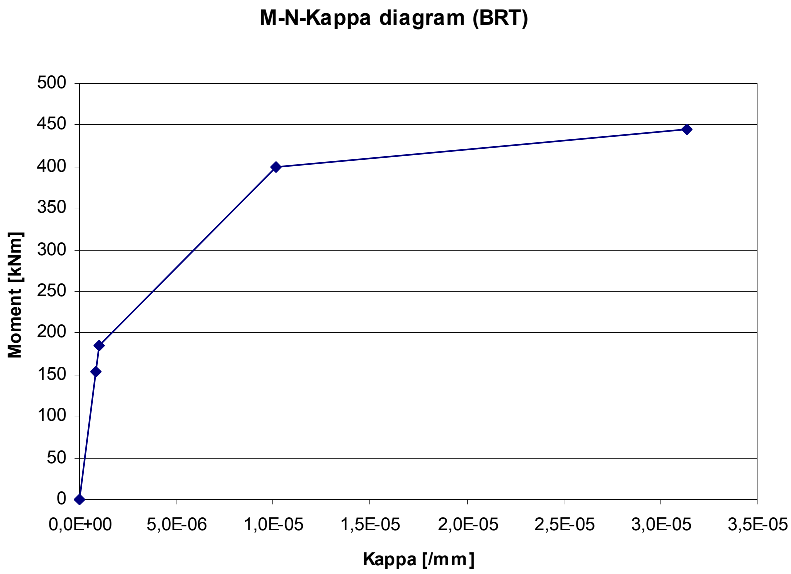

Figure 3.2 – M - N - κ relation with a constant normal force of 2262.5kN (BRT).

3.3 Longitudinal joints

As mentioned before, the structural behaviour of the ring in the soil depends strongly on the stiffness of the ring. Since the longitudinal joints are weak discontinuities in the ring; the joints influence the ring's structural behaviour. Hence, the longitudinal joints, which are in between two segments, bring on reduced stiffness compared to the homogeneous ring.

The joint transfers a bending moment and a normal force by contact. The joint is unable to transfer tensile forces since the segments are not physically connected. The normal force prevents opening of the joint to some extend. However, in case of a relative high bending moment the joint will open. As a result, the stiffness of the joint is reduced. Modelling of a contact area usually means longer calculation time, which is undesirable. The model itself requires a lot of input time as well.

A simplified solution has been presented by Janβen. The contact problem is reduced to the problem of a beam, which is unable to cope with tensile stresses. The depth of the beam equals the width of the joint (segmental width) and the height and width of the beam are both equal to the joint's contact height. The contact behaviour in the longitudinal joint (also called Janβen joint) can be described by a simple non-linear rotational spring, which is more common and requires much less modelling and calculation time. The relation between rotation, bending moment and normal force is determined analytically. Next, this relation is translated into a spring stiffness of the rotational spring. An elaboration is given in appendix D. The analytical solution for the rotational stiffness is expressed by two formulas, each corresponding to a specific situation. Figure 3.3 shows a $M-\theta$ relation of a Janβen joint for the BRT.

1) As long as the stress due to the compressive normal force (hoop force) is larger than the maximum stress due to the bending moment, the rotational stiffness is constant and the joint is closed. Hence, there is no gap in the joint: the rotational stiffness is constant (not depending on the occurring rotation in the joint).

$$c_r = \frac{b l_t^2 E_c}{12} \qquad \text{under the condition that} \qquad \theta \le \frac{2N}{E_c b l_t}$$

2) A gap will develop if the normal force is out of the neutral force centre of the joint's cross-section. The developed tensile stress due to the bending moment exceeds the compression stress due to the normal force. If this is happening, a gap starts to develop and the rotational stiffness will also depend on the rotation itself and becomes non-linear. The bending stiffness of the ring reduces even more. Hence, there is a gap in the joint: the rotational stiffness is reducing as a function of the rotation.

$$c_r = \frac{9 b l_t E_c \left(\frac{2M}{N l_t} - 1\right)^2}{8N} M \qquad \text{under the condition that} \qquad \theta > \frac{2N}{E_c b l_t}$$

Where:	c_r	=	rotational stiffness
	b	=	width of the contact area of the joint (segmental width)
	l_t	=	height of the contact area of the joint
	E_c	=	Young's modulus of the concrete
	M	=	bending moment
	N	=	normal force
	θ	=	rotation in the joint

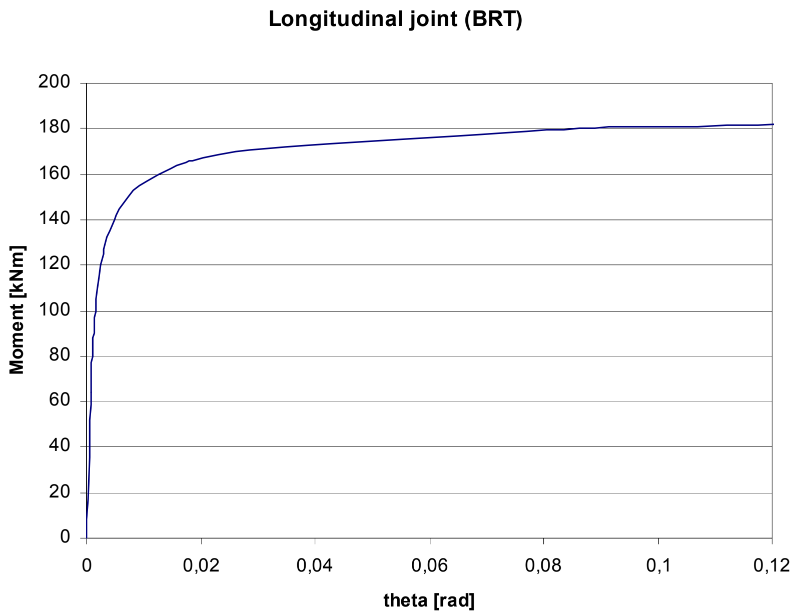

Figure 3.3 – Janβen joint with a constant normal force of 2262.5kN (BRT).

In theory it is possible that the second stage pass into a third stage in which the concrete in the joint becomes plastic. Most studies only take into account the first two stages. Moreover, when the second stage goes on (the rotation increases without consideration of plasticity), it describes almost the plastic behaviour of the third stage. The second stage acts a little bit too stiff, but the difference is unimportant.

Obviously the Janβen method only focuses on the transfer of bending moments in the joint. Normal forces and shear forces are transmitted in a far more straightforward way. Provided that the joint is subjected to a pure compressive normal force the joint will not be noticed at all. The normal force is simply transferred from one tunnel segment to the other. The joint itself will not shrink by the compressive force since the influence zone is relatively small. The shear force is transferred by friction in the joint. The maximum shear force that can be transferred depends on the normal force and the contact surface of the joint. It is assumed that there is enough friction at all time to transfer the shear force.

$$F_f = \mu_s * F_N$$

This is a simple formula to determine the maximum shear force that can be transferred.

Where: F_f = maximum shear force that can be transferred by friction

μ_s = static friction coefficient between two concrete surfaces (≈ 0.6)

F_N = The normal force in the Janβen joint.

For the BRT the normal force varies between 2300kN and 4200kN. Consequently the maximum shear force that can be transferred roughly varies between 1400kN and 2500kN. Since the maximum acting shear force is much smaller than these values, there is no problem at all by transferring it from one segment to the other.

In the end, a longitudinal joint can be modelled by a rotational spring only (Janβen characteristics). The normal force as well as the shear force is transferred by connecting two beam elements to each other at places where a Janβen joint is situated. This will result in a stiff connection. Every ring of the BRT has seven segments and also seven Janβen joints.

The equation for the spring stiffness of an open joint shows that the stiffness is related to the rotation, the bending moment and the normal force. However, the software application Scia Engineer only offers a non-linear rotational spring with a custom relation between rotation and bending moment. To simulate the changing normal force, several calculations, all with a different constant normal force, will be performed. Reality is a combination of these calculations.

3.4 Soil interaction

3.4.1 Soil loading according to Blom [2]

The lining must be stable and resist the water pressure. The structural forces and deformations however are complex to determine due to time dependent behaviour of the soil and the phased construction stage. An exact determination of the structural behaviour is only possible with an integral calculation approach, but is hardly to be fulfilled because of the complexity. In the design practice for tunnel linings a far more practical (and traditional) approach is used.

Even in the prefabrication stage a variety of loadings act on the segments, like de-moulding loading and lift and store loadings. During the construction stage also a variety of loadings act on the segments, like positioning loading, TBM jack loading and bold forces. Grout loading is important as well. The most dominant load during the serviceability stage is soil loading. Since the serviceability stage is the longest period in the segmental lifetime it should be aimed for that this stage is the most governing stage in structural design. For the purpose of this research, only a description of the soil loading is given.

In figure 3.4 the case of a tunnel surrounded by soil is considered. Assuming that the vertical soil pressure has to be calculated at a certain depth, the vertical pressure is calculated by the weight of the soil overburden above this level. At the same depth there is water pressure. The effective vertical soil pressure is calculated by subtracting the water pressure from the vertical soil pressure. The local horizontal effective soil pressure is calculated by multiplication of the effective vertical soil pressure with the horizontal soil coefficient. The total horizontal soil pressure is the sum of the effective horizontal soil pressure and the water pressure.

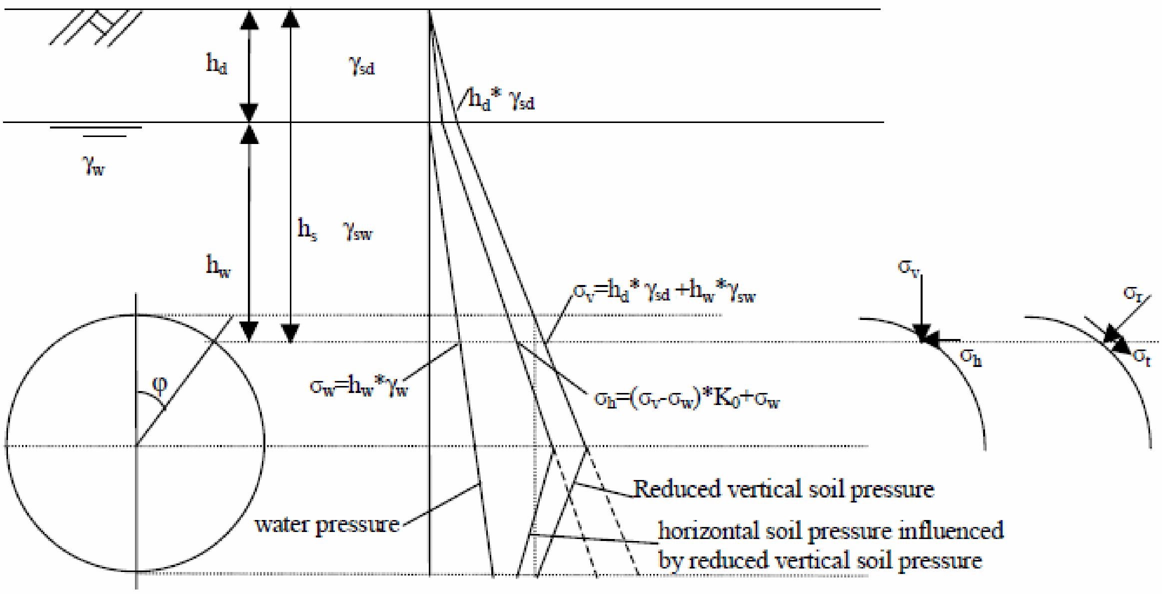

Figure 3.4 – Soil pressure on a ring of the lining.

The vertical and the horizontal soil pressure can be transformed into the radial and the tangential stress-loading components (figure 3.5). To activate the tangential loading component there must be a possibility to mobilise tangential friction between the soil and the lining. In several lining designs there has been an interesting discussion whether or not tangential loading occurs. The occurrence is expected to depend on all factors of soil properties, grout body properties and the interfaces between concrete and grout and grout and soil. Involving all tangential loading (in combination with the tangential soil reaction) could result in unrealistic lining dimensions. Even some existing linings would collapse due to this loading system. Some lining designs only involve a percentage of the full tangential loading (Botlek Railway Tunnel: 25%).

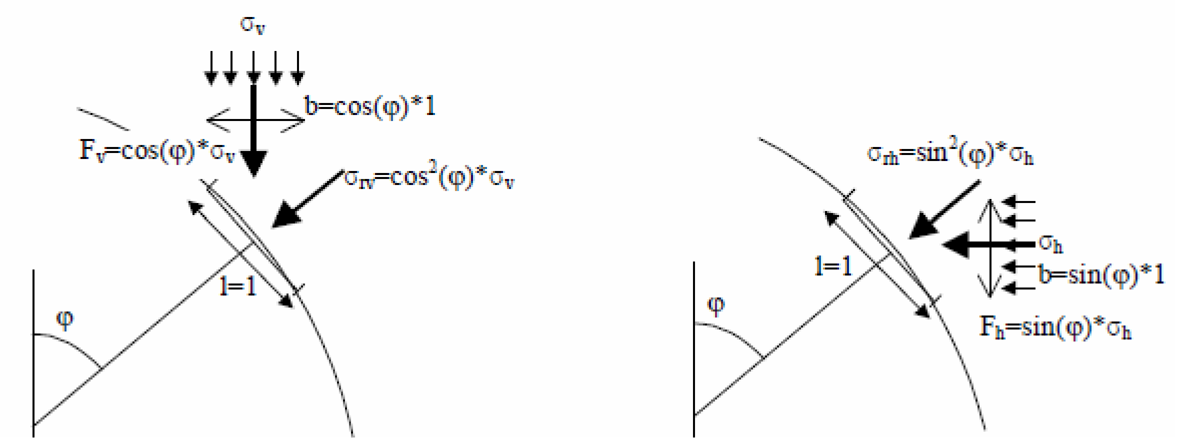

Figure 3.5 – Transformations of vertical and horizontal loading to the radial and tangential component.

The total radial component is:

$$\sigma_{r,\varphi} = \sigma_{v,\varphi} \cos^2(\varphi) + \sigma_{h,\varphi} \sin^2(\varphi)$$

The total tangential component is:

$$\sigma_{t,\varphi} = (\sigma_{v,\varphi} + \sigma_{h,\varphi}) \cos(\varphi) \sin(\varphi)$$

The structural model requires a definition of the loading in order to predict the internal forces and the deformations of the lining. Blom presents three approaches. The first approach makes use of a reduced vertical pressure on the lower half of the lining, the second approach assumes a constant vertical pressure but an increasing water pressure in relation to the depth and the third approach omits the floating due to water pressure. This third approach has been applied frequently, which gives a load system with pressure equilibrium in vertical and horizontal direction. One should think about the influence that the omission of floating has on the internal stress distribution and the deformations of the lining.

To illustrate the influence of floating on the internal forces and deformations of the lining, it is assumed that a ring is loaded only by water pressure and the ring is uniformly supported by an elastic soil continuum. Only radial loading will act due to the water pressure. Next it is assumed that the soil support is only active in radial direction. From this point of view the floating component of the water pressure will only result in a translation of the lining in the supporting medium. It is stated that the floating component due to water pressure does not result in bending moments and ovalisation of the ring, since all loads act in radial direction.

The question is: What values for active loading should be used in the calculations?

Due to floating the ring shifts upwards. The soil support on the upper part of the ring will increase (total pressure increases) while the soil support at the lower half of the ring will decrease (total pressure decreases). Finally, the vertical ring translation holds when the upward directed loading is equal to the downward directed loading. This means equilibrium of soil pressure on top, soil pressure at the bottom, self weight and floating. Since the self weight is very low compared to soil loading, the self weight is neglected. Hence, it is assumed that the self weight does not cause internal forces. The absolute vertical loading at the top and the bottom of the ring will then be equal to the vertical soil pressure at the centre of the ring: $\sigma_{top} = \sigma_{bottom} = \sigma_{vc}$. The horizontal loading at the sides of the ring is not influenced by the vertical translation of the ring: $\sigma_{side} = \sigma_{vc,eff} * K_0 + \sigma_{wc}$.

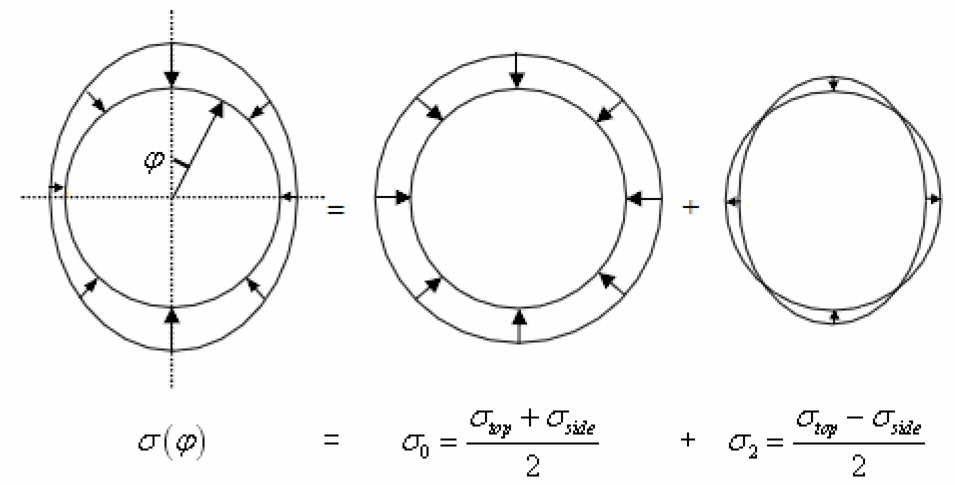

Figure 3.6 – The total loading on the lining is a summation of the uniform pressure σ_0 and the ovalisation pressure σ_2.

By determining the top and the side pressure, the uniform and ovalising radial pressure can be calculated. This is illustrated in figure 3.6. Realistic values are roughly: $0.15 \le \sigma_0 \le 0.7MPa$ and $0.03 \le \sigma_2 \le 0.15MPa$. However, σ_2 can be increased enormously by grout loading. The floating pressure component is called σ_1 and is omitted here. The total radial pressure around the ring is calculated with: $\sigma(\varphi) = \sigma_0 + \sigma_2 \cos(2\varphi)$.

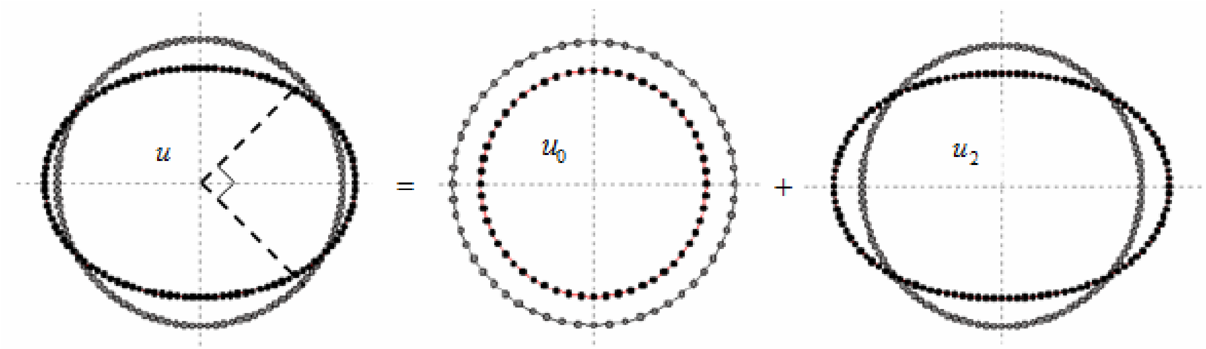

Figure 3.7 – deformations of the tunnel ring as result of the loads in figure 3.6.

The uniform loading (σ_0) causes normal forces only (hoop force; $N = \sigma_0 R$). Due to these normal forces the ring shrinks a bit, but stays circular (see u_0, figure 3.7). The ovalisation loading (σ_2) causes bending moments. Due to this loading the ring starts to bend and gets an oval shape (see u_2, figure 3.7). If the ovalisation loading increases, the horizontal diameter of the oval increases as well and simultaneously the curvatures at the top and bottom decrease. At a certain moment snap through takes place, because the ring is not able to resist the normal force anymore due to the large deformations (ovalisation) of the ring itself. Hence, at a certain moment the deformed geometry is not able to create equilibrium anymore. As one knows, the deformed situation is affected by the second order effect (GNL) and the physical non-linear behaviour (FNL). If both the uniform and the ovalisation loading increase, the negative effect of the ovalisation loading slightly reduces, since there is extra pressure at the sides of the ring to maintain a circular shape. This is undesirable for this specific study on snap through, since bending as a result of the ovalisation loading is an important aspect.

One of the failure mechanisms according to the current rules on tunnelling is the formation of a plastic hinge. Blom [4] shows that the opposite is true: the tunnel lining will not collapse after formation of a plastic hinge. Blom shows for the BRT that the load could even be three times higher ($\sigma_{2,ULS} = 3\sigma_{2,M_p}$) before the ring collapses explosively as a consequence of snap through (approximately when three plastic hinges are present). Thus, for the BRT holds a reserve capacity of a factor 3. However, one of the reasons that the reserve capacity indicates a very safe situation is that Blom [4] increased the ovalisation loading as well as the uniform loading.

In order to discover the reserve capacity for different rings, the load is dictated; σ_0 is constant and σ_2 increases in small steps until snap through has been occurred. Hence, to increase bending moments and trigger snap through, only the ovalisation loading is increased in this research. This was done to find out which mechanism is decisive. The reserve capacity can be expressed by a safety factor γ (paragraph 4.4). If $\gamma \geq 1$, the ring is safe and the formation a first plastic hinge is decisive. If $\gamma < 1$, a dangerous situation can appear, since the unexpected snap through collapse will be the decisive failure mechanism.

3.4.2 Soil support

Relative stiff parts in a structure attract more internal forces than relative weak parts. Since there is a certain stiffness ratio between the ring and the surrounding soil, the soil loading is supported by the ring as well as by the soil itself. It seems to be quite strange that the soil can load the tunnel and support it against this loading at the same time. This can be explained by the fact that the soil loading reacts on the deformation of the loaded structure. A very simple loading case is considered. Imagine a homogeneous ring with a certain axial stiffness, only loaded by a radial uniform loading from the soil. Due to the radial uniform loading it is obvious that the ring will have a uniform compressive deformation (the rings 'shrinks' a bit, but stays circular). Due to this compression the soil reaction is activated. The initial radial uniform loading will decrease due to the soil release. If compression is positive, the value of the equation underneath must be larger than zero, as soil can not bear tensile stress.

$\sigma_{total} = \sigma_{initial} - \sigma_{reduction} \geq 0$ Where: $\sigma_{initial} = \sigma(\varphi) = \sigma_0 + \sigma_2 \cos(2\varphi)$

The reduction loading ($\sigma_{reduction}$) is the result of the soil release and should be modelled with a continuum. Because this study focuses on the tunnel structure, a more practical model has been used. Blom [4] defined a solution to model the soil release by linear translational springs that support the periphery of the ring (bedding) against the initial loading ($\sigma_{initial}$).

$$\frac{k_r}{A_r} = \alpha_s \frac{E_{oed}}{r}$$

Where: k_r = integrated translational spring stiffness
E_{oed} = Oedometer stiffness (soil stiffness during one-dimensional compression test)
r = Radius of the tunnel
α_s = Soil stiffness reduction factor
A_r = Surface for which the bedding is represented by the spring k_r

When the soil is modelled with springs instead of a continuum, special attention should be paid to the spring stiffness. The main difference is that the springs do not interact with each other, while this is established in the continuum model. By comparing the continuum model with the spring model, it turned out that the equation $k_r / A_r = \alpha_s E_{oed} / r$ is useful in a frame analysis. A distinguish is made between uniform compression and ovalisation. In case of uniform compression the soil stiffness reduction factor has a value of $\alpha_s = 1$. In case of ovalisation the soil stiffness reduction factor has a value of $\alpha_s = 0.65$. In order to be consistent, $\alpha_s = 1$ is used in this research, since Blom [4] as well as Consortium DC-COB [1] adopted this value to analyse snap through.

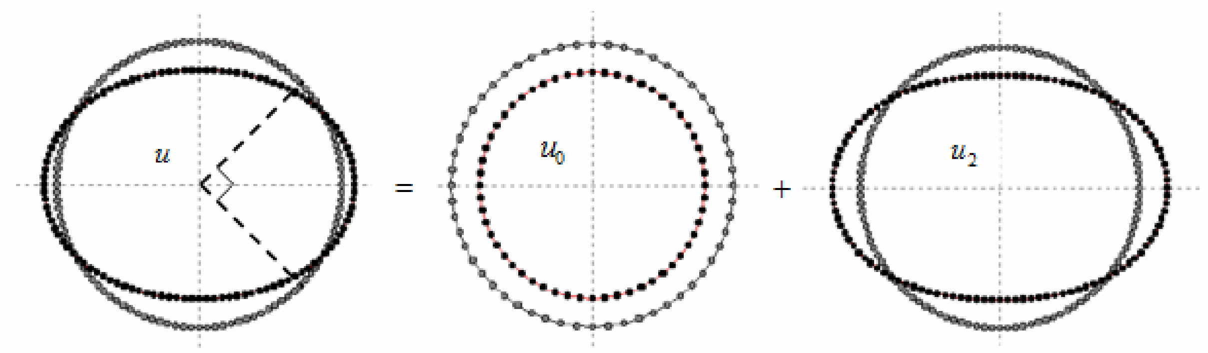

Figure 3.8 – deformations of the tunnel ring as result of the loading.

It is assumed that the soil on top of the tunnel follows the deformation of the tunnel. Hence, there is no soil release and the final loading (after deformation) equals the initial loading. To ensure equilibrium, the same holds for the soil under the tunnel. Therefore, the bedding is only projected at both sides of the tunnel. The bedding supports the sides over an angle of $90°$ (figure 3.9), because these areas are roughly the places for which the tunnel compresses the soil (figure 3.8). Moreover, projecting the bedding on top and at the bottom of the ring as well, will not contribute to more accurate knowledge about the reserve capacity.

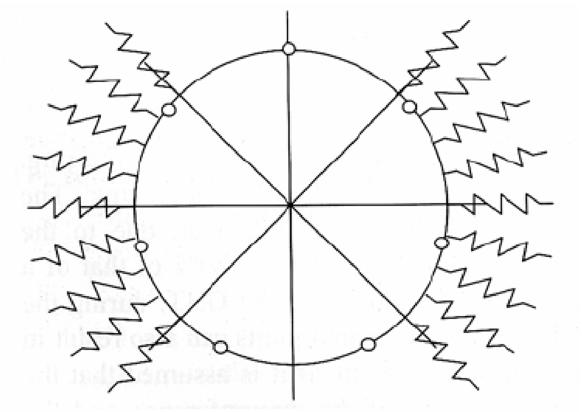

Figure 3.9 – The soil supports the ring (bedding).

3.5 Validation of the model for the reinforced concrete tunnel segments

The model for the concrete tunnel segments is a combination of beam elements and rotational spring elements. Figure 3.2 shows the cross-sectional behaviour of the segments, which is modelled by the rotational spring elements only. All beam elements are connected to just one rotational spring element. Therefore, all rotational spring elements are responsible for the physical non-linear behaviour of the segments over just the length of one beam element.

To ensure the validity of this discontinuous model, a comparison is made with a more accepted continuous model (table 3.1). This model only uses linear beam elements to model the physical behaviour of the segments. For both models the relation between the displacement at the top of the ring (u_{top}) and the loading (σ_2) is plotted (figure 3.10). Both models should indicate the same relation. Note: It is only possible to compare both models until the moment that the concrete starts to crack. The model with only beam elements does not take into account the reduced bending stiffness after the first crack. Hence, after the first crack both models could show different results. The first branch in figure 3.2 represents the uncracked cross-section. The corresponding maximum bending moment equals 153.47kNm. Both models should indicate the same results until this bending moment.

	Continuous model	Discontinuous model
Linear beam element	EA and EI	EA
Non-linear rotational spring element	-	EI

Table 3.1 – reproduction of the properties for each model.

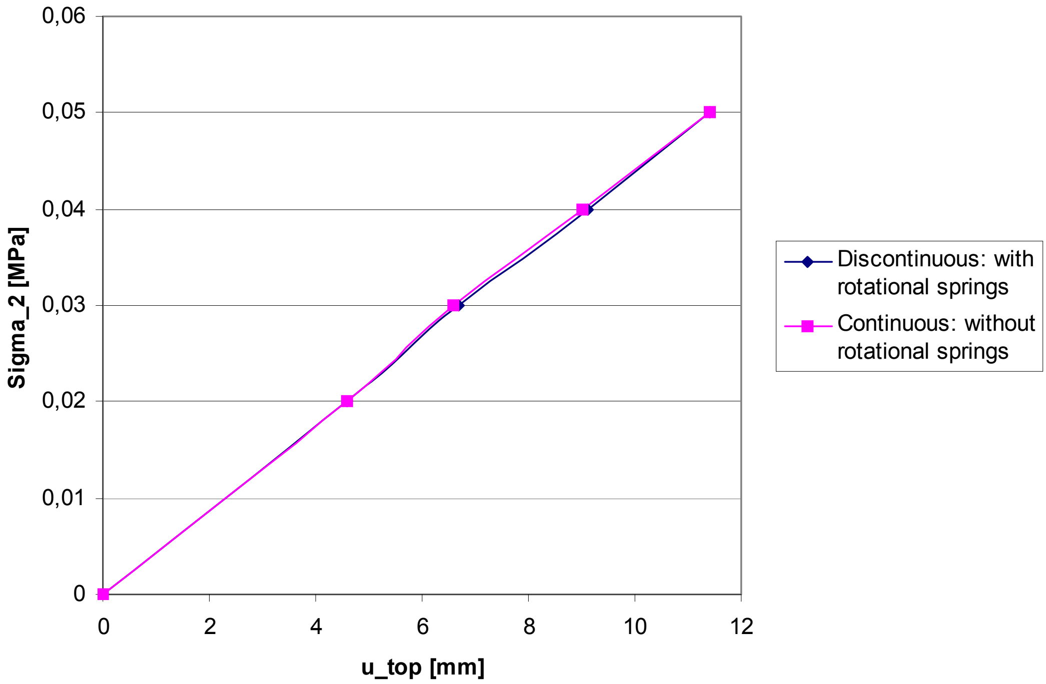

Figure 3.10 – The discontinuous model versus the more accepted continuous model.

Both models almost show exactly the same result. It is concluded that the discretised character of the model with beam elements and non-linear rotational spring elements is not less accurate than the more accepted continuous model with only beam elements.

Moreover, the results with respect to the non-linear structural behaviour of this discontinuous model can be compared with the results according to Blom and Consortium DC-COB [1]. The load versus displacement curves called 'Verticaal opgelegd A1' and 'Rectificatie thesis Blom' in figure 3.11 are representative.

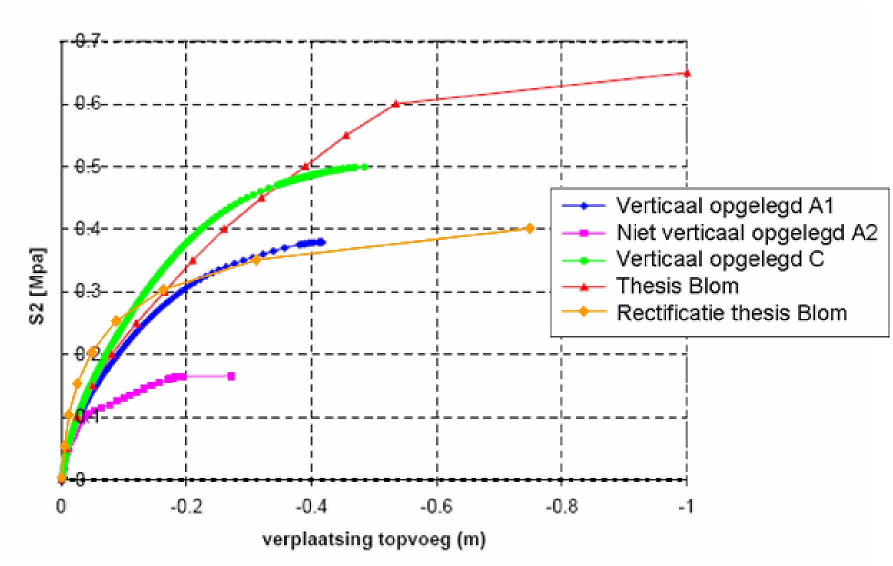

Figure 3.11 – Load (σ_2) vs. displacement (u_{top}) according to Blom and Consortium DC-COB.

The curve used in this research, presented in figure 3.12, fits very well too the two mentioned curves in figure 3.11. Therefore, it is concluded that the non-linear structural behaviour of this discontinuous model performs accurate enough as well. Figure 3.12 is based on a calculation with a constant normal force ($N = 3500kN$). This value is approximately the average of the minimum and maximum occurring normal force in the ring ($N_{\min} = 2262.5kN$ and $N_{\max} = 4200kN$).

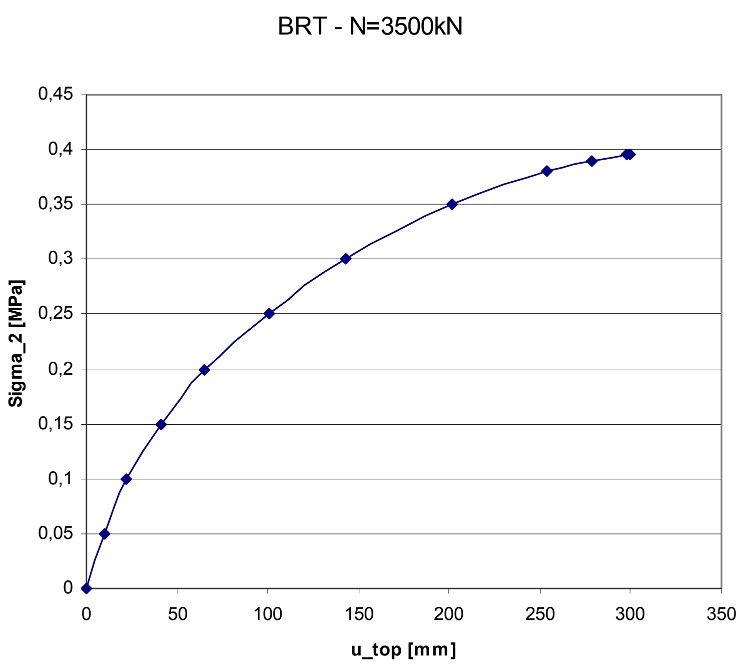

Figure 3.12 – Load (σ_2) vs. displacement (u_{top}) according to this research.

4 RESULTS AND INTERPRETATION

4.1 Introduction

From a mechanical point of view it is possible to analyse a structure in four different ways. In order to clarify the model from chapter 3, a visualisation displayed in figure 4.1. Figure 4.1 shows the behaviour of the ring for all four types of analysis.

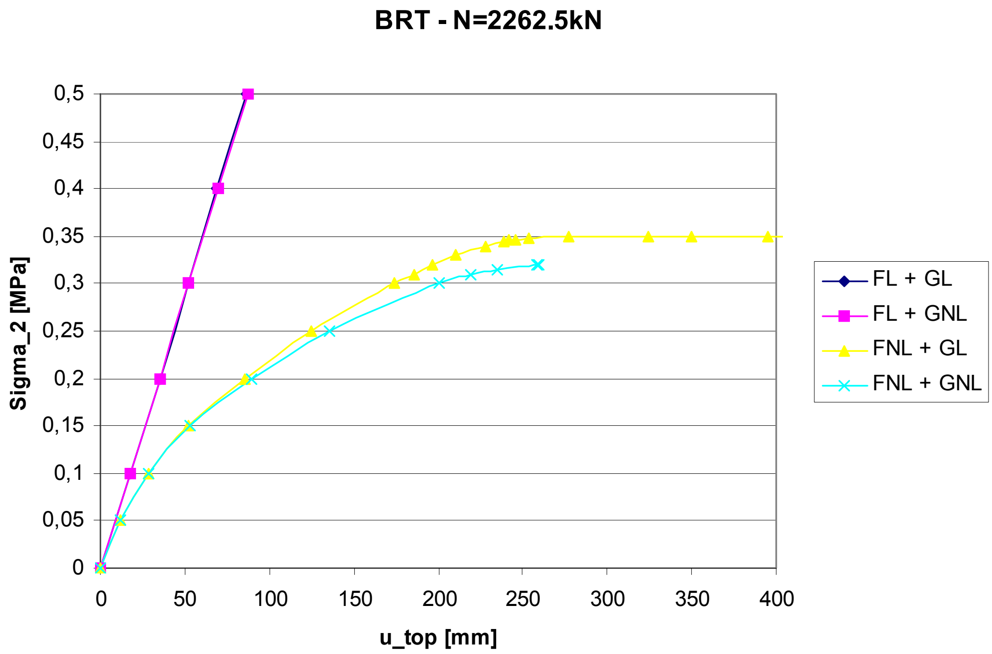

Figure 4.1 – The stiffness behaviour of four different types of mechanical analysis.

- FL + GL. The concrete segments as well as the Janβen joints are linear elastic (FL). The Janβen joints are realised with the initial linear stiffness according to paragraph 3.3. Equilibrium of forces is based on the undeformed situation, which means a first order calculation (GL). Obviously the relation between displacement (u_{top}) and force (σ_2) is linear. Note: this statement only holds for relative small displacements since the program assumes that $\tan(\theta) \approx \theta$ and $\sin(\theta) \approx \theta$. This is typical for a linear elastic (LE) calculation (appendix B).

- FL + GNL. The same physical behaviour from the first analysis is also used in this analysis. But now, equilibrium of forces is based on the deformed situation, which means a second order calculation (GNL). This line is normally used to determine the buckling load of the structure; the line approaches the buckling load asymptotically. However, in this case the structure is statically indeterminate and linear elastic. Exactly the same behaviour as in figure 6.6 (paragraph 6.2) is observed for this analysis. The Janβen joints are too stiff compared with the bedding stiffness to obtain instability (snap through). The buckling load is infinitely.

- FNL + GL. The physical behaviour of the concrete segments as well as the Janβen joints is non-linear (FNL). The segments are able to show reduced bending stiffness by cracking of the concrete and yielding of the reinforcement (paragraph 3.2). The Janβen joints are able to behave like the second branch of the $M-\theta$ relation as explained in paragraph 3.3. At a certain moment the structure reaches the plastic collapse load, which is clearly demonstrated in figure 4.1. The same geometrical behaviour from the first analysis is also used in this specific calculation.

- FNL + GNL. This fourth analysis is a 'summation' of all non-linear types of analysis mentioned above. The physical (segments and Janβen joints) as well as the geometrical behaviour is able to show non-linear relations. This analysis gives most accurate approach of reality. The model in chapter 3 is based on this type of analysis and corresponds to the weakest relation between displacement and force (figure 4.1).

Figure 4.1 is also a qualitative control of the analysis. The line corresponding to FL + GL must show the stiffest behaviour and the line corresponding to FNL + GNL must show the weakest behaviour. The lines corresponding to FL + GNL and FNL + GL must be somewhere is between. Figure 4.1 fulfils this requirement.

The well-known formula of Merchant provides extra confirmation about the accuracy of this analysis as well.

$$\frac{1}{F_c} = \frac{1}{F_b} + \frac{1}{F_p} \quad \rightarrow \quad \frac{1}{\sigma_{2,c}} = \frac{1}{\sigma_{2,b}} + \frac{1}{\sigma_{2,p}}$$

This formula gives in a simple way the critical geometrical and physical non-linear failure load (F_c) as a function of the buckling load (F_b) and the plastic collapse load (F_p).

$$\frac{1}{\sigma_{2,c}} = \frac{1}{\infty} + \frac{1}{0.3497} \quad \rightarrow \quad \sigma_{2,c} = 0.3497 MPa \approx 0.3202 MPa$$

This formula is only valid for simple structures. In most cases the critical collapse load is overestimated [9]. This statement confirms the result exactly.

4.2 Results

In order to obtain good results, three different diameters were considered. The three ring calculations were carried out for many constant normal forces. This is done to simulate the varying normal force in the segments and the Janβen joints. All calculations together provided a clear view of the ring behaviour influenced by the diameter and the normal force.

This chapter is about the results of the calculations when using the model according to chapter 3. An interpretation of these results is presented as well. Afterwards a conclusion is formulated, based on the results and interpretation.

First of all, the important internal forces were discussed. Figure 4.2 (left) shows the real normal force of the BRT is case of a low modelled normal force and small ovalisation loading. Figure 4.2 (right) shows the real normal force of the BRT is case of a low modelled normal force and large ovalisation loading, just before snap through occurs.

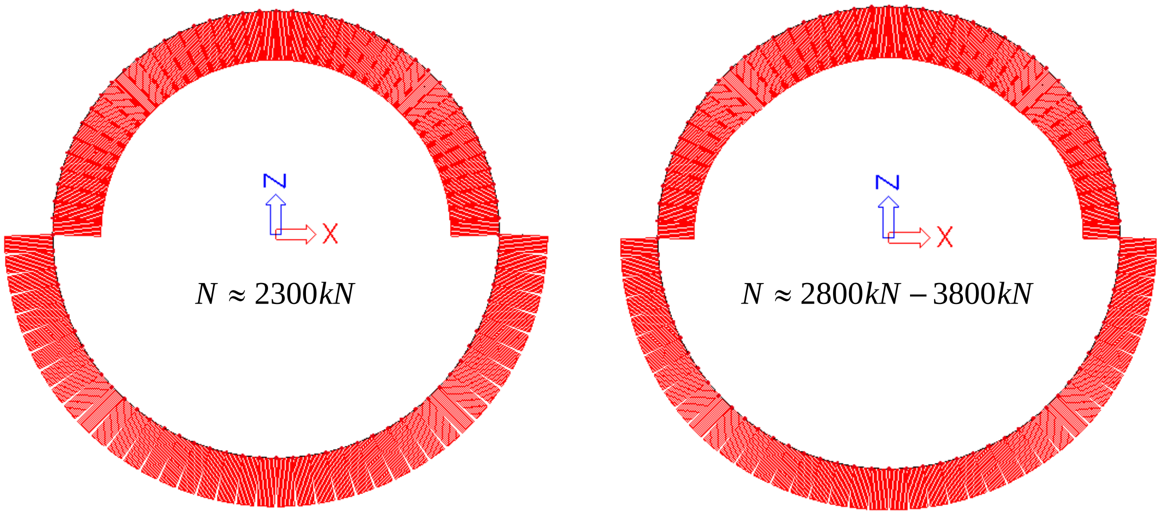

Figure 4.2 – The real compressive normal force in the ring for the BRT. Left: modelled N=2262.5kN, ovalisation loading $\sigma_2 = 0.05MPa$. Right: modelled N=2262.5kN, ovalisation loading $\sigma_2 = 0.3202MPa$.

The visual normal forces of both rings in figure 4.2 can not be compared; the diagrams are not on scale with reference to each other. The abrupt change in the diagrams is a result of the x coordinate that changes sign. Figure 4.2 (left) shows a uniform distribution of the normal force along the ring periphery. Figure 4.2 (right) shows a less uniform distribution of the normal force along the ring periphery. The normal force in the top region has the highest value and the normal force at the sides is the lowest. The bottom normal force is somewhere in between.

Figure 4.3 (left) shows the real bending moment of the BRT in case of a low modelled normal force and small ovalisation loading. Figure 4.3 (right) shows the bending moment of the BRT in case of a low modelled normal force and large ovalisation loading, just before snap through occurs.

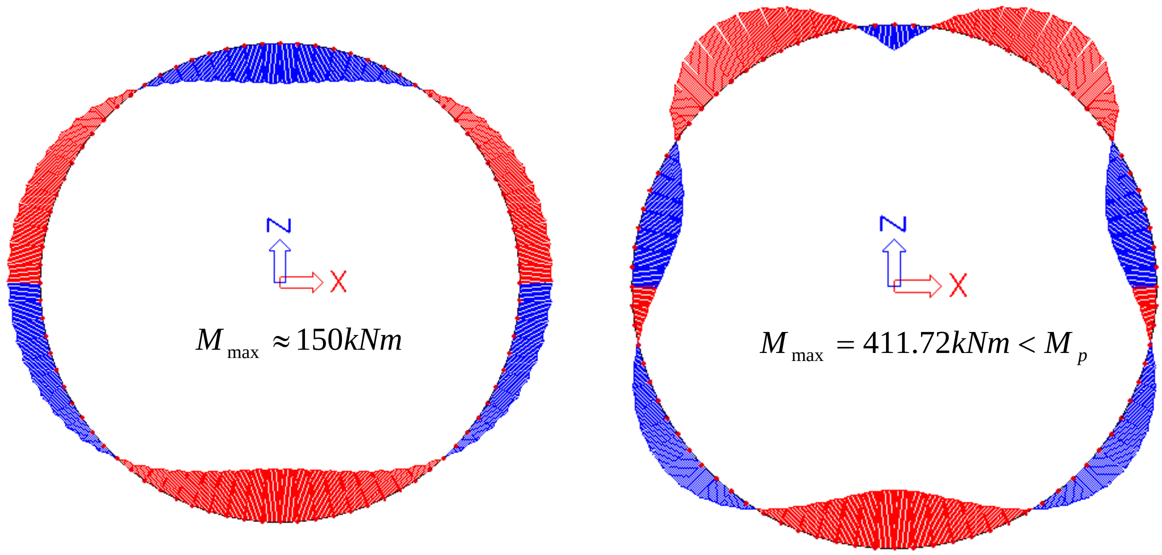

Figure 4.3 – The bending moment (change) in the ring for the BRT. Left: modelled N=2262.5kN, ovalisation loading σ_2 = 0.05MPa . Right: modelled N=2262.5kN, ovalisation loading σ_2 = 0.3202MPa .

The visual bending moments of both rings in figure 4.3 can not be compared; the diagrams are not on scale with reference to each other. Nearby, the shape of both diagrams in figure 4.3 is quite different.

Secondly, the relation between the ovalisation loading and displacement for the BRT is given in figure 4.4. Since snap through is expected in the top region, the displacement of the node at the top of the ring is considered.

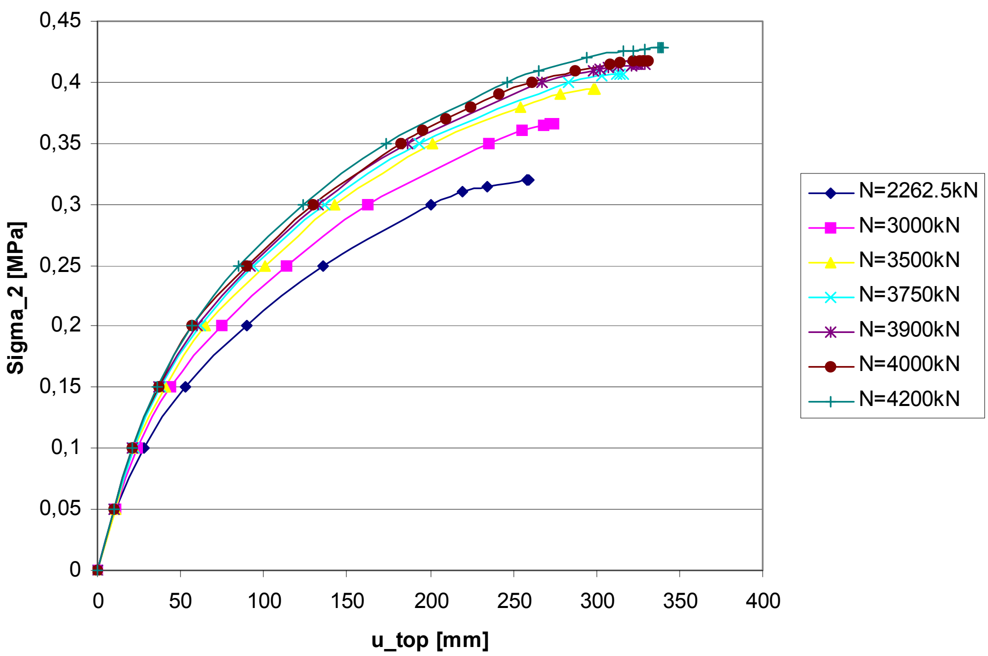

Figure 4.4 – u_{top} vs. σ_2 for the BRT, modelled with different values for the normal force.

Figure 4.4 shows that a larger normal force causes stiffer ring behaviour. The extreme values for u_{top} and σ_2 increase as well in case of a larger normal force.

4.3 Interpretation

Normal force

The left picture in figure 4.2 shows a uniform distribution of the normal force. This is the result of the relative high uniform pressure σ_0. This uniform pressure only results in a uniform normal force (hoop force), which is described by the "ketel" formula. The tangential normal force N_0 is determined by consideration of the forces as shown in figure 4.5. Horizontally, these forces are definitely in equilibrium. The relation between N_0 and σ_0 comes from vertical force equilibrium.

$$\sum N_0 = \int_{-\pi/2}^{\pi/2} \sigma_0 \cos(\varphi) r d\varphi \Rightarrow 2N_0 = \sigma_0 r [\sin(\varphi)]_{-\pi/2}^{\pi/2} = \sigma_0 r [1 - -1] \Rightarrow N_0 = \sigma_0 r [N/m']$$

The tangential normal force is given in force per unit length of the ring; $N = \sigma_0 r$, where r is the radius of the ring. $N = 0.5 \cdot 10^6 * 4.525 = 2262.5kN$. This is quite close to the actual value of $N = 2300kN$. Since the ovalisation pressure σ_2 is very low, almost no bending occurs. As a consequence, there are almost no reaction forces from the bedding. Therefore, the modelled normal force almost equals the actual normal force.

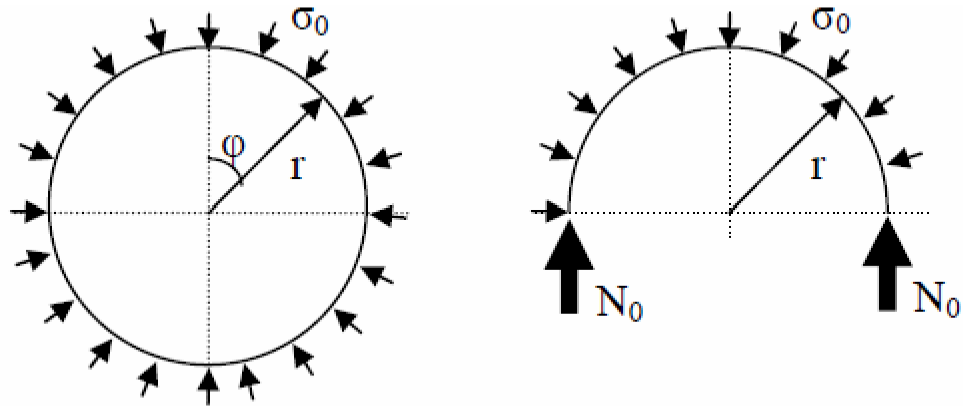

Figure 4.5 – Uniform compression

The right picture in figure 4.2 shows a less uniform distribution of the normal force. This is the result of the increased ovalisation pressure, which is now of the same magnitude as the uniform pressure. The primary effect of the ovalisation pressure is the occurrence of bending moment along the ring. As a consequence of the bending moment, the ring starts to deform and gets an oval shape ("lying egg"). The sides of the ring were pushed outwards into the soil, which activates the bedding. So, the secondary effect is that the bedding starts to resist this deformation, because the active or neutral soil pressure shifts towards more passive soil pressure (the soil stiffens). The normal force in the top and bottom region increases most. This is explained by figure 4.6.

Due to the configuration of the Janβen joints in this ring; the top region has less bending stiffness than the bottom region. Therefore, the top region deforms easier and pushes more into the soil (more bedding reaction forces). Hence, the top region experiences even more normal force than the bottom region. This is perfectly expressed by the right picture in figure 4.2.

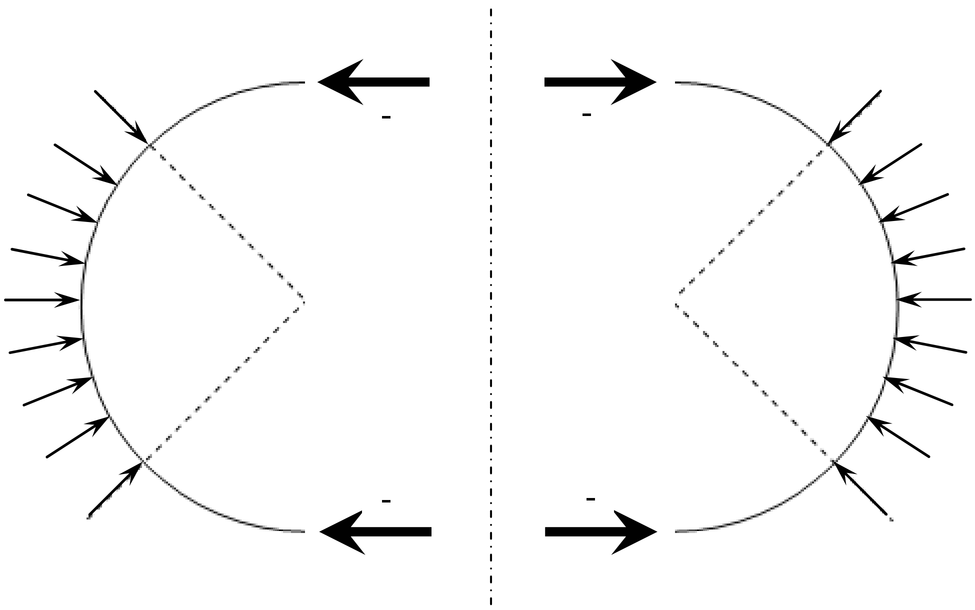

Figure 4.6 – The increasing normal force (large arrows) in top and bottom region due to the bedding reaction forces (small arrows).

It is concluded that the normal force in the ring depends on the uniform pressure as well as the bedding (stiffness). The stiffness of the bedding defines the relation between the deformation of the ring and the increasing normal force. Note: the normal force is completely determined by the soil properties (σ_0 and the bedding stiffness). This is not surprisingly at all, since internal forces are always caused by the (external) loading.

Bending moment
The left picture in figure 4.3 shows a bending moment that belongs to a homogeneous ring, subjected to ovalisation. This statement is quite obvious since the ovalisation loading is very small, relative to the uniform loading. The relative high uniform loading provides the ring high bending stiffness because the normal force is very high. Since the ovalisation pressure is relatively low, there is also little impulse to bend the ring. There are barely any stiffness differences along the ring. So, a high loading ratio (σ_0/σ_2) has a positive influence on physical behaviour of the ring. Especially the Janβen joints are able to show stiff behaviour in case of high loading ratio. As a consequence the ring will not deform very much. This fact has also a positive influence on geometrical behaviour. Since the ring remains quite circular, it is able to carry the load even better. It turned out that a higher ratio between the uniform loading and the ovalisation loading (σ_0/σ_2) results in more homogeneous ring behaviour. A stiffer bedding also contributes to more homogeneous ring behaviour since it resists ovalisation. This effect will be stronger when the bedding is stiffer.

The right picture in figure 4.3 shows a bending moment that differs a lot from the left picture. The bending moment changes sign more frequently. The reason is a low loading ratio, which means relative low bending stiffness to resist ovalisation. Especially the Janβen joints are too weak to maintain the circular shape of the tunnel in case of relative high ovalisation loading. As one knows, stiff parts (segments) attract more internal forces than weak parts (Janβen joints). Since there are stiffness differences along the ring, the bending moment distribution has been changed.

It is concluded that the bending moment distribution depends on the corporation between the segments, the Janβen joints and the bedding. Actually, the bending moment distribution depends on the stiffness differences between the segments, the Janβen joints and the bedding. This is always the case when a statically indeterminate structure is considered. The magnitude of the bending moment is caused by the (external) loading.

Load versus displacement
Figure 4.4 shows that a larger normal force causes stiffer ring behaviour. This behaviour can be explained very easily by the fact that a larger normal force will increase the bending stiffness of the segments and the Janβen joints. Hence, the entire ring attracts more internal forces while the deformations are relatively low.

The maximum values for u_{top} and σ_2 increase as well in case of a larger normal force. This can be clarified by comparing the ring behaviour for a low and a high normal force.

The ring corresponding to the line for N=2262.5kN snaps through just after formation of the first plastic spot in the two upper segments ($\varepsilon_c = 1.75 \cdot 10^{-3}$, figure 4.7). This is the result of an intense decrease of the bending stiffness. At this point the ring is not able to attain equilibrium of forces anymore. The collapse is induced by the changing physical properties.

The ring corresponding to the line for N=4200kN snaps through when already five plastic spots have been developed in both upper segments ($1.75 \cdot 10^{-3} < \varepsilon_c < 3.5 \cdot 10^{-3}$). The highest value for the bending moment is indicated in figure 4.7. This is the result of much less reduction of the bending stiffness in case of high normal force. The ring is still able to maintain equilibrium of forces after the formation of the first plastic spot in the two upper segments (figure 4.7). Thereby, also the bending moment capacity of the segments increases in case of high normal force. Finally, the ring collapses as result of the deformed geometry.

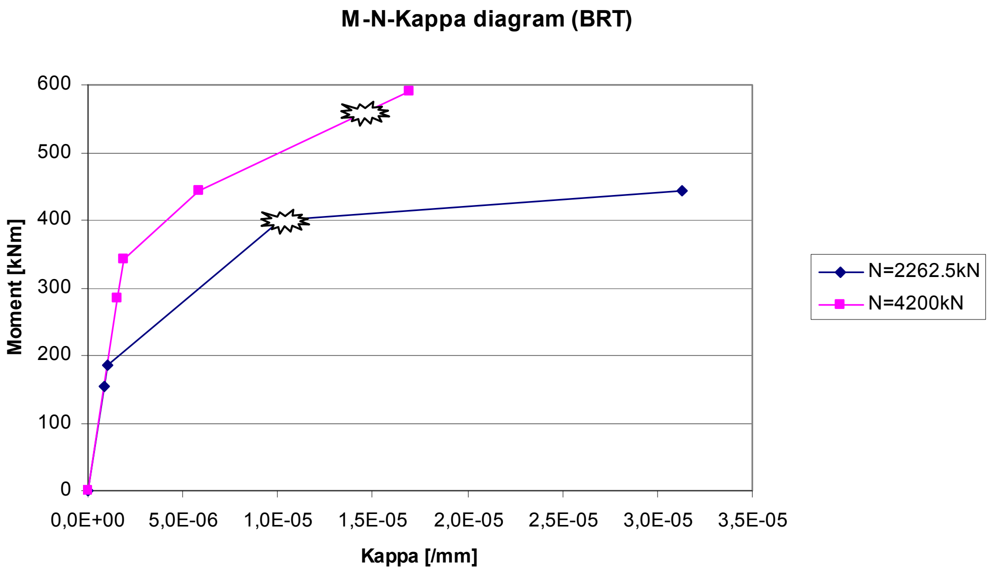

Figure 4.7 – Cross-sectional behaviour of the segments in case of low and high normal force.

Figure 4.7 clearly shows the occurrence of more deformation (which means larger u_{top}) and relative more bending moment (which means larger σ_2) just before snap through in case of a higher normal force.

4.4 Reserve capacity

One of the failure mechanisms according to the current rules on tunnelling is the formation of a plastic hinge. Blom [4] shows that the opposite is true; the tunnel lining will not collapse after formation of the first plastic hinge. The load can increase till snap through occurs. To quantify the reserve capacity, a safety factor γ is defined. For $\gamma \geq 1$ the ring is safe and the formation of the first plastic hinge is decisive. If $\gamma < 1$, a dangerous situation can appear, since the unexpected snap through collapse will be the decisive failure mechanism. Hence, if $\gamma < 1$, snap through occurs without any plastic hinge in the lining. In this situation the safety factor is defined by the ratio between the maximum occurred bending moment in the lining just before snap through and the value for the theoretical plastic moment.

$$\gamma = \gamma_1 = \frac{M_{\max}}{M_p} < 1$$

If $\gamma \geq 1$, the formation of the first plastic hinge occurs at an earlier load stage than snap through. In this situation, the safety factor is defined by the ratio between ultimate value σ_2 (for which snap through occurs) and the value for σ_2 where the first plastic hinge develops.

$$\gamma = \gamma_2 = \frac{\sigma_{2,snap\ through}}{\sigma_{2,first\ plastic\ hinge}} = \frac{\sigma_{2,st}}{\sigma_{2,M_p}} \geq 1$$

As mentioned before, three different diameters are considered for many constant normal forces; $r = 0.5r_{BRT}$, $r = r_{BRT}$ and $r = 2r_{BRT}$. Table 4.1 shows an abstract of all parameters. Note: parameters that depend on the radius change proportionally. Dependent on the diameter and the modelled normal force, a plastic hinge could develop before snap through occurs. In all situations, only one safety factor is determined (γ_1 or γ_2), as only one value for γ is valid in a specific situation; $\gamma < 1$ or $\gamma \geq 1$. Figure 4.8 shows the safety factor for all tunnels and all modelled normal forces.

r=2.2625m (0.5BRT)	**r=4.525m (BRT)**	**r=9.05m (2BRT)**
$d_{seg} = 200mm$	$d_{seg} = 400mm$	$d_{seg} = 800mm$
$l_t = 85mm$	$l_t = 170mm$	$l_t = 340mm$
$B45$	$B45$	$B45$
$E_{oed} = 38MPa$	$E_{oed} = 38MPa$	$E_{oed} = 38MPa$
$k_b = 16.7956MN/m^2$	$k_b = 8.3978MN/m^2$	$k_b = 4.1989MN/m^2$
$\alpha_{bedding} = 90°$	$\alpha_{bedding} = 90°$	$\alpha_{bedding} = 90°$
$n_{seg} = 7$	$n_{seg} = 7$	$n_{seg} = 7$
$\sigma_0 = 0.5MPa$	$\sigma_0 = 0.5MPa$	$\sigma_0 = 0.5MPa$
$\omega_{0,\min} = 0.18\%$	$\omega_{0,\min} = 0.18\%$	$\omega_{0,\min} = 0.18\%$
$c = 35mm$	$c = 35mm$	$c = 35mm$
$\phi_{rebar} = 10mm$	$\phi_{rebar} = 10mm$	$\phi_{rebar} = 10mm$

Table 4.1 – Abstract of the parameters for all three tunnels.

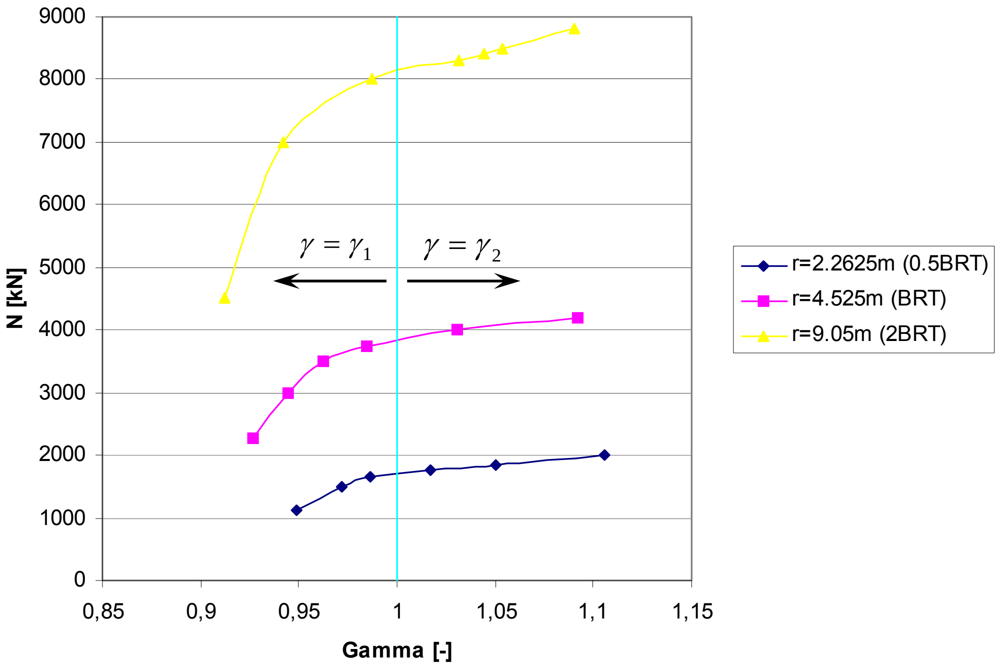

Figure 4.8 – Modelled normal force N vs. γ for all three tunnel diameters.

The value γ_1 starts to present a nonlinear relation with the normal force for values nearly equal to 1. For smaller values of γ_1, the relation looks linear. γ_2 shows a linear relation with the normal force at all time.

Figure 4.4 displays many relations between u_{top} and σ_2 for the BRT. The behaviour for N=2262.5kN is too weak, because the modelled normal force is too low. The behaviour for N=4200kN is too stiff, because the modelled normal force is too high. The real behaviour is somewhere in between. Quantifying this finding is very difficult. The same philosophy holds for figure 4.8. The lowest value for γ_1 is based on the minimum occurring normal force, $N = \sigma_0 r$ ($\gamma_{1,\min}$). The highest value for γ_2 is based on the maximum occurring normal force ($\gamma_{2,\max}$). The values $\gamma_{1,\min}$ respectively $\gamma_{2,\max}$ are too low respectively too high. The real situation is somewhere in between these extreme values (grey area). For all three tunnels, these two extreme values are showed in figure 4.9.

Figure 4.9 indicates that small radius and large normal force have positive influence on safety. A higher normal force increases the bending stiffness of the ring (segments and Janβen joints). However, the bending moment capacity of the segmental cross-section does not increase proportionally as a consequence of higher normal force. Figure 4.7 clearly explains the occurrence of more deformation and relative more bending moment just before snap through in case of higher normal force. This results in more reserve capacity.

Figure 4.10 shows the relation between the ovalisation loading and the displacement at the top for all tunnels. This figure gives information about the stiffness of the tunnels. It turned out that a twice as large diameter behaves more than twice as weak. So, relative less bending moment is attracted by the segments, which results in less safety.

The situation concerning snap through is worse than Blom [4] predicted. Figure 4.9 shows that γ is quite close to one for all diameters, instead of $\gamma = 3$ as Blom predicted for the BRT. Therefore, a closer look at practical design methods is needed (paragraph 4.5).

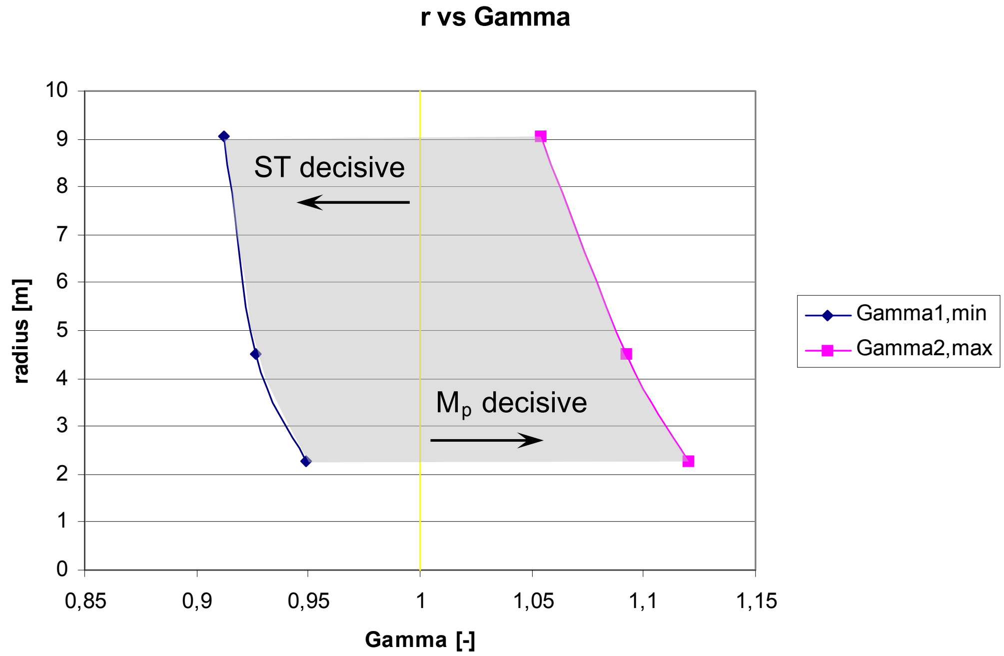

Figure 4.9 – Radius vs. γ . ST = snap through.

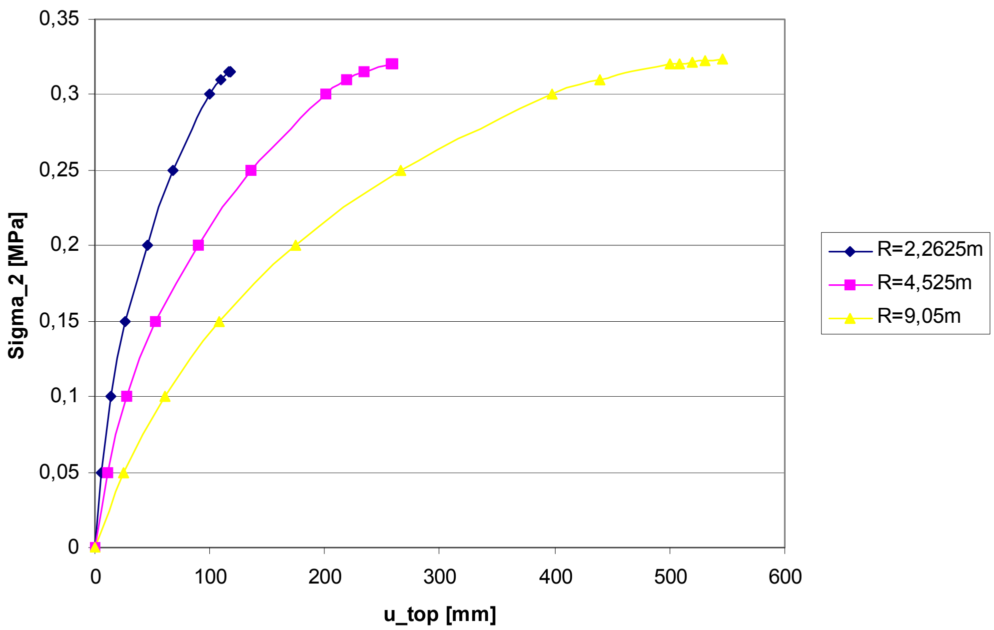

Figure 4.10 – u_{top} vs. σ_2 concerning the radius. These Lines are valid for the lowest acting normal force in the ring.

A second plastic hinge is not found in any calculation. Only the bottom of the ring was stiff enough to reach the bending moment capacity under certain conditions. In the top region, only plastic behaviour has been observed ($1.75 \cdot 10^{-3} < \varepsilon_c < 3.5 \cdot 10^{-3}$). Depending on the normal force, on one or more spots in the two upper segments show this plastic behaviour.

4.5 Reserve capacity concerning engineering practice

As mentioned before, this research is based on a FNL + GNL analysis; which is the best approach of real behaviour. However, in practice, most of the time a FL + GL analysis is carried out. Sometimes the analysis is extended by the non-linear behaviour of the Janβen joints, which is called SL + JNL + GL (segments linear + Janβen non-linear + geometrical linear). This means a first order calculation including linear elastic segments and non-linear Janβen joints. All three types of analysis are presented in figure 4.11.

Both alternative models are too stiff. As a consequence, the bending moment in the ring is too high for the corresponding deformation. Therefore, the bending moment capacity is reached at an earlier load stage. Hence, the inaccuracy of the two practical analyses provides saver or less unsafe results.

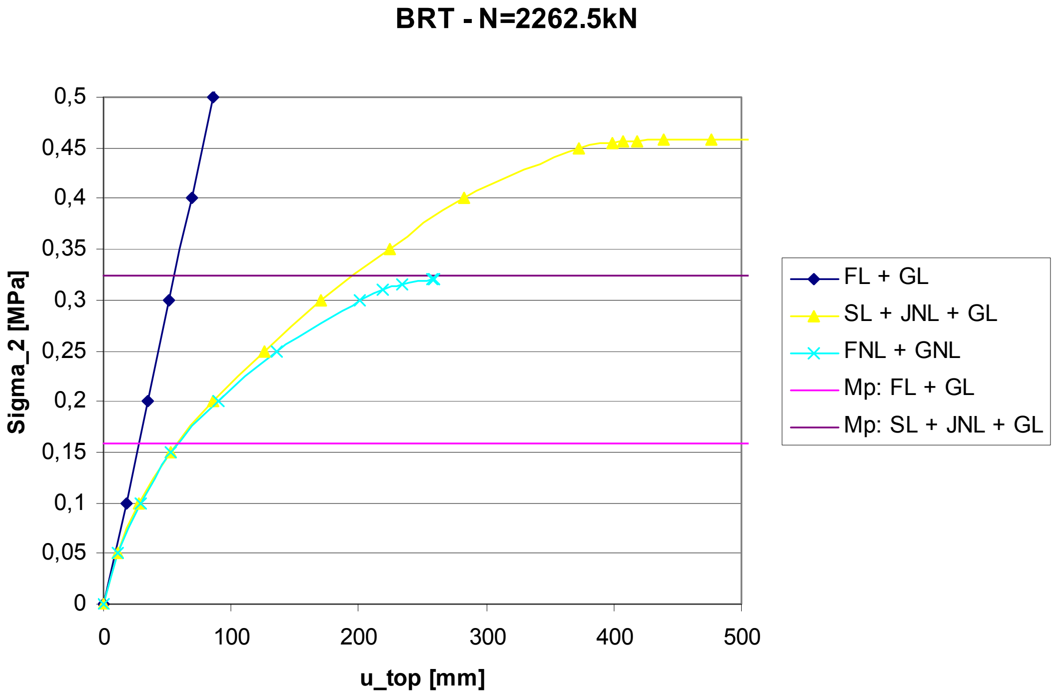

Figure 4.11 – Two types of practical mechanical analysis versus the scientific mechanical analysis.

The two horizontal lines represent the values σ_2 for which the bending moment capacity has been reached for both alternative analyses (σ_{2,M_p}). In case of a FL + GL analysis, the bending moment capacity is reached at a very early load stage ($\sigma_2 = 0.1586MPa$, only valid for the situation in figure 4.11). In case of a SL + JNL + GL analysis, the bending stiffness of the ring is reduced due to the non-linear Janβen joints. In this case, the ovalisation loading must be significantly higher to reach the bending moment capacity ($\sigma_2 = 0.324MPa$, only valid for the situation in figure 4.11). These values will be compared with $\sigma_{2,st}$. This is the load for which snap through occurs in the scientific analysis (FNL + GNL). The safety factor can be determined.

$$\lambda = \frac{\sigma_{2,st}}{\sigma_{2,M_p}}$$

This safety factor is demonstrated in figure 4.12 for all tunnel diameters. Again, two extreme values, corresponding to the minimum and maximum occurring normal force in the ring, are presented for both types of practical analysis. The real λ value is somewhere in between (grey area).

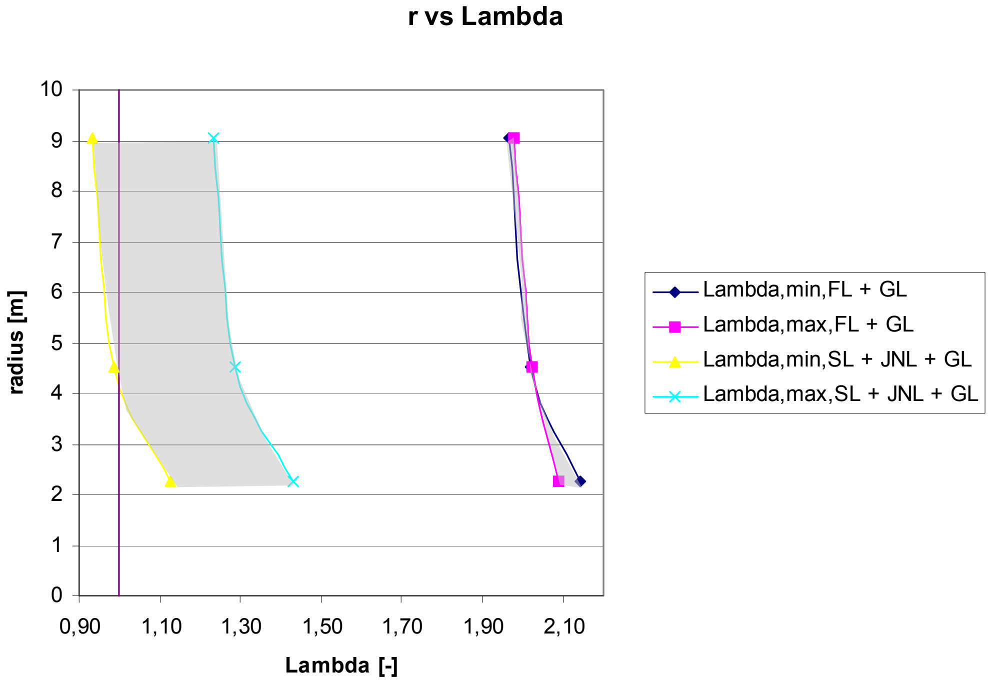

Figure 4.12 – Radius vs. λ

Figure 4.12 indicates that the practical methods are almost safe at all time. The lines corresponding to the FL + GL analysis provides safest results. It turned out that the normal force is not important in this case. Figure 4.4 displays that a higher normal force increases the snap through failure load ($\sigma_{2,st}$). But, also the bending moment capacity increases in case of higher normal force (figure 4.7). Since this calculation is linear elastic, there is a linear relation between σ_{2,M_p} and the bending moment capacity. Hence, $\sigma_{2,st}$ as well as σ_{2,M_p} increase in case of a higher normal force. Apparently these values increase proportionally. Therefore, the safety factor λ is barely influenced by the normal force. For all normal forces and all diameters $\lambda \approx 2$. Note: the initial stiffness of the Janβen joints has the same value in both extreme cases.

The lines corresponding to the SL + JNL + GL analysis provides least safe results. It turned out that the normal force is important in this case. Paragraph 3.3 as well as appendix D explained that a higher normal force increases the bending stiffness of the Janβen joints. In contradiction with the FL + GL analysis, the bending stiffness of the ring has increased in case of higher normal force. Therefore, the bending moment capacity is not increasing proportionally anymore. Thus, a larger safety factor is observed when both extreme situations of the SL + JNL + GL analysis are compared.

With respect to the BRT, one can conclude that the safety factor is about two ($\lambda \approx 2$), if a linear elastic analysis (FL + GL) has been used for designing this tunnel. However, if a SL + JNL + GL analysis has been applied, the safety factor is in the range of $0.99 \leq \lambda \leq 1.29$. Hence, although the BRT design is probably based on the right failure criterion, the reserve capacity is quite low in this case. Moreover, realistic soil loading will not cause snap through.

4.6 Conclusion

The situation concerning snap through is worse than Blom [4] predicted. It turned out that the γ value is close to one, instead of $\gamma = 3$ as Blom predicted for the BRT. However, the γ value varies to some extent for different diameters. Since γ is close to the critical point for snap through, a closer look at practical design methods was carried out to discover whether or not practical assumptions are still valid.

Despite the wrong results, it is concluded that everyone can safely go to bed when using the FL + GL (linear elastic) analysis, because snap through will never occur before the bending moment capacity has been reached ($\lambda \approx 2$). More awareness of reality is required for everyone who uses the SL + JNL + GL (linear elastic with non-linear Janβen joints) analysis. For larger tunnel diameters ($r > 4m$) it is more likely that the analysis provides unsafe results (figure 4.12). A larger possibility exists that snap through takes place without any plastic hinge.

This conclusion is only valid concerning the diameter of the tunnel. In this specific research it was not possible to determine the 'exact' reserve capacity for different tunnel diameters since the influence of the normal force can not be included. However, based on specific parameter sets it was possible to indicate minimum and maximum values for the reserve capacity.

This research confirms the expectation that increasing the tunnel diameter has negative influence on safety of the design when using a practical way to analyse a shield driven tunnel. Since it is not unthinkable that snap through is the decisive failure mechanism, it is very dangerous if one realises that the practical methods to analyse a shield driven tunnel will not notice this failure mechanism. The tunnel design is probably based on the wrong criterion.

5 OUT OF THE BOX

5.1 Introduction

The objective of this research was to discover the influence of the tunnel diameter on snap through failure concerning the reserve capacity. An answer is given in chapter 4. The conclusion in paragraph 4.6 is only valid for the parameter values given in table 4.1. The corresponding literature study [7] and the research itself provided the expectation that some other parameters have influence on safety as well.

This chapter will describe the influence of the segmental thickness (d_{seg}) only. This is the most interesting parameter since the segmental thickness is determined by an empirical rule. One twentieth times the tunnel's internal diameter is a rule of thumb to calculate the segmental thickness, simply because it works very well.

$$d_{seg} = \frac{1}{20} D_i$$

The analysis is done by presenting an elaboration that looks like paragraph 4.4 and 4.5.

5.2 segmental thickness

This parameter has a lot of influence on the stiffness of the lining and the bending moment capacity. Paragraph 4.3 already explained the importance of the stiffness differences between the segments, the Janβen joints and the bedding. To study the relation between the segmental thickness and safety, the BRT is analysed with three different linings (table 5.1). Note: the height of the Janβen joint (l_t) depends on the segmental thickness and changes proportionally.

$r = 4.525m$	$r = 4.525m$	$r = 4.525m$
d_{seg} = 200mm	**d_{seg} = 400mm (BRT)**	**d_{seg} = 800mm**
$l_t = 85mm$	$l_t = 170mm$	$l_t = 340mm$
$B45$	$B45$	$B45$
$E_{oed} = 38MPa$	$E_{oed} = 38MPa$	$E_{oed} = 38MPa$
$k_b = 8.3978MN/m^2$	$k_b = 8.3978MN/m^2$	$k_b = 8.3978MN/m^2$
$\alpha_{bedding} = 90°$	$\alpha_{bedding} = 90°$	$\alpha_{bedding} = 90°$
$n_{seg} = 7$	$n_{seg} = 7$	$n_{seg} = 7$
$\sigma_0 = 0.5MPa$	$\sigma_0 = 0.5MPa$	$\sigma_0 = 0.5MPa$
$\omega_{0,\min} = 0.18\%$	$\omega_{0,\min} = 0.18\%$	$\omega_{0,\min} = 0.18\%$
$c = 35mm$	$c = 35mm$	$c = 35mm$
$\phi_{rebar} = 10mm$	$\phi_{rebar} = 10mm$	$\phi_{rebar} = 10mm$

Table 5.1 – Abstract of the parameters for all three tunnels.

The safety factor γ is determined in the same way as mentioned in paragraph 4.4. These results are based on the extreme values for the normal force as well. Reality is somewhere in between (grey area). The safety factor γ, which is based on a FNL + GNL analysis, is displayed in figure 5.1.

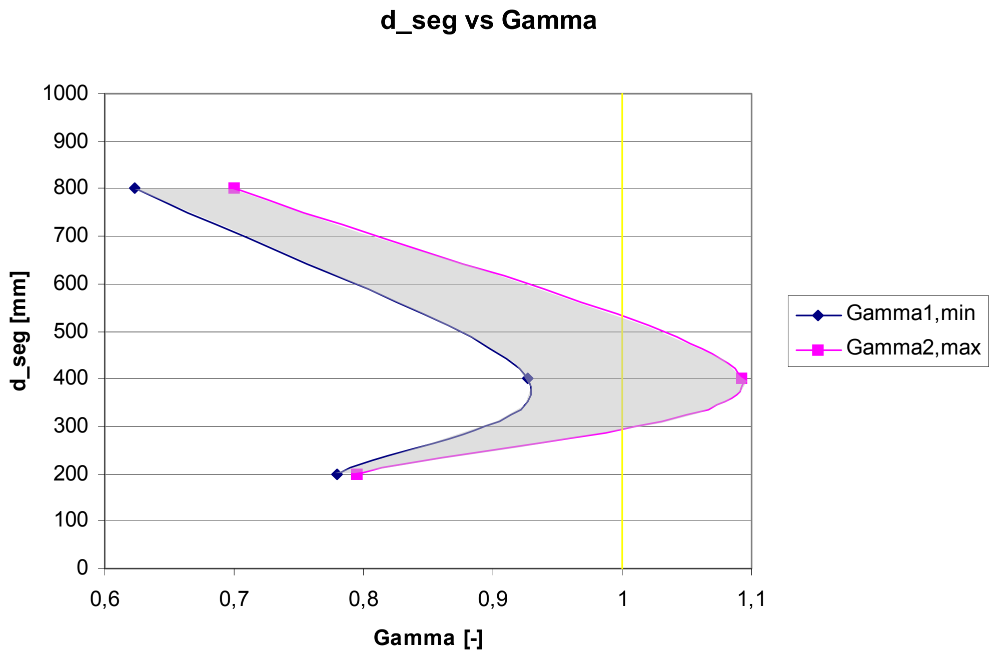

Figure 5.1 – segmental thickness vs. γ

Figure 5.1 indicates that the segmental thickness can probably be optimised in order to create safest and most efficient results. It is quite remarkable that multiplying or dividing the segmental thickness by a factor two both result in less safety. Even the most favourable extreme situation ($\gamma_{2,\max}$, corresponding to the highest normal force) is unsafe for very thin or very thick linings.

The tunnel lining with very thin segments ($d_{seg} \approx D/40$) experiences very high normal stress, since the hoop force ($\sigma_0 r$) is only supported by the reduced cross-sectional area. Chapter 4 showed the positive influence of high normal force on the reserve capacity. However, in such thin segments the normal stress is extremely high which results in a very high concrete strain. A small bending moment is already enough to reach the plastic concrete strain ($\varepsilon_c = 1.75 \cdot 10^{-3}$), which reduces the bending stiffness. This phenomenon is explained in figure 5.2. In case of a low modelled normal force the lining collapses when the first plastic spot is observed in the two upper segments. Thereby, the initial bending stiffness is already very low, since the internal lever arm as well as the reinforcement amount is very small. The thin tunnel lining snaps through very easily (figure 5.3). In case of a high modelled normal force the plastic concrete strain is reached even faster. This results in four plastic spots in both upper segments when the ring snaps through. Safety however is not increased significantly. For both extreme situations the collapse is induced by the changing physical properties of the segments.

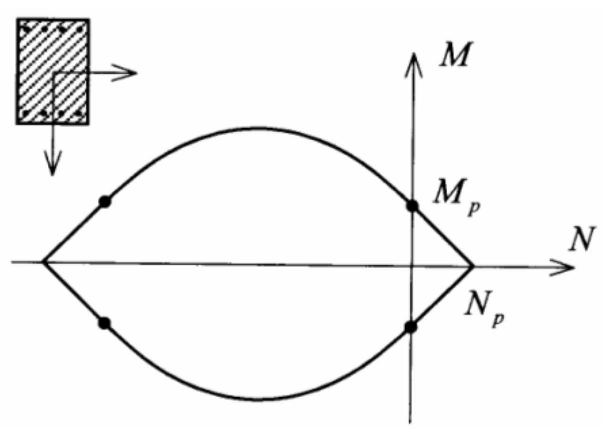

Figure 5.2 – M_p vs. N_p for reinforced concrete cross-sections with identical top and bottom reinforcement. [11]

The tunnel lining with very thick segments ($d_{seg} \approx D/10$) experiences very low normal stress, since the hoop force ($\sigma_0 r$) is supported by the increased cross-sectional area. Despite the relative low normal stress the segments are very stiff since the internal lever arm as well as the reinforcement amount is very large. The bending moment capacity is very high as well. It turned out that the bending moment capacity is too high for this tunnel. Even no plastic behaviour has been observed just before snap through occurs. Since the bedding is very weak now, relative to the segments and Janβen joints, the bedding prevents ovalisation relatively bad. The deformation due to ovalisation is absorbed by the Janβen joints since these are the weakest construction parts. The upper three Janβen joints have rotated so much that they behave like hinges. Finally, the two upper segments will snap through completely. As mentioned before, no plastic behaviour is observed, which implies a dangerous situation since the bending moment in the segments is not even close to the bending moment capacity. This results in a safety factor smaller than one. The same explanation holds for the analysis with a high modelled normal force. For both extreme situations the collapse is induced by the reduced rotational stiffness of the Janβen joints in the upper region.

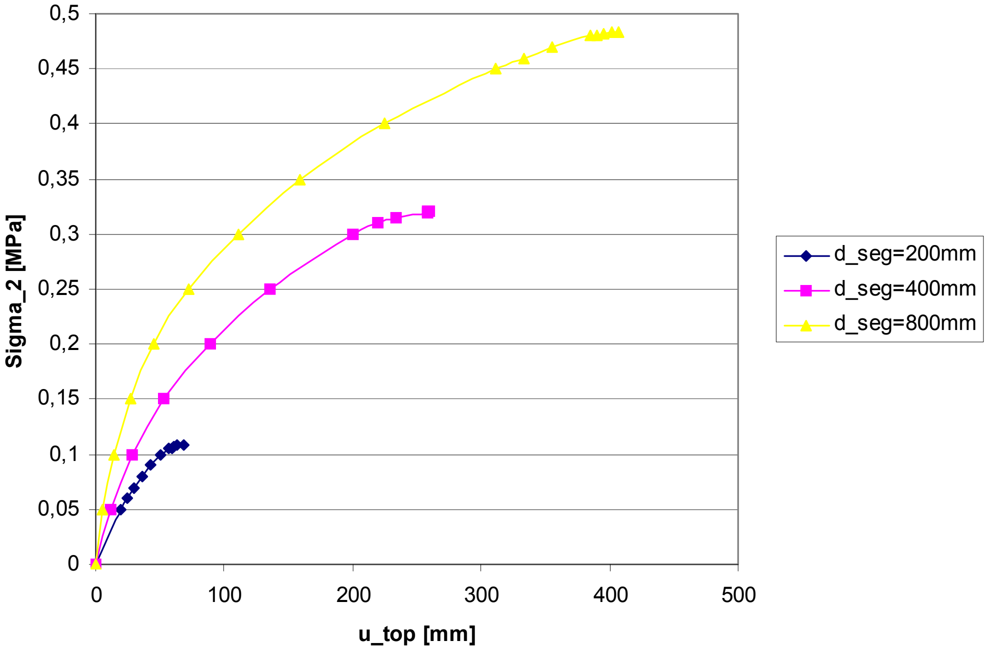

Figure 5.3 – ***u_{top} vs. σ_2 concerning the segmental thickness. These Lines are valid for the lowest occurring normal force (N=2262.5kN).***

For very thin or very thick segments the γ value is always smaller than one. Only for the original segmental thickness the γ value could be slightly lager than one. The segmental thickness seems to be not very robust since a small change results in large safety differences. Therefore, a closer look at practical design methods is needed again (paragraph 5.4). Paragraph 5.3 is about the optimal segmental thickness in relation to the rule of thumb mentioned before.

5.3 Optimal segmental thickness

Figure 5.1 indicates that the segmental thickness has an optimal value in order to create the highest γ value. The magnitude of the γ value gives an indication about the importance to analyse snap through in relation to the practical design methods. An optimal γ value indicates the most efficient value for the parameter under consideration. In this specific case, a certain value for the segmental thickness provides the most efficient use of concrete and reinforcement. In paragraph 4.4 two possible γ values are distinguished.

$$\gamma = \gamma_1 = \frac{M_{\max}}{M_p} < 1 \qquad\qquad \gamma = \gamma_2 = \frac{\sigma_{2,snap\ through}}{\sigma_{2,\ first\ \ plastic\ hinge}} = \frac{\sigma_{2,st}}{\sigma_{2,M_p}} \geq 1$$

Both γ values, γ_1 as well as γ_2, are based on real behaviour and indicates the degree to which the bending moment has developed when snap through occurs. Hence, a lager γ values indicates more efficient use of the specific segmental cross-section.

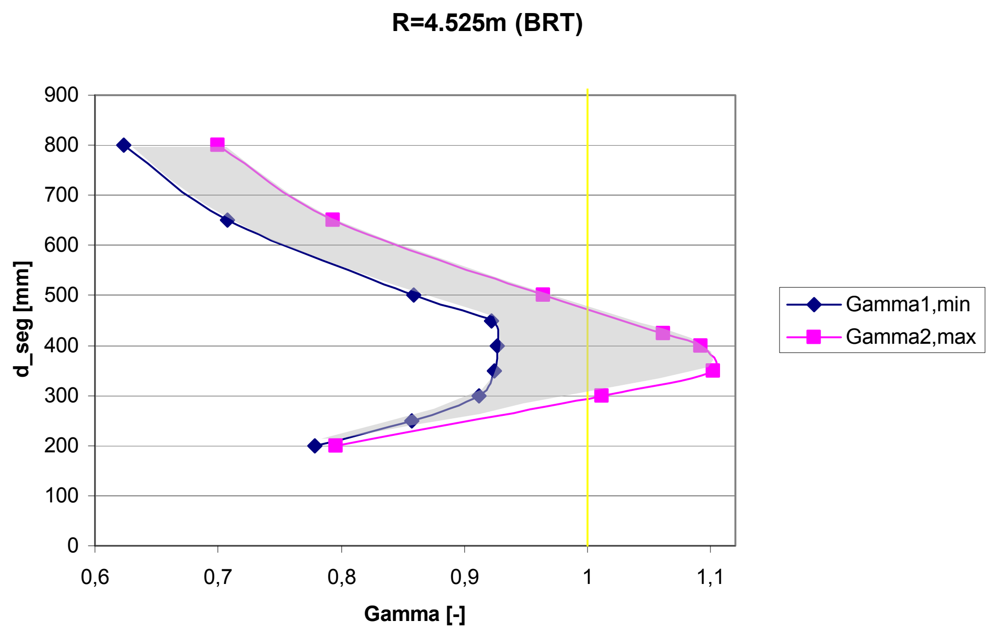

Figure 5.4 – This is actually figure 5.1 extended with some extra results.

Some extra FNL + GNL calculations with different segmental thicknesses (close to the apparent optimum according to figure 5.1) were done to determine the optimal segmental thickness more accurate (figure 5.4). It turned out that the normal force is not important. Both extreme γ values, $\gamma_{1,\min}$ as well as $\gamma_{2,\max}$, corresponding to the minimum and maximum occurring normal force, show the same value for the segmental thickness as optimum. Only very small differences have been observed due to small inaccuracy concerning the maximum modelled normal force. Figure 5.5 displays the optimal segmental thickness for three rings with different diameters.

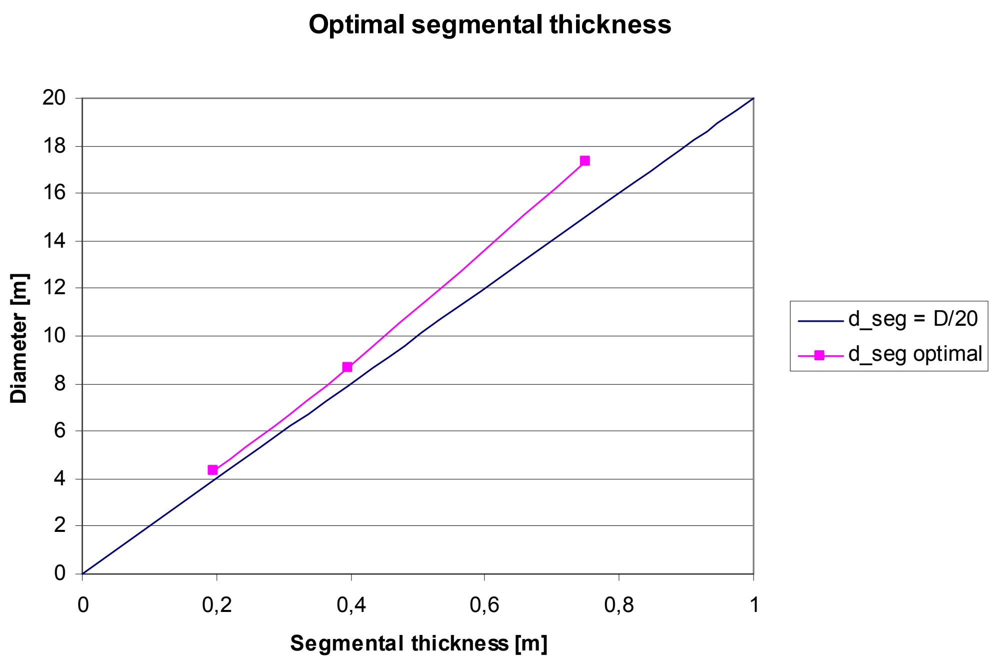

Figure 5.5 – Diameter vs. segmental thickness.

Figure 5.5 demonstrates that the optimal value for the segmental thickness is quite close to the value indicated by the empirical design rule ($d_{seg} = D_i / 20$). The optimal value seems to be linearly related to the diameter. The average ratio $d_{seg,optimal} / D_i$ can be determined.

$$\begin{aligned} 0.195/4.33 &= 1/22.2 \\ 0.395/8.655 &= 1/21.9 \\ 0.75/17.35 &= 1/23.1 \end{aligned} \quad \rightarrow \quad \frac{d_{seg,optimal,average}}{D_i} = \frac{3}{22.2+21.9+23.1} = \frac{1}{22.4}$$

Table 5.2 shows the same ratio for many case studies. The segmental thickness over the diameter ratio for Dutch shield driven tunnels approaches the standard ratio of $1/20$ relatively close. However, most tunnels use a slightly smaller ratio of $1/22$, which is extremely close to the optimal average ratio found in this research. One can conclude that the empirical design rule to determine the segmental thickness is a very good approach for most efficient material use.

Tunnel project	Internal diameter [m]	Segmental thickness [m]	Ratio
Second Heinenoord Tunnel	7.6	0.35	1/22
Westerschelde Tunnel	10.1	0.45	1/22
Sopia Rail Tunnel	8.65	0.40	1/22
Botlek Rail Tunnel	8.65	0.40	1/22
Tunnel Pannerdensch Canal	8.65	0.40	1/22
Green Heart Tunnel	13.3	0.60	1/22
North/South Metro Line Amsterdam	5.62	0.30	1/19
RandstadRail Tunnel Rotterdam	5.8	0.35	1/17
Hubertus Tunnel The Hague	9.4	0.45	1/21

Table 5.2 – Segmental thickness over diameter ratio for Dutch shield driven tunnels.

5.4 Segmental thickness concerning engineering practice

Figure 5.1 showed that the γ value is close to one or even smaller than one. Therefore, the FNL + GNL analysis is compared with the practical methods.

The safety factor λ (explained in paragraph 4.5) is showed in figure 5.6 for the BRT configuration with many different segmental thicknesses. Again, two extreme values, corresponding to the minimum and maximum occurring normal force in the ring, are given for both types of practical analysis. The real λ value is somewhere in between (grey area).

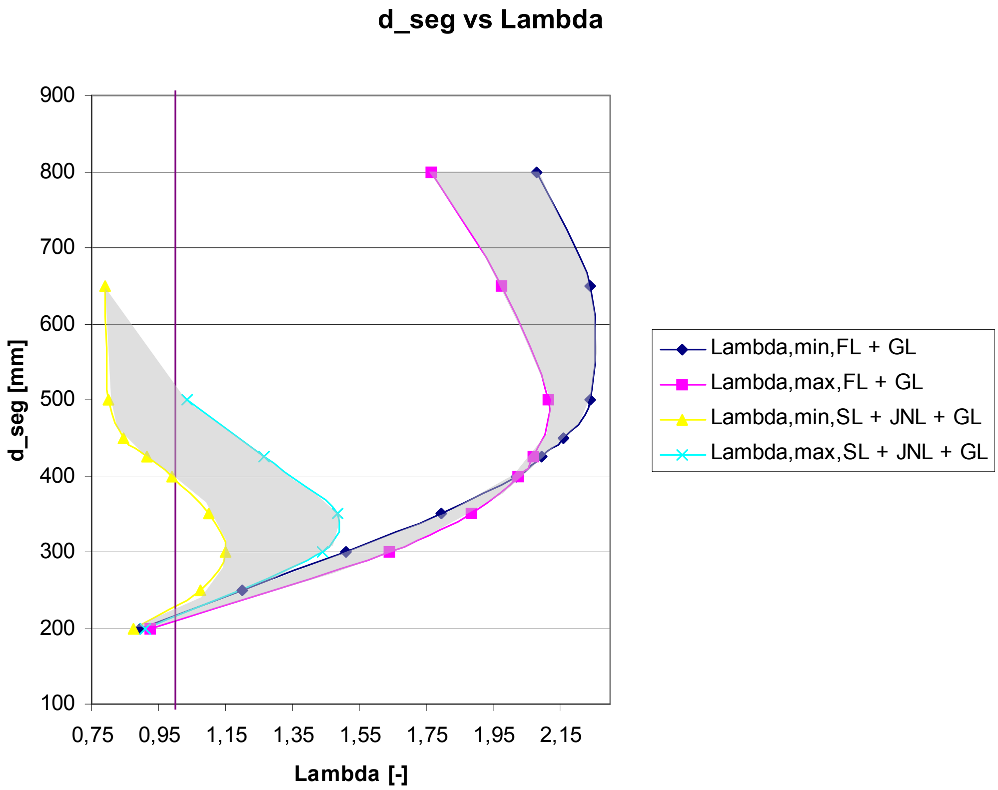

Figure 5.6 – Segmental thickness vs. λ. Only valid for the BRT with varying segmental thickness.

Figure 5.6 shows that the practical methods result in safer (or less unsafe) behaviour. This statement is true since both practical analyses show stiffer behaviour than the scientific analysis, while the bending moment capacity is the same in all analyses. Hence, σ_{2,M_p} has a lower value when using a practical method, which results in more safety.

The lines corresponding to the FL + GL analysis provides safest results. It turned out that the normal force is not important for relative thin linings ($d_{seg}/D_i < 1/20$). Figure 4.4 shows that a higher normal force increases the snap through failure load ($\sigma_{2,st}$). But, also the bending moment capacity increases in case of higher normal force (figure 4.7). Since this calculation is linear elastic, there is a linear relation between σ_{2,M_p} and the bending moment capacity. Hence, $\sigma_{2,st}$ as well as σ_{2,M_p} increase in case of a higher normal force. Apparently these values increase almost proportionally. Snap through is induced by a decreasing bending stiffness of the two upper segments. However, in case of relative thick linings ($d_{seg}/D_i > 1/20$), snap through is induced by a decreasing bending stiffness of the Janβen joints and the normal force points out to be more important. Moreover, the FL + GL analysis roughly provides safe results when the segmental thickness is larger than $D_i/40$.

The lines corresponding to the SL + JNL + GL analysis provide least safe results. It turned out that the normal force is important at all time. In paragraph 4.5 an explanation is given. The λ value can not be determined for relative thick segments because the ring snaps through before the bending moment capacity has been reached. This has been observed for thinner segments when the extreme situation corresponding to the maximum occurring normal force is considered. For relative thin linings this analysis provides safest results. If $1/38 < d_{seg}/D_i < 1/22$, the results will be safe at all time. For segmental thicknesses outside this interval the analysis probably provides unsafe results. When the segments become very thin ($d_{seg}/D_i < 1/40$) or very thick ($d_{seg}/D_i > 1/17$) the results will be unsafe at all time. However, snap through in case of extreme thick segments ($d_{seg}/D_i > 1/13$) would be noticed by the engineer since the non-linear behaviour of the Janβen joints is included.

Note: the safest segmental thickness in case of a practical analysis (the maximums in figure 5.6) does not correspond to the most material efficient segmental thickness (paragraph 5.3; $d_{seg} = D/21.9 = 8.655/21.9 = 0.395m$).

5.5 Conclusion

Again, the situation concerning snap through is worse than Blom [4] predicted. It turned out that the γ value is always close to one or smaller than one for all segmental thicknesses, instead of $\gamma = 3$ as Blom predicted for the BRT. The segmental thickness is an exponential parameter; a small change results in large safety differences. Since γ is close to the critical point for snap through, a closer look at practical design methods was carried out to discover whether or not practical assumptions are still valid.

Despite the wrong results, it is concluded that everyone can safely go to bed when using the FL + GL (linear elastic) analysis. Snap through will never occur before the bending moment capacity has been reached if $d_{seg} > D_i/40$. More awareness of reality is required for everyone who uses the SL + JNL + GL analysis (linear elastic with non-linear Janβen joints). For segmental thicknesses outside the interval $1/38 < d_{seg}/D_i < 1/22$ it is more likely that the analysis provides unsafe results. A larger possibility exists that snap through takes place without any plastic hinge. Since it is not unthinkable that snap through is the decisive failure mechanism, it is very dangerous if one realises that the practical methods to analyse a shield driven tunnel will not notice this failure mechanism. The tunnel design is probably based on the wrong criterion.

This conclusion is only valid concerning the segmental thickness of the tunnel. In this specific research it was not possible to determine the ‘exact’ reserve capacity since the influence of the normal force can not be included. However, based on specific parameter sets it was possible to indicate minimum and maximum values for the reserve capacity.

This research confirms the correctness of the empirical rule to determine the segmental thickness in relation to the radius. Most efficient material use is reached if $d_{seg} \approx D_i/22$.

6 SIMPLIFICATION

In chapter 3 a model for the tunnel ring surrounded by soil was chosen and explained as well. The calculations were done by using computer software, since the model is quite large and the analysis very advanced. A physical and geometrical non-linear analysis was carried out for a model that contains many elements. This chapter is about simplifying the computer model and reducing the engineering time needed to determine the real load bearing capacity. First of all, a simple theoretical model to analyse snap through failure will be introduced. Secondly, snap through is affected by the radius, the soil and the Janβen joints. The influence on the load bearing capacity and the snap through character (global or local instability) is analysed. In the end the load bearing capacity of this model is calibrated to some results corresponding to the computer model. A clear practical procedure to consider snap through is introduced. The software application Maple is used (appendix E).

6.1 Modelling

The simplest way to model a tunnel ring is to schematise one quarter of the ring as an infinite stiff straight beam, standing with an angle of $45°$ relative to the horizontal direction (figure 6.1). The support at the left upper end of the beam (A) can be modelled as a rotational spring c_1 and a hinge which can move freely in vertical direction. This support represents the connection with the other part of the tunnel. On this end, also a vertical load F is applied, which represents σ_2. The support at the right lower end of the beam (B) can be modelled as a rotational spring c_2 and a hinge which can move freely in horizontal direction. This support represents the connection with the other part of the tunnel. But, at this end of the beam the support is extended with a translational spring k in horizontal direction, which represents the support from the soil at the sides.

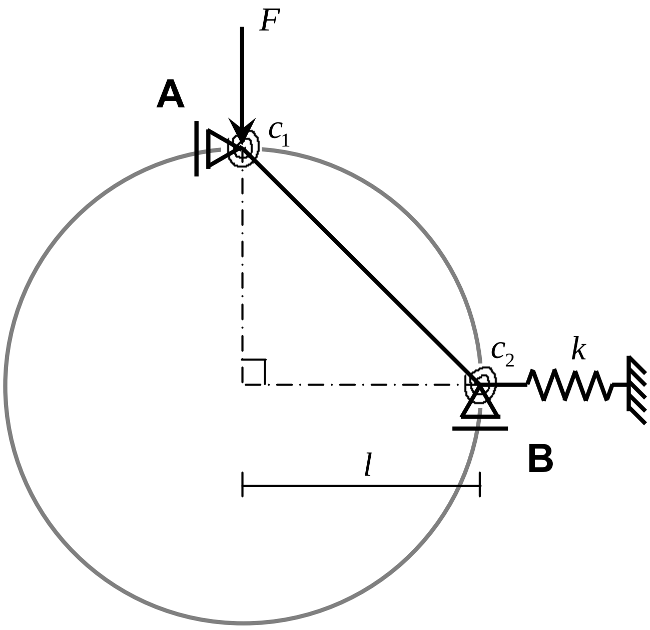

Figure 6.1 – A simple model to analyse snap through.

The behaviour of this model is given by three types of equations: kinematic, constitutive and equilibrium equations.

6.1.1 Kinematic equations

Kinematic equations give the relation between the change in geometry (deformation) and the displacement caused by that change in geometry. In this case the rotation of the beam θ causes a vertical displacement w of point A of the beam (figure 6.2). In this case the beam is standing with an initial angle of $45°$ relative to the horizontal direction. The initial angle is defined as the variable φ, since it can vary in general. The angle $\varphi-\theta$, relative to the horizontal direction, determines the new configuration of the rotated beam.

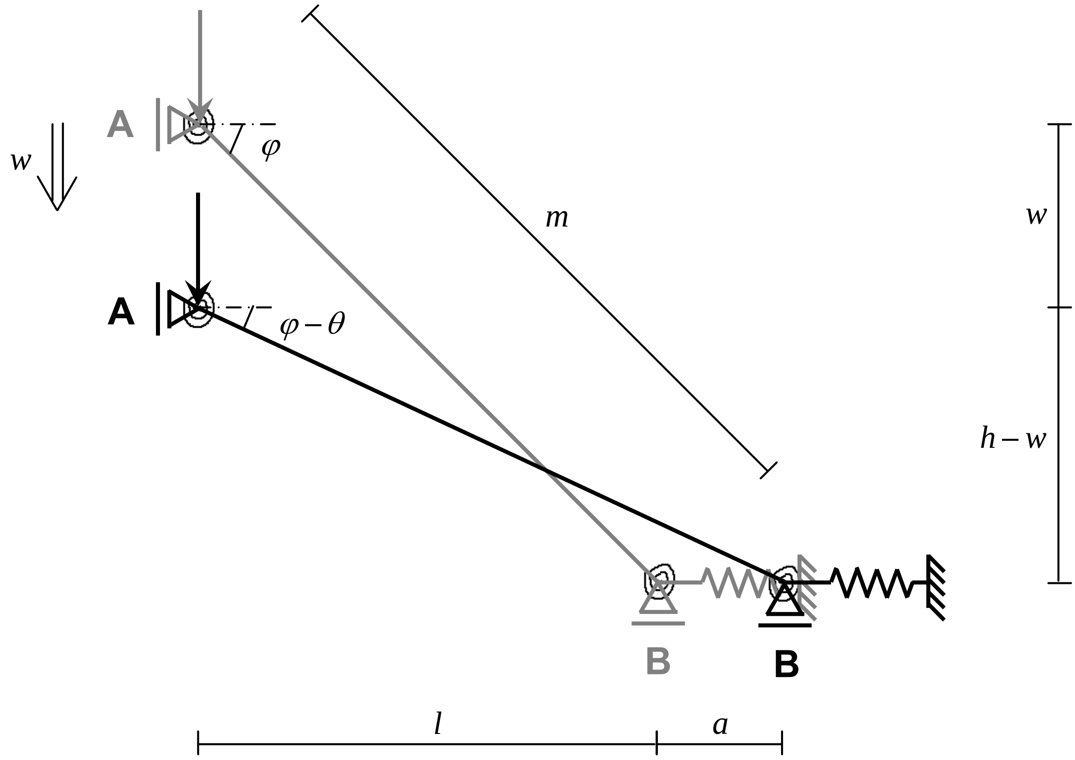

Figure 6.2 – The rotation θ of the beam causes a vertical displacement w of point A. Grey is the initial situation and black is the rotated situation.

From this figure the next kinematic equations can be defined easily. First of all, the constant length of the beam m is determined, in which l is the initial horizontal length. Parameter h is the initial vertical length.

$$m = \frac{l}{\cos(\varphi)} \quad \rightarrow \quad a = m\cos(\varphi-\theta) - l$$

$$h = l\tan(\varphi) \quad \rightarrow \quad w = h - m\sin(\varphi-\theta)$$

6.1.2 Constitutive equations

Constitutive equations give the relation between the internal forces and the change in geometry (deformation) caused by these internal forces. For convenience linear elastic stiffness behaviour of the rotational springs and the translational spring is presumed. R is the reaction force in the translational spring k caused by the displacement a. M_1 and M_2 are the reaction moments in the rotational springs c_1 and c_2, caused by the rotation θ.

$$R = ka \qquad M_1 = c_1\theta \qquad M_2 = c_2\theta$$

6.1.3 Equilibrium equations

Equilibrium equations give the relation between the internal forces and the external forces. There must be equilibrium of forces (horizontally and vertically) and equilibrium of moments. A_h is the horizontal reaction force in A and B_v is the vertical reaction force in B.

$$\sum F_h = 0 \quad \rightarrow \quad R - A_h = 0 \quad \rightarrow \quad A_h = R$$

$$\sum F_v = 0 \quad \rightarrow \quad F - B_v = 0 \quad \rightarrow \quad B_v = F$$

$$\sum M\Big|_A = 0 \quad \rightarrow \quad F(l+a) - M_1 - R(h-w) - M_2 = 0 \quad \rightarrow \quad F = \frac{M_1 + R(h-w) + M_2}{(l+a)}$$

Three sets of equations are available now. In order to obtain the solution of this stability problem, the kinematic equations must be substituted into the constitutive equations and the constitutive equations must be substituted into the equilibrium equations. Very useful and explicit functions for $w(\theta)$ and $F(\theta)$ are determined now. Only the length l (radius of the ring), the angle φ and the stiffness parameters k, c_1 and c_2 are initial values which have to be quantified.

$$w(\theta) = l\tan(\varphi) - \frac{l\sin(\varphi-\theta)}{\cos(\varphi)} \quad \rightarrow \quad \theta(w) = \varphi + \arcsin\left(\frac{w\cos(\varphi) - l\sin(\varphi)}{l}\right)$$

$$F(\theta) = \frac{c_1\theta + k\left(\dfrac{l\cos(\varphi-\theta)}{\cos(\varphi)} - l\right)\left(\dfrac{l\sin(\varphi-\theta)}{\cos(\varphi)}\right) + c_2\theta}{\left(\dfrac{l\cos(\varphi-\theta)}{\cos(\varphi)}\right)}$$

The function $\theta(w)$ can be substituted into $F(\theta)$, which will lead to the explicit function $F(\theta(w)) = F(w)$. This expression is too large to write down.

6.1.4 The creation of a continuous initial horizontal length l

In order to predict the character of the snap through failure (global or local failure), different beams with a different initial angle ($0 \le \varphi \le \pi/4$) must be considered (figure 6.3). The result will be a maximum load F, for every single beam with a different initial angle. That enables one to identify the most sensitive spot to snap through along the ring.

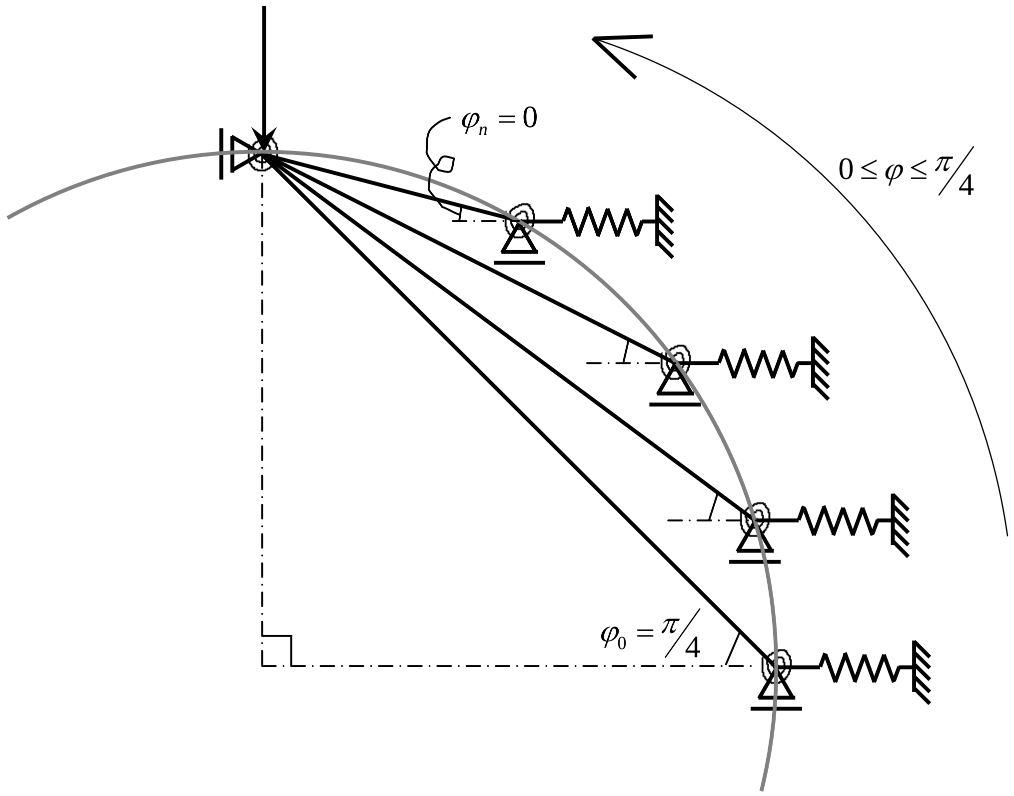

Figure 6.3 – Different initial angles φ must be analysed to find out the weakest spot along the ring.

As one can see in figure 6.3 and 6.4, the initial horizontal length l will vary too. But, the initial horizontal length can be written as a continuous function $l(\varphi, r)$, where r is the radius of the specific ring that is considered.

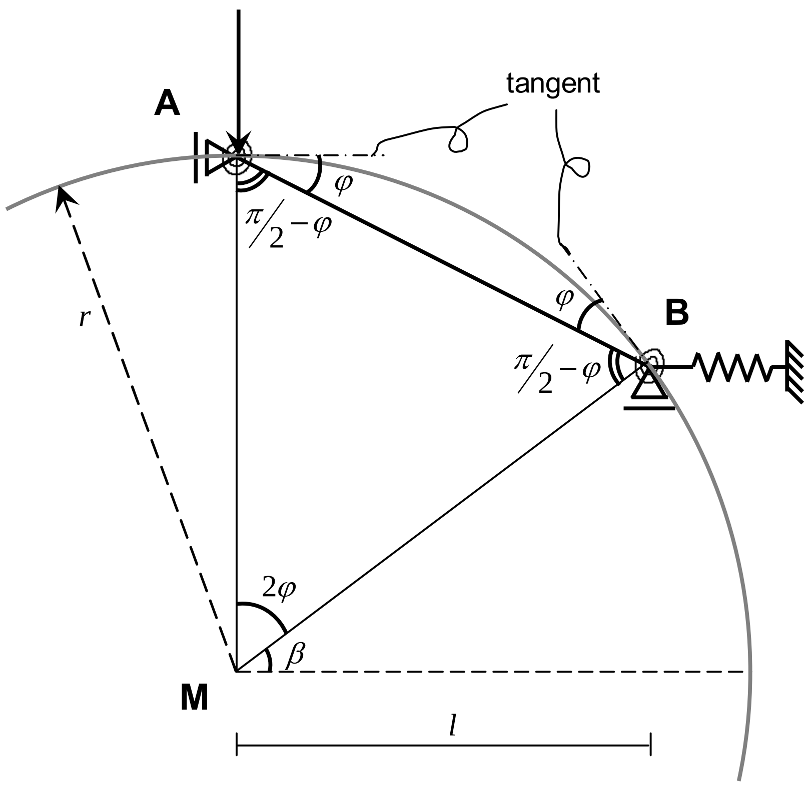

Figure 6.4 – The features of the isosceles triangle ABM determine l .

The feature that the summation of the three angles of a triangle is π radials has been used. Since the triangle ABM is an isosceles triangle, the next features are known.

$$\angle AMB = \pi - \angle MAB - \angle ABM = \pi - 2\angle MAB = \pi - 2\left(\frac{\pi}{2} - \varphi\right) = 2\varphi$$

$$l(\varphi, r) = r\cos(\beta) = r\cos\left(\frac{\pi}{2} - 2\varphi\right)$$

Note: If the beam is standing with an initial angle of $45°$ relative to the horizontal direction, than the initial horizontal length is equal to the radius of that specific ring, $l = r$ (basic situation, figure 6.1).

From now on, it is possible to describe the behaviour of the model in figure 6.1 for every combination of the basic parameters: r, φ, k, c_1 and c_2.

6.2 The influence of the basic parameters: r, φ, k, c_1 and c_2

Until now, only equations have been derived. This paragraph describes the qualitative influence that the basic parameters r, φ, k, c_1 and c_2 have on the behaviour of the model. This will be clarified by some graphs.

First of all, the influence of the stiffness parameters k, c_1 and c_2, and the interaction between them, will be analysed. The radius $r = 10m$ and the initial angle $\varphi = 45° = \pi/4rad$ (basic situation, figure 6.1). Two extreme situations can be considered.

- k has a certain value ($10N/m$) and $c_1 = c_2 = 0Nm/rad$.
- The other way around: $k = 0N/m$ and c_1 and c_2 have a certain value (both $10Nm/rad$).

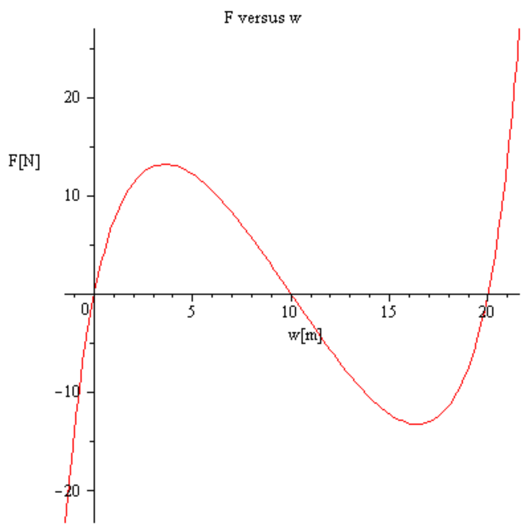

Figure 6.5 – Behaviour of the model for k = 10N/m and c_1 = c_2 = 0Nm/rad .

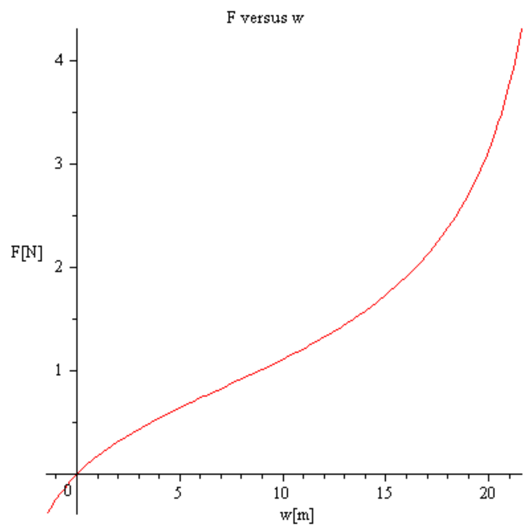

Figure 6.6 – Behaviour of the model for k = 0N/m and c_1 = c_2 = 10Nm/rad .

Figure 6.5, the first extreme situation, indicates a clear snap through behaviour. This graph looks just the same as the right graph in figure 1.8 from the literature study [7]: the characteristic graph for snap through of a well known model. Figure 6.6, the other extreme situation, does not show snap through at all. This is not very strange, since the reaction moments in the rotational springs always increase if the rotation of the beam increases (as a result of the increasing force F). Hence, F must increase in order to push point A downwards further, which means increasing w.

It turns out that, if all stiffness parameters k and c_1 and c_2 are non zero values, a combination of figure 6.5 and 6.6 is observed. Figure 6.7 is a situation for which all stiffness parameters are not equal to zero. Still the same radius and initial angle are used. This specific combination of these parameters approximately represents the splitting point for snap through. If k is smaller or the summation of c_1 and c_2 is larger than the values in figure 6.7, snap through will not occur. But, if k is larger or the summation of c_1 and c_2 is smaller than the values in figure 6.7, snap through will occur.

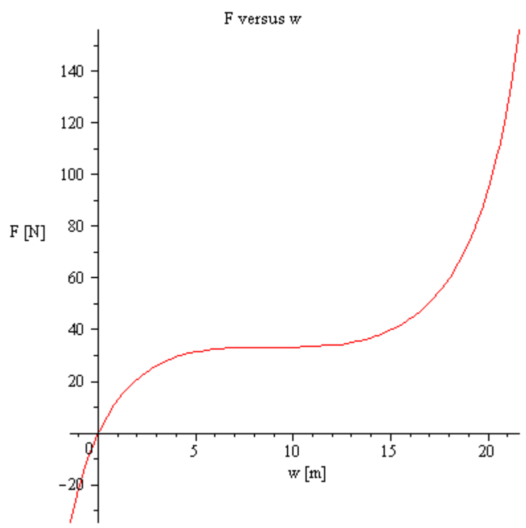

Figure 6.7 – Behaviour of the model for k = 10N/m and c_1 = c_2 = 600Nm/rad .

Note: From the equilibrium equations (equilibrium of moments) it is clear that superposition of M_1 and M_2 is allowed, since both of them depends linearly on the rotated angle θ.

However, the behaviour of the model shown in figure 6.6 and 6.7 is not representative for the real behaviour. The moments in the rotational springs will increase linearly with the rotation θ. The rotational springs are theoretically able to increase till infinitely, which means that the snap through failure does not occur anymore for some combinations of the stiffness parameters. In reality the weakest spots in the ring are the longitudinal joints, which can be modelled according to Janβen (paragraph 3.3). $M = c\theta$, with:

$$c = \frac{b l_t^2 E_c}{12} \qquad \text{under the condition that} \qquad \theta \leq \frac{2N}{E_c b l_t}, \qquad \text{and}$$

$$c = \frac{9 b l_t E_c \left(\frac{2M}{N l_t} - 1 \right)^2}{8N} M \qquad \text{under the condition that} \qquad \theta > \frac{2N}{E_c b l_t}.$$

Where:	b	=	Width contact area longitudinal joint (segmental width)
	l_t	=	Height contact area longitudinal joint
	E_c	=	Young's modulus concrete
	N	=	Normal force in ring
	M	=	Moment in longitudinal joint

The first branch of the $M-\theta$ relation according to Janβen is also linear, the second branch is non-linear. The non-linear branch depends on the rotation itself. At a certain moment the longitudinal joint (rotational spring) has lost his stiffness almost completely. Therefore, the moment in the longitudinal joints can increase barely. These more accurate stiffnesses for the rotational springs c_1 and c_2 are used from now on. Realistic values are used for all parameters to illustrate the behaviour of the longitudinal joints (figure 6.8). Figure 6.9 shows the behaviour of the model in the extreme case that $k = 0N/m$ and c_1 and c_2 behave like a Janβen joint with the characteristics from figure 6.8. The fact that this problem is geometrical non-linear explains the extreme increase of the force F in figure 6.9. The reaction moment in the rotational springs is already constant at that time.

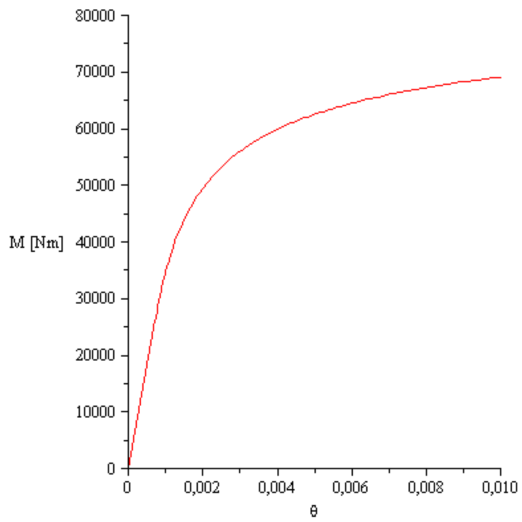

Figure 6.8 – ***M - θ relation according to Janβen. N = 1000kN , b = 1m , E = 15000N/mm^2 and l_t = 0.170m***

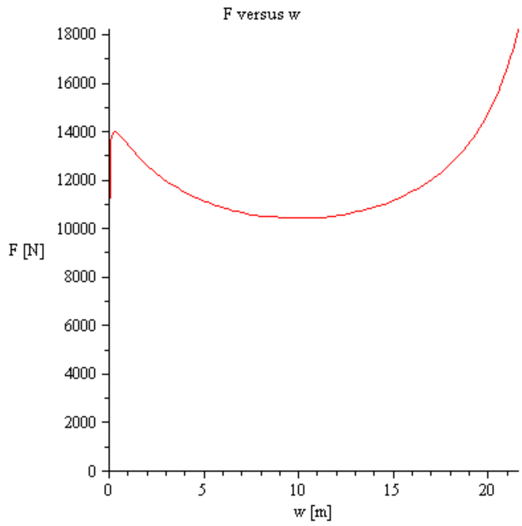

Figure 6.9 – ***Behaviour of the model for k = 0N/m and c_1 and c_2 according to figure 6.8***

In reality, the soil stiffness is non-linear as well. Despite this fact, in this model the linear stiffness of the soil is not improved, since the system can fail as a consequence of snap through. This is very important in order to answer the question whether or not snap through occurs on a global scale. A realistic and frequently used value for the linear soil stiffness k can be obtained [4].

$$\frac{k}{A} = \frac{E_{oed}}{2r}$$

Where:	E_{oed}	=	Oedometer stiffness of soil
	r	=	External radius of the tunnel
	A	=	Surface for which the bedding is represented by the spring k.

An assumption for k must be made to show the improved behaviour of the model when all stiffness parameters are not equal to zero. In this case $r = 10m$ and $A = 5m^2/m$ because only the soil support at the upper half of the ring at the right side has been modelled (one quarter of the ring). A realistic value for $E_{oed} = 38MPa$. From the equation above it turns out that $k = 9.5MN/m$. The "new" behaviour of the model, by using the realistic values for all parameters, is shown in figure 6.10. Figure 6.5 and 6.10 look exactly the same. The longitudinal joints have hardly any influence on the snap through behaviour.

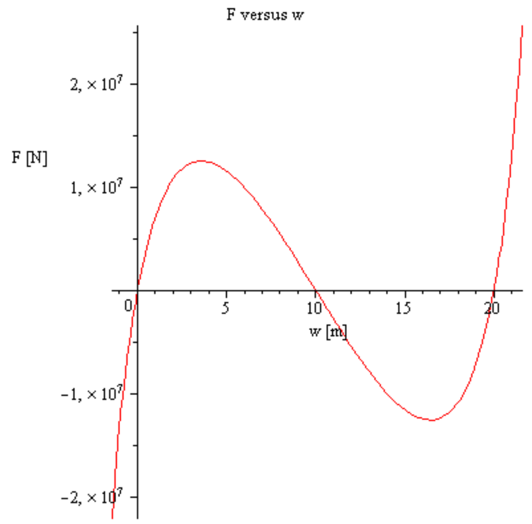

Figure 6.10 – More realistic behaviour of the model.
k = 9.5MN/m and c_1 and c_2 according to figure 6.8

Now the influence of the stiffness parameters k, c_1 and c_2, and the interaction between them is clear. *In the second step to study the behaviour of the model, the influence of the radius r will be analysed.* Again two extreme situations will be considered.

- k has a certain value ($9.5MN/m$) and $c_1 = c_2 = 0Nm/rad$ (figure 6.11).
- The other way around: $k = 0N/m$ and c_1 and c_2 according to figure 6.8 (figure 6.12).

The initial angle φ is still $45° = \pi/4rad$.

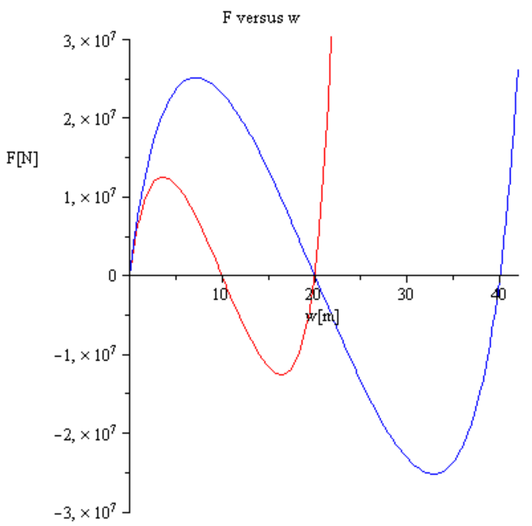

Figure 6.11 – Behaviour of the model for
k = 9.5MN/m and c_1 = c_2 = 0Nm/rad .
red line: r = 10m , blue line: r = 20m

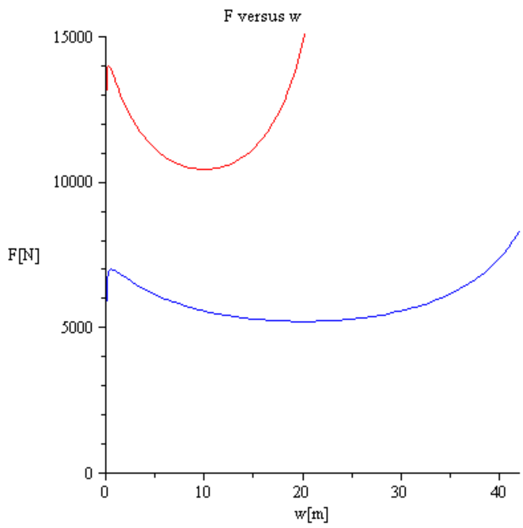

Figure 6.12 – Behaviour of the model for k = 0MN/m
and c_1 and c_2 according to figure 6.8.
red line: r = 10m , blue line: r = 20m

Figure 6.11, the first extreme situation, clearly shows an increase of both coordinates w and F with a factor 2. The functions $w(\theta)$ and $F(\theta)$ clarify this multiplication since l is twice as big. This statement does not hold for the second extreme situation. After the enlargement of the radius by a factor 2, the coordinate w is enlarged by a factor 2, but the coordinate F

is decreased by a factor 2 (figure 6.12). But, also this behaviour is underpinned by the functions $w(\theta)$ and $F(\theta)$. In order to obtain the same moment in the rotational springs, the load F must decrease, since the lever arm increase (r is twice as big).

It turns out that the value for k dominates the system so much, that varying the radius does not influence the behaviour at all. Only the coordinates w and F are increased by a factor 2. The functions $w(\theta)$ and $F(\theta)$ clarify this multiplication since l is twice as big. The total enlargement is shown in figure 6.13. Since the blue line is an enlargement of figure 6.10 (figure 6.10 is exactly the same as the red line in figure 6.13), the blue line looks exactly the same as the graph in figure 6.5 as well.

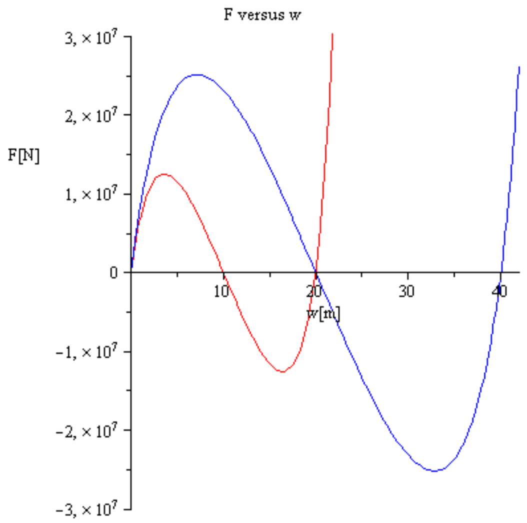

Figure 6.13 – More realistic behaviour of the model.
k = 9.5MN/m and c_1 and c_2 according to figure 6.8.
red line: r = 10m , blue line: r = 20m

In the last step to study the behaviour of the model, the influence of the initial angle φ will be analysed. Again, two extreme situations will be considered, each of them with different values for the stiffness parameters.

- k has a certain value ($0.95MN/m$, $9.5MN/m$ or $95MN/m$) and $c_1 = c_2 = 0Nm/rad$.
- The other way around: $k = 0N/m$ and c_1 and c_2 according to the Janβen characteristics in figure 6.8. But, l_t has three different values ($0.170m$, $0.340m$ or $0.510m$).

	1	2	3	4	5	6
k	$0.95MN/m$	$9.5MN/m$	$95MN/m$	-	-	-
N	-	-	-	$1000kN$	$1000kN$	$1000kN$
b	-	-	-	$1m$	$1m$	$1m$
$\boldsymbol{E_c}$	-	-	-	$15000N/mm^2$	$15000N/mm^2$	$15000N/mm^2$
$\boldsymbol{l_t}$	-	-	-	$0.170m$	$0.340m$	$0.510m$

Table 6.1 – Three different cases for each extreme situation will be considered.

Table 6.1 shows six different situations which will be considered. The maximum load F will be plotted against the angle β (figure 6.14 and 6.15). The definition of β is given in figure 6.4.

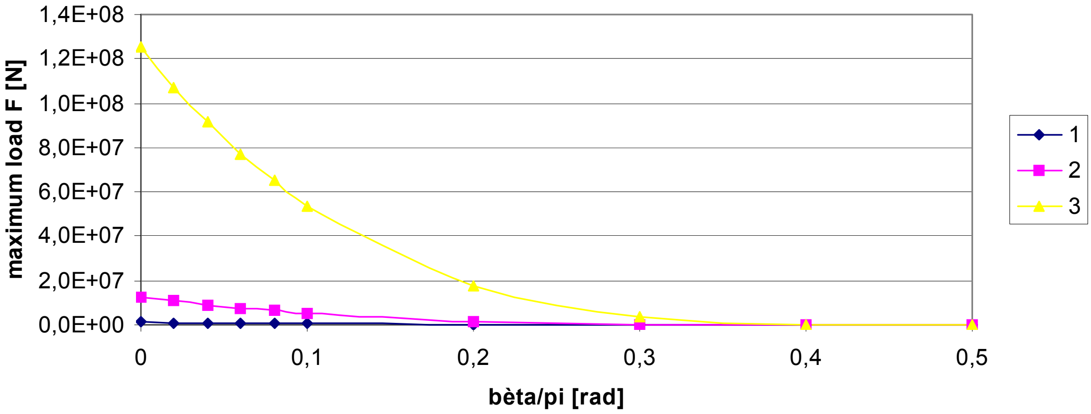

Figure 6.14 – F versus β. Situation 1, 2 and 3.

All curves in figure 6.14 have the same shape. All three cases show a maximum load $F = 0$, if $\beta / \pi = 0.5 \Rightarrow \beta = 0.5\pi$ (initial angle $\varphi = 0$). Hence, for the first extreme situation (1, 2 and 3), different values for k do not influence the most sensitive spot to snap through. But, the influence of k in general decreases when β increases, because k contributes less to the maximum load F when β increases.

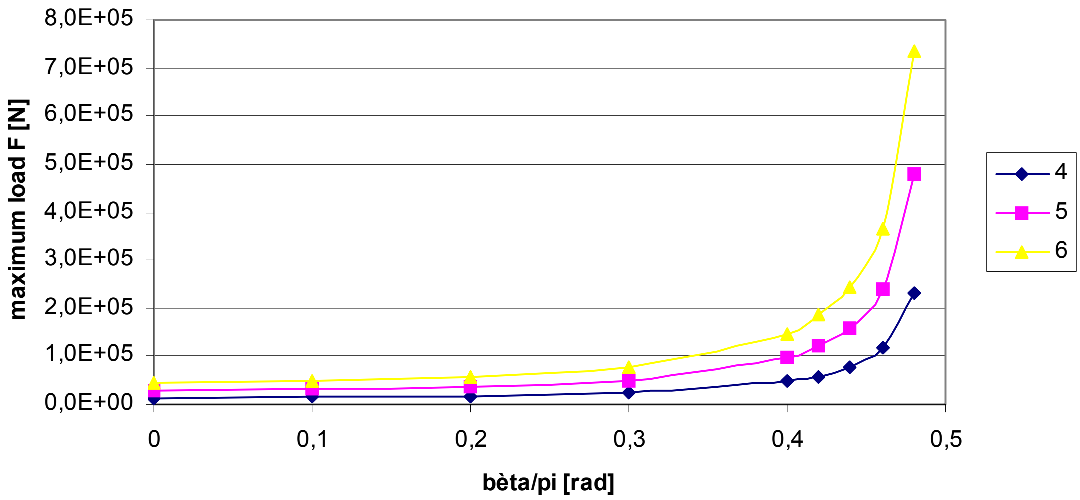

Figure 6.15 – F versus β. Situation 4, 5 and 6.

All curves in figure 6.15 have the same shape. The maximum load F in all three cases tend to go to infinity, if $\beta / \pi = 0.5 \Rightarrow \beta = 0.5\pi$ (initial angle $\varphi = 0$). Hence, for the other extreme situation (4, 5 and 6), different Janβen characteristics for c_1 and c_2 do not influence the most sensitive spot to snap through. But, the influence of c_1 and c_2 in general increases when β increases, because c_1 and c_2 contribute more to the maximum force F when β increases.

In reality all stiffness parameters are non zero values. It turns out that, if the realistic values from figure 6.13 are used, a minimum has been found for the maximum load F somewhere in the top region of the ring. This is a combination of situation 2 and 4. For these high β values, the radius r is an important parameter as well (figure 6.16).

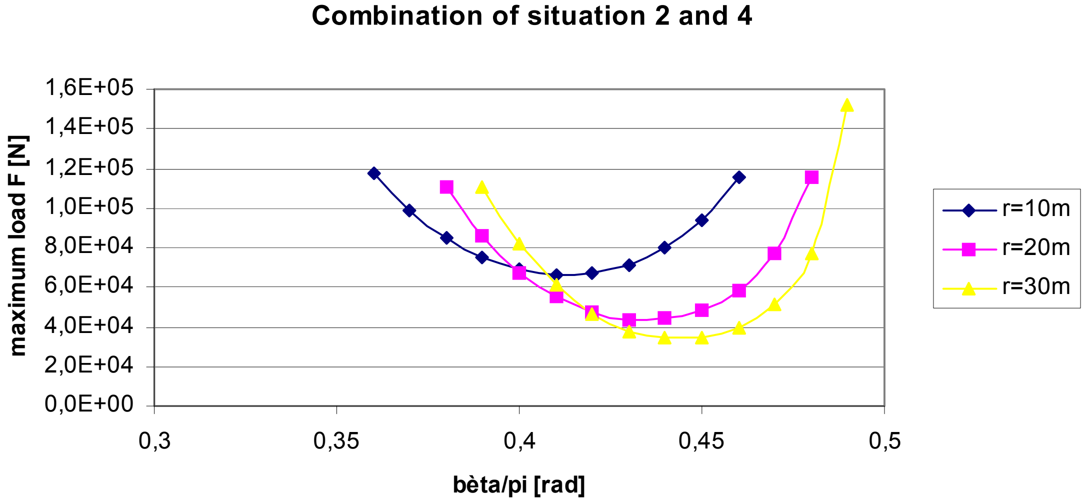

Figure 6.16 – F versus β curves show local instability for k = 9.5MN/m , N = 1000kN , b = 1m , E = 15000N/mm^2 and l_t = 0.170m .

Regardless the radius, figure 6.16 shows a local instability. According to this analysis the top region of the ring is the most sensitive part to snap through. Furthermore, figure 6.16 gives some information about the radius with respect to snap through. If the radius increases, the maximum load F, which that specific structure can carry, decreases. A more local snap through failure is observed in case of a larger radius as well.

Figure 6.16 shows the result for a regular situation. To be more precise about the range for β, with respect to the most likely place for snap through to occur, two extreme situations are considered. The result will be more accurate values for the boundaries of the range for β (figure 6.17).

- The lowest value for β (lower boundary of the range) is observed when k and r are small and the parameters for the Janβen joint are large. So: $k = 0.95 MN/m$, $r = 3m$, $N = 1000kN$, $b = 1m$, $E_c = 15000 N/mm^2$ and $l_t = 0.510m$. The result will be the lower boundary for β.
- The highest value for β (upper boundary of the range) is observed when k and r are large and the parameters for the Janβen joint are small. So: $k = 95 MN/m$, $r = 30m$, $N = 1000kN$, $b = 1m$, $E_c = 15000 N/mm^2$ and $l_t = 0.100m$. The result will be the upper boundary for β.

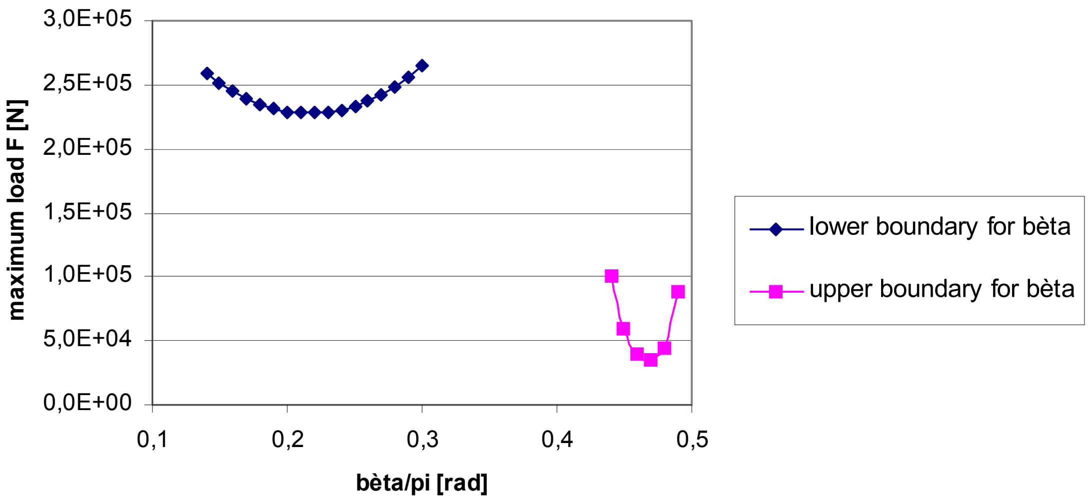

Figure 6.17 – These two curves (F versus β) determine the extreme boundary values of the range for β.

Conclusion
The objective of this paragraph was to obtain qualitative knowledge about the character of snap through and the load bearing capacity influenced by k, c_1, c_2 and r. Therefore, an analytical model was developed. All important parameters were studied to find out there influence on the behaviour of the model.

To summarize all these findings with respect to global or local snap through and the failure load, the influence of the important parameters is given in table 6.2. The second column gives an indication on what happens with the character of the snap through failure, if the specific parameters increase. The same philosophy holds for the third column.

Increase parameter	**Character of snap through**	**Failure load F**
k	More local	increase
c_1	More global	increase
c_2	More global	increase
r	More local	decrease

Table 6.2 – The influence of the parameters on the character and the failure load of snap through.

The extreme range for β is determined by figure 6.17. The coordinates for β of these two convex functions, for which the coordinates of F are minimum, are $\beta = 0.22\pi$ and $\beta = 0.47\pi$. Hence, the most sensitive region along the ring to snap through is defined as $0.22\pi < \beta < 0.47\pi$ (or $0.14\pi > \varphi > 0.015\pi$). If more realistic values were used (BRT), than $\beta \approx 0.38\pi$ (or $\varphi \approx 0.06\pi$), which indicates a quite local snap through failure.

This theoretical analysis is just an approach of the mechanism. The bending stiffness of the lining is not included, as well as the circular shape. The loading σ_2 and the soil support are concentrated in one point, which is of course not true. However, the model was sophisticated enough to attain the objective mentioned above.

6.3 Calibration

The model from paragraph 6.1 will be calibrated for two different situations. In the first situation, snap through is induced by the reduced rotational stiffness of the Janβen joints in the upper region. Both upper segments will snap through completely, which is called Janβen failure from now on. In the second situation, snap through is induced by the changing physical properties of the segments. Both upper segments will snap through partly, since the bending stiffness has been reduced somewhere along both upper segments ($\varepsilon_c = 1.75 \cdot 10^{-3}$ has been reached), which is called segmental failure from now on. These two situations are the only possible inducements for snap through. For each situation table 6.3 shows a specific parameter set. These two examples are already considered by using the computer model.

Segmental failure	**Janβen failure**
$N = 2262.5kN$	$N = 2262.5kN$
$r = 4.525m$	$r = 4.525m$
$d_{seg} = 400mm$ (BRT)	$d_{seg} = 800mm$
$l_t = 170mm$	$l_t = 340mm$
$B45$	$B45$
$E_{oed} = 38MPa$	$E_{oed} = 38MPa$
$k_b = 8.3978MN/m^2$	$k_b = 8.3978MN/m^2$
$\alpha_{bedding} = 90°$	$\alpha_{bedding} = 90°$
$n_{seg} = 7$	$n_{seg} = 7$
$\sigma_0 = 0.5MPa$	$\sigma_0 = 0.5MPa$
$\omega_{0,\min} = 0.18\%$	$\omega_{0,\min} = 0.18\%$
$c = 35mm$	$c = 35mm$
$\phi_{rebar} = 10mm$	$\phi_{rebar} = 10mm$

Table 6.3 – Abstract of the parameters for both situations.

In order to compare the computer model with the simplification, both models must be linked. Hence, the ovalisation loading σ_2 must be written as a function of the force F and the soil stiffness k must be written as a function of the reaction force R and the horizontal displacement a.

6.3.1 Janβen failure

The straight beam from the simplification is projected in between the two Janβen joints in order to simulate the Janβen failure. Hence, according to figure 6.4 and figure 6.18 $\beta = 3\pi/14$ (and $\varphi = \pi/7$) since this tunnel ring has seven segments. For convenience the radial directed ovalisation loading σ_2 is integrated for $0 \le \phi \le \pi/4$ to determine the force F (figure 6.18). This is approximately the average location for which the ring snaps through in general. Note: the Janβen failure is the most global collapse possible.

$$F = \int_0^{\pi/4} \sigma_2 \cos(2\phi) d\phi \cdot r = r\sigma_2 \left[\tfrac{1}{2}\sin(2\phi)\right]_0^{\pi/4} = \tfrac{1}{2} r\sigma_2 \qquad \rightarrow \qquad \sigma_2(F) = 2F/r$$

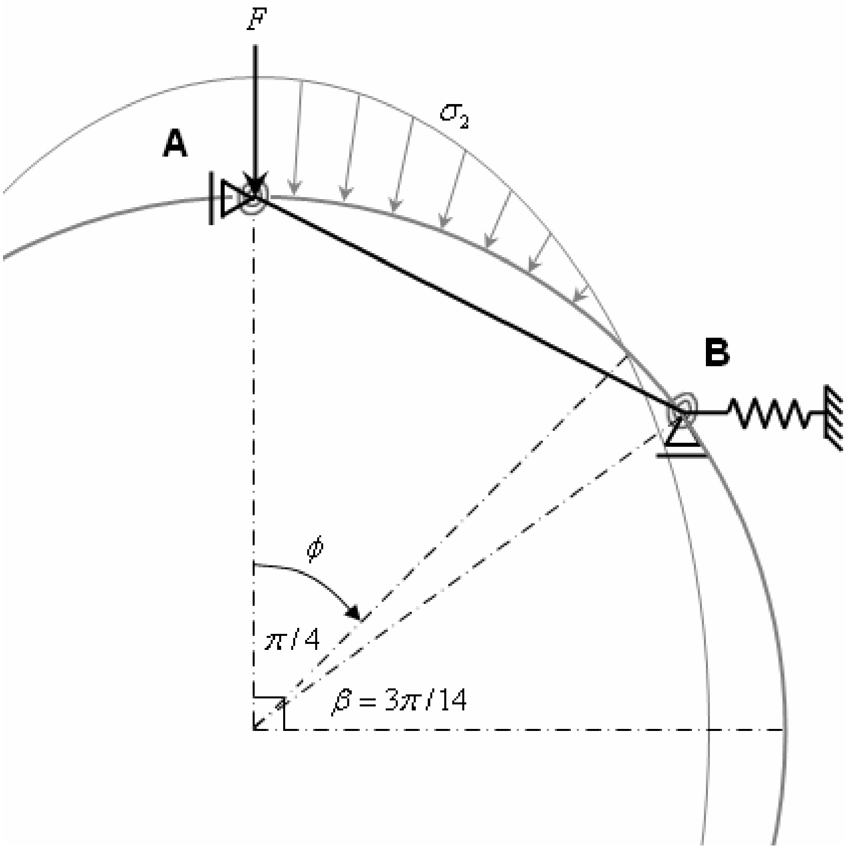

Figure 6.18 – σ_2 is integrated for $0 \le \phi \le \pi/4$ to determine F .

The soil stiffness k is determined in a more advanced way by using the computer models. The normal force, shear force and displacement in horizontal direction in the Janβen joint (point B, figure 6.18) were registered for many load steps. The reaction force R in the horizontal translational spring k is a summation of the horizontal force components: $R = N_{hor} + V_{hor}$. Figure 6.19 shows the diagram for R versus a . A fourth order expression is given for this specific relation.

$$R = -0.000006a^4 + 0.0022a^3 - 0.291a^2 + 18.098a + 1515.9$$

One must realise that the derivative of this expression provides a continuous expression for the stiffness of the horizontal spring k .

$$k = R' = -0.000024a^3 + 0.0066a^2 - 0.582a + 18.098 \qquad \text{[kN/mm = MN/m]}$$

The Janβen joints in point A and B are modelled according to paragraph 3.3. The input is complete and the load bearing capacity according to the simple model can be determined.

$$\begin{aligned}\sigma_{2,\max,simple} &= 0.6188 MPa \\ \sigma_{2,\max,computer} &= 0.4836 MPa\end{aligned} \quad \rightarrow \quad \frac{\sigma_{2,\max,simple}}{\sigma_{2,\max,computer}} = \frac{0.6188}{0.4836} = 1.28$$

The simple model overestimates the load bearing capacity with 28%. This is an unsafe approximation.

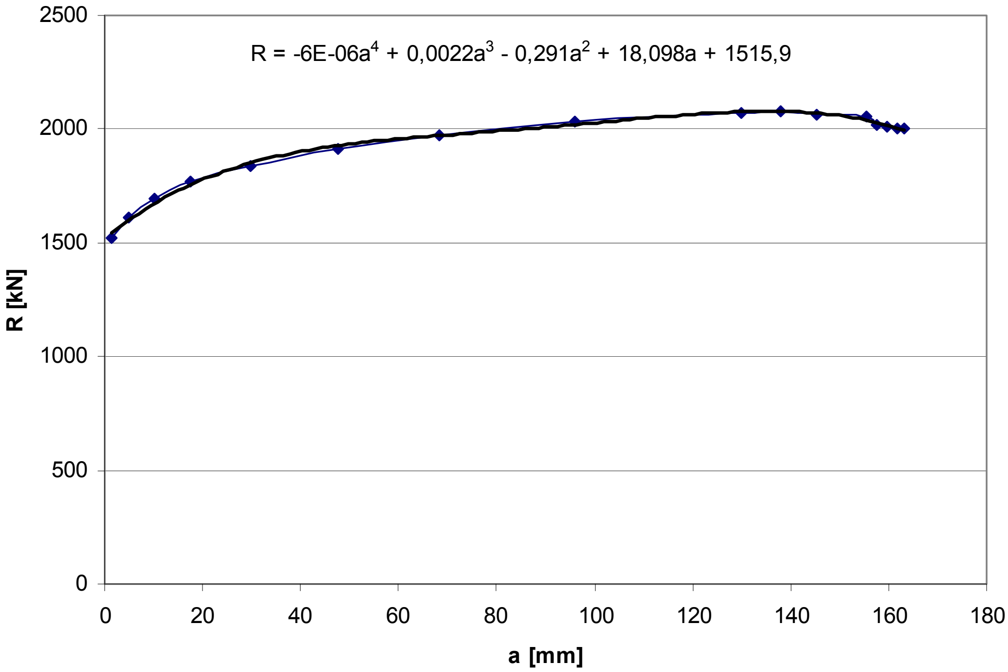

Figure 6.19 – R versus a, included a fourth order expression for R.

The simple model assumes an infinite stiff lining without curvature. In order to eliminate the inaccuracy as a consequence of the infinite stiff beam, the computer model for the Janβen failure is also calculated with infinite stiff segments. The expression for the spring k turns out to be a little bit different.

$$k = -0.000012a^3 + 0.0039a^2 - 0.4232a + 15.729 \quad \text{[MN/m]}$$

Again the load bearing capacity can be determined.

$$\begin{aligned} \sigma_{2,\max,simple} &= 0.5481 MPa \\ \sigma_{2,\max,computer} &= 0.5121 MPa \end{aligned} \quad \rightarrow \quad \frac{\sigma_{2,\max,simple}}{\sigma_{2,\max,computer}} = \frac{0.5481}{0.5121} = 1.07$$

The simple model overestimates the load bearing capacity with just 7%. One can conclude that the inaccuracy of the simple model regarding the stiffness of the segments is $28 - 7 = 21\%$. The remaining 7% inaccuracy is the result of the curvature which is neglected and the inaccurate determination of the function $\sigma_2(F)$. But, the approximation is still unsafe.

6.3.2 Segmental failure

The whole analysis for the segmental failure is almost the same as the Janβen failure analysis. From the computer model it turned out that $\beta = 13\pi/42$ (and $\varphi = 2\pi/21$). Secondly, the Janβen joint is point B is replaced by a rotational spring that represents plastic behaviour in the upper segment. A relation which is almost bi-linear (almost rigid plastic behaviour) is used for the $M-\theta$ diagram. Since Maple can only handle continuous functions, the bi-linear relation is simulated by the general function $M(\theta) = x \cdot \arctan(y \cdot \theta)$, in which x and y are constants. The constant y influences the stiffness and the constant x influences the bending moment capacity. The constant y must be a large number to obtain extreme high initial stiffness. The plastic behaviour starts if $\varepsilon_c = 1.75 \cdot 10^{-3}$, which means $M = 399.44 kNm$. Figure 6.20 shows the $M-\theta$ diagram for the Janβen joint in point A (blue line) and the segmental plastic behaviour in point B (red line). The spring stiffness k is determined according to the Janβen failure analysis, by using the corresponding computer model. Afterwards, the load bearing capacity can be determined.

$$k = -0.0008a^3 + 0.0678a^2 - 2.1962a + 44.1$$

$$\begin{aligned} \sigma_{2,\max,simple} &= 0.3611MPa \\ \sigma_{2,\max,computer} &= 0.3202MPa \end{aligned} \quad \rightarrow \quad \frac{\sigma_{2,\max,simple}}{\sigma_{2,\max,computer}} = \frac{0.3611}{0.3202} = 1.13$$

The simple model overestimates the load bearing capacity with 13%. The approximation for the load bearing capacity concerning the segmental failure performs more than twice as good than the Janβen failure approach (28% deviation). However, it is an unsafe approximation.

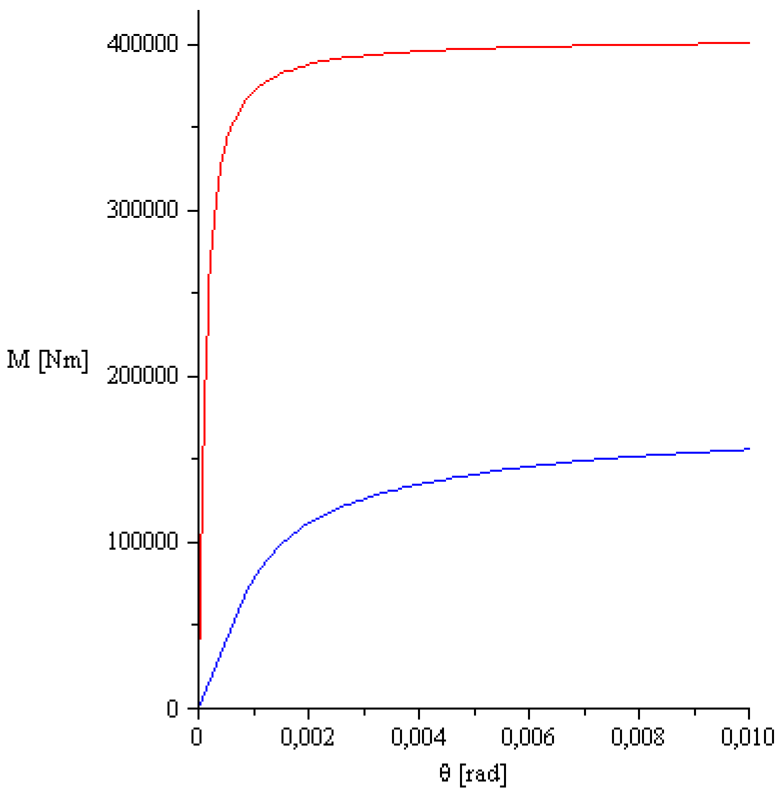

Figure 6.20 – M - θ diagram for the Janβen joint (blue line) and the segmental plastic behaviour (red line).

6.3.3 Initial soil stiffness

Until now, the spring stiffness k is determined by using the computer models. These models are not available in practice. So, this simple model needs a spring stiffness k which can be determined easily. The initial soil stiffness according to paragraph 3.4.2 is a very easy way. Only the horizontal component of the bedding in figure 6.21 is integrated for $0 \le \delta \le \pi/4$.

$$k = \int_0^{\pi/4} k_b \cos(\delta) d\delta \cdot r = \int_0^{\pi/4} \frac{E_{oed}}{r} \cos(\delta) d\delta \cdot r = \frac{E_{oed}}{r} r[\sin(\delta)]_0^{\pi/4} = \tfrac{1}{2}\sqrt{2} E_{oed}$$

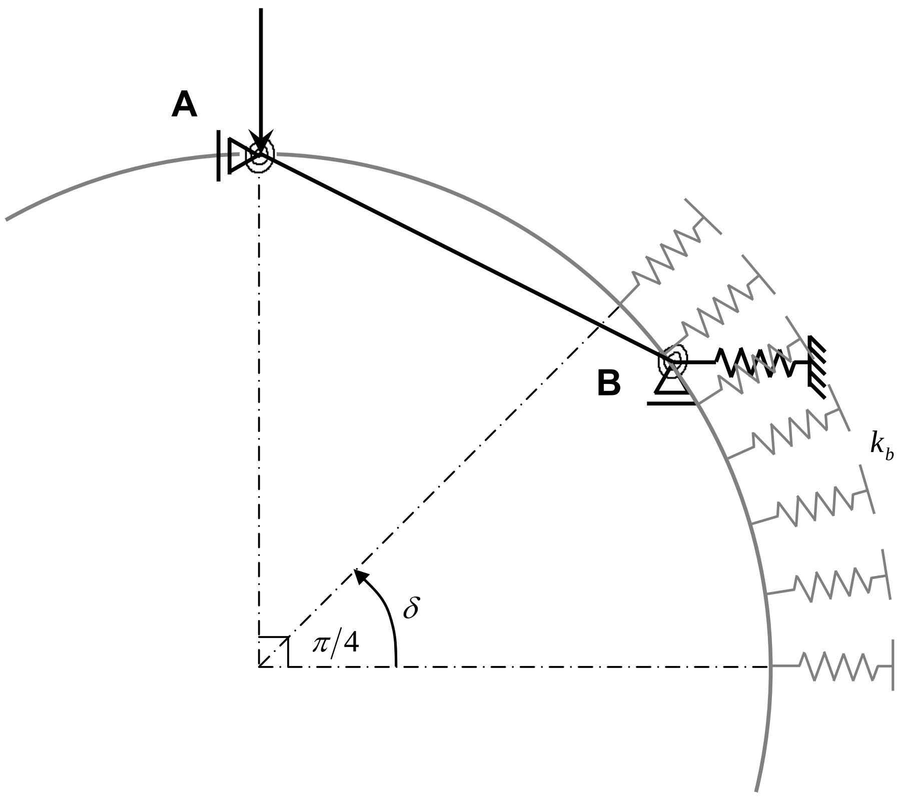

Figure 6.21 – The horizontal component of k_b is integrated for $0 \le \delta \le \pi/4$ to determine k.

The two possible situations according to table 6.3 will be analysed again by implementing the initial soil stiffness into the simple model. First, the load bearing capacity and the deviation for the Janβen failure will be determined. The simple model overestimates the load bearing capacity with 84%.

$$\sigma_{2,\max,simple} = 0.8884 MPa \quad \rightarrow \quad \frac{\sigma_{2,\max,simple}}{\sigma_{2,\max,computer}} = \frac{0.8884}{0.4836} = 1.84$$

Secondly, the load bearing capacity and the deviation for the segmental failure will be determined. The simple model underestimates the load bearing capacity with 19%. This is a safe approximation.

$$\sigma_{2,\max,simple} = 0.2581 MPa \quad \rightarrow \quad \frac{\sigma_{2,\max,simple}}{\sigma_{2,\max,computer}} = \frac{0.2581}{0.3202} = 0.81$$

One can conclude that using the initial soil stiffness provides a very simple model, but the results become less accurate. However, the assumption was made that the bedding is uniformly compressed. From the computer models it turned out that the bedding is not uniformly compressed, but more or less in a bi-linear shape (figure 6.22). The ratios seems to be valid in general. A small adjustment to the integrated reaction force from the bedding will increase accuracy a lot.

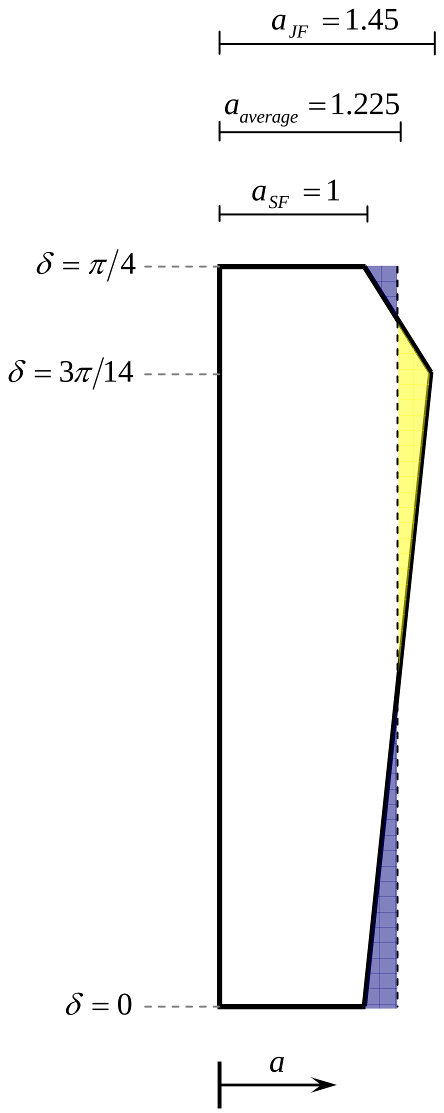

Figure 6.22 – The bedding is compressed in a bi-linear shape. JF = Janβen failure, SF = segmental failure.

In case of Janβen failure, the reaction force from the bedding is overestimated, since the average compression of the bedding is less than the specific compression at the location of the Janβen joint. Since the blue surface equals the yellow surface (figure 6.22), the reaction force must be divided by $1.2\ (\approx 1.45/1.225)$. The new load bearing capacity and corresponding deviation can be determined.

$$\sigma_{2,\max,simple} = 0.7514 MPa \quad \rightarrow$$

$$\frac{\sigma_{2,\max,simple}}{\sigma_{2,\max,computer}} = \frac{0.7514}{0.4836} = 1.55 \qquad \text{(55\% deviation)}$$

In case of segmental failure, it is just the other way around. The reaction force from the bedding is underestimated, since the average compression of the bedding is more than the specific compression at the location where the segment fails. Since the blue surface equals the yellow surface (figure 6.22), the reaction force must be multiplied by $1.2\ (\approx 1.225/1)$.

For convenience and consistency, the approach for the Janβen failure has been used as well in this case. The new load bearing capacity and corresponding deviation can be determined for the segmental failure as well.

$$\sigma_{2,\max,simple} = 0.2904 MPa \quad \rightarrow$$

$$\frac{\sigma_{2,\max,simple}}{\sigma_{2,\max,computer}} = \frac{0.2904}{0.3202} = 0.91 \qquad \text{(9\% deviation)}$$

6.3.4 Interpretation

This paragraph is about the practical value of the simplification to determine the load bearing capacity of a shield driven tunnel. In other words: the capability of the simplification to determine the load bearing capacity of a tunnel must be verified. The results from paragraph 6.3.3 were interpreted.

Literature explains that if $n = F_b / F \geq 10$ the first order calculation always suffices. Hence, when the buckling load F_b is at least ten times larger than the specified load F, the structural design will be safe from a stability point of view. If $n = 10$, the first order approach deviates just 11.1% from the real result, which is accepted since safety factors are used. This deviation can be explained by calculating the magnification factor for $n = 10$.

Magnification factor: $\frac{n}{n-1} = \frac{10}{10-1} = 1.11$ → 11.1% deviation

Figure 6.23 shows the deviation for many n values when using a first order calculation. If $n = 2$, the deviation is 100%. Hence, all displacements and internal forces are twice as big as the first order calculation predicted.

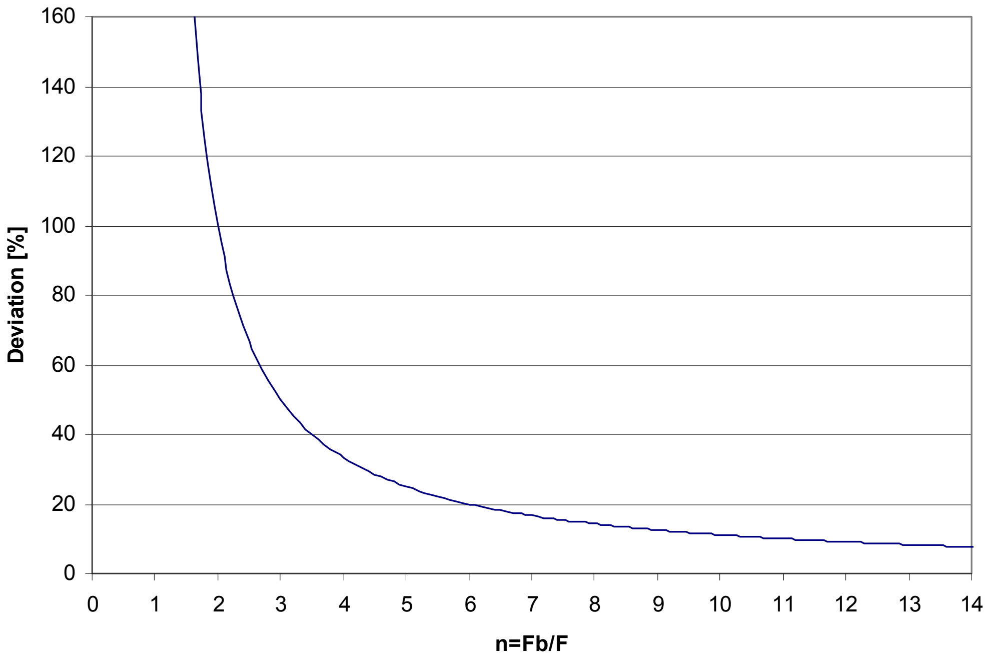

Figure 6.23 – Deviation from First order approach to reach equilibrium.

Dicke [10] tells in a practical way how the factor n should be interpreted.

- $n \leq 2$ Unacceptable; the structure is unstable.
- $2 < n \leq 5$ Dangerous; building a structure like this is highly discourage. Extensive non-linear analysis is required.
- $5 < n \leq 10$ Attention; a second order calculation is needed for a stable design. (Equilibrium must be based on deformed structure.)
- $n > 10$ Good; the structure is stable. A first order (LE) calculation suffices.

Therefore, a practical design should aim at $n \geq 10$. The simple model overestimates the collapse load with 55% if one analyses the Janβen failure. Hence, when the load bearing capacity is determined by using the simple model, the n value is not equal to ten, but $n = 6.45$. The n value for the Janβen failure according to the simple model is shown in figure 6.24.

The simple model underestimates the collapse load with 9% if one analyses the segmental failure. Hence, when the load bearing capacity is determined by using the simple model, the n value is not equal to ten, but $n = 10.99$. The n value for the segmental failure according to the simple model is shown in figure 6.24.

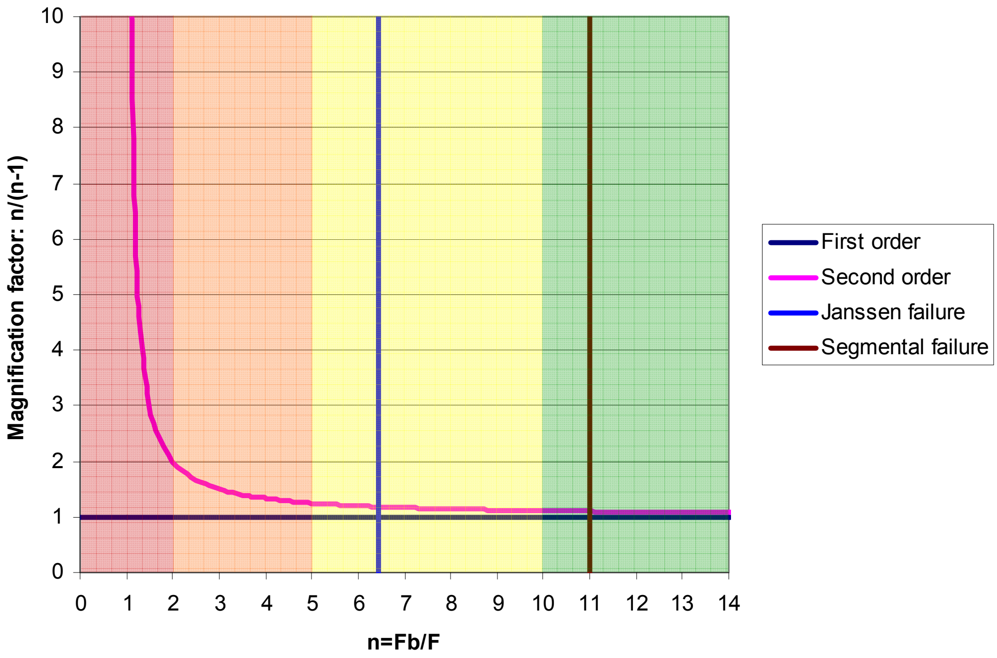

Figure 6.24 – Illustrative interpretation of the factor n according to Dicke.

For the situations in table 6.3 one can conclude that the simple model is able to indicate whether or not the tunnel is stable. Even without calibration the results are acceptable ($n > 5$; yellow and green area).

6.3.5 Recommendation for a practical procedure

As mentioned before, snap through failure can be induced by the Janβen joints or the segments. However, in practice it is unknown which one will be decisive in the end. In order to know the actual load bearing capacity of a specific case, it is important to develop a practical procedure which finds out the decisive snap through inducement.

The Janβen failure as well as the segmental failure must both be checked for a specific case. The definition for the function $\sigma_2(F)$, the Janβen characteristics for c_1 and c_2 (paragraph 3.3) and the expression for the spring stiffness k are similar for *both failure types*.

$\sigma_2(F) = 2F/r$ and $k = 1/2\sqrt{2}E_{oed}$

Other input parameters depend on the failure type under consideration. For the *Janβen failure* the initial angle φ (figure 6.4) depends on the location and the number of Janβen joints. This expression assumes that the first Janβen joint is located in the top of the ring.

$\varphi = \dfrac{\pi}{n}$ Where: n = Number of Janβen joints in one tunnel ring.

Secondly, the reaction force (R) in the translational spring must be divided by 1.2, since the reaction force from the bedding is overestimated.

For the *segmental failure* the initial angle φ is determined by the average place for which plastic behaviour starts to develop. In case of seven Janβen joints, the initial average angle $\varphi = 2\pi/21$. This is a very accurate definition, since all advanced computer analyses only show very small differences.

If the segmental failure is considered, the reaction force (R) in the translational spring must be multiplied by 1.2, since the reaction force from the bedding is underestimated.

Furthermore, in case of the segmental failure analysis, the Janβen joint in point B in replaced by a rotational spring which represents plastic behaviour in the upper segment. The bending moment capacity must be limited by the situation for which $\varepsilon_c = 1.75 \cdot 10^{-3}$. Note: this approach is most conservative. The $M - \theta$ relation for this new rotational spring in point B must be rigid plastic or nearly rigid plastic. Hence, an extreme high initial stiffness (almost infinite) must promptly change into extreme low stiffness (almost zero stiffness). This rapid stiffness change must occur at the bending moment for which the concrete strain equals $1.75 \cdot 10^{-3}$.

Finally, by using this practical procedure for this simple model, one obtains two different load bearing capacities. These two values must be divided by the corresponding calibration factor according to paragraph 6.3.3. The failure analysis corresponding to the lowest factored load bearing capacity is the decisive snap through inducement. This load bearing capacity can be used in tunnel design concerning snap through. For good stability, the specified load must be at least ten times smaller than this load bearing capacity ($n = F_b/F \geq 10$). So, the first order approach deviates just 11.1% of the real result. From a practical point of view this is acceptable since safety factors are used. Paragraph 6.3.4 gives a recommendation how to act if $n < 10$.

This practical procedure predicts the right snap through inducement for the specific situations in table 6.3.

7 CONCLUSIONS AND RECOMMENDATIONS

7.1 Conclusions

The discretised model with beam elements and non-linear rotational spring elements is not less accurate than the more accepted continuous model with only beam elements. The physical and geometrical non-linear model is able it provide knowledge about the ‘real’ structural behaviour of a shield driven tunnel surrounded by soil.

The normal force in the ring depends on the uniform pressure as well as the bedding. The bedding stiffness defines the relation between ring deformation and the increasing normal force. The normal force is completely determined by the soil properties (uniform loading and bedding stiffness). This is not surprisingly at all, since internal forces are always caused by the (external) loading.

The bending moment distribution depends on the corporation between the segments, the Janβen joints and the bedding. Actually, the bending moment distribution depends on the stiffness differences between the segments, the Janβen joints and the bedding. This is always the case when a statically indeterminate structure is considered. The magnitude of the bending moment is caused by the (external) loading.

The research question was: *“Are shield driven tunnels with large diameters more sensitive to snap through than smaller ones?*” The situation concerning snap through is worse than Blom [4] predicted. It turned out that the γ value is always close to one, instead of $\gamma = 3$ as Blom predicted for the BRT. Since γ is close to the critical point for snap through, a closer look at practical design methods was carried out to discover whether or not practical assumptions are still valid.

The radius is a quite robust parameter concerning snap through. Changing the radius of the tunnel will not influence safety a lot. However, the segmental thickness is an exponential parameter since a small change has large influence on safety. Despite the wrong results, the FL + GL (linear elastic) analysis turned out to be the safest approach for tunnel design. In case of changing radius, snap through will never occur before the bending moment capacity has been reached ($\lambda \approx 2$). In case of changing segmental thickness, the tunnel is safe if $d_{seg} > D_i/40$. More awareness of reality is required for everyone who uses the SL + JNL + GL (linear elastic with non-linear Janβen joints) analysis. For larger tunnel diameters ($r > 4m$) it is more likely that the analysis provides unsafe results. The same holds for segmental thicknesses outside the interval $1/38 < d_{seg}/D_i < 1/22$. A larger possibility exists that snap through takes place without any plastic hinge.

This research confirms the expectation that increasing the tunnel diameter has negative influence on safety of the design when using a practical way to analyse a shield driven tunnel. Hence, shield driven tunnels with large diameters are more sensitive to snap through than smaller ones. Since it is not unthinkable that snap through is the decisive failure mechanism, it is very dangerous if one realises that the practical methods to analyse a shield driven tunnel will not notice this failure mechanism. The tunnel design is probably based on the wrong criterion.

Additionally, this research confirms the correctness of the empirical design rule to determine the segmental thickness in relation to the radius. The reinforced concrete segments are used most efficient if $d_{seg} \approx D_i/22$.

The simplified model is a very practical and quite good tool to analyse snap through of shield driven tunnels. The model provides qualitative knowledge about the character of snap through and the load bearing capacity influenced by k, c_1, c_2 and r (soil, segments, longitudinal joints and the radius of the tunnel). Even without calibration, the simple model is able to indicate quantitative whether or not the tunnel is stable. After calibrating the simple model, it was possible to reveal a practical procedure to predict the right snap through inducement and corresponding load bearing capacity in no time.

7.2 Recommendations

During this research only the radius and the segmental thickness are studied in relation to snap through. In paragraph 2.1 all influencing parameters are introduced. The question remains whether or not these parameters are exponential or robust. For a complete statement about snap through and safety, the influence of these parameters must be analysed.

l_t	= Height of the Janβen joint
n	= Number of Janβen joint
$B\ value$	= Concrete strength
k_b	= Bedding stiffness (depends on E_{oed} and α_s)
σ_0	= Uniform loading

This research assumes that a single segmented ring is sophisticated enough to analyse snap through (paragraph 3.1). However, as a result of large deformations, peak forces will develop and load the segments, since the so-called dowel and socket system is activated (coupling forces). These coupling forces could have a positive effect on safety, since the tunnel rings support each other to bear the ovalisation loading. But, possibly these forces have negative influence on safety, since plastic hinges can develop very close to each other as a consequence of these large peak forces.

The results shown in chapter 4 are based on calculations with constant normal force. The software application Scia Engineer (as well as MatrixFrame) only offers a non-linear rotational spring with a custom relation between the rotation and bending moment. In order to analyse snap through, the ovalisation pressure is increased. Therefore, the bedding is activated and the normal force increases. Since the normal force is very important for the bending stiffness of the segments and the Janβen joints, it is recommended to create a normal force dependant model ($M - N - \theta$ relation). Extending the model from chapter 3 with normal force dependant structural behaviour will cause more convenience for the engineer and high accuracy of the results. Furthermore, it is recommended to check exactly the difference between the behaviour of the discontinuous model (with non-linear rotational springs) and the continuous model (with non-linear beam elements). The difference will probably be very small. However, in case of snap through, a small change in stiffness can influence results quite intensely.

Chapter 6 is about a simple model to analyse snap through. The results are calibrated and used for a practical procedure to determine the load bearing capacity. The simple model and the practical procedure perform very well. However, the conclusion is based on two specific cases. Since this simplification has high potential for practical usage, it is recommended to determine the calibration factors more accurate (based on many cases). Perhaps, one general calibration factor dependant on one or more of the parameters mentioned in paragraph 2.1 can be determined. A specific calibration factor for both snap through inducements (Janβen failure and segmental failure) is possible as well. In this case, the adapted calibration factors should be implemented into the practical procedure mentioned in paragraph 6.3.5.

REFERENCES

[1] Consortium DC-COB, December 2009, *Bezwijkveiligheid van boortunnels*.

[2] C.B.M. Blom, December 2009, *Concrete linings for shield driven tunnels.*

[3] C.B.M. Blom, 2002, Supplement to the Ph.D. Thesis “Design philosophy of segmented linings for tunnels in the soft soils”, Background document “Lining behaviour – analytical solutions of coupled segmented rings in soil”, Delft University of Technology 25.5-01-15.

[4] C.B.M. Blom, December 2002, *Design philosophy of segmented linings for tunnels in the soft soils*, dissertation, Delft University of Technology.

[5] Blom, C.B.M., A.P.M. Plagmeijer, *Boren van tunnels met niet-ronde vormen*. In: Cement № 6 2003, pages 74-80 (Dutch).

[6] T.W. Groeneweg, January 2007, *Shield driven tunnels in ultra high strength concrete*, master thesis, Delft University of Technology.

[7] T.G. van der Waart van Gulik, March 2010, *Snap through of large shield driven tunnels*, literature study for master thesis, Delft University of Technology.

[8] S.J. Lokhorst, 24 mei 2006, *COB-TC151 Literatuurstudie bezwijkveiligheid boortunnels vs1.0*, Movares Nederland B.V.

[9] A.C.W.M. Vrouwenvelder, February 2003, *CT5144 Structural stability*.

[10] D. Dicke, 1994 - 2005, *Stabiliteit voor ontwerpers*.

[11] A.C.W.M. Vrouwenvelder, March 2003, *Plastic Analysis of Structures*, Faculteit CITG.

APPENDICES

A Choosing an appropriate program

In order to answer the research question, numerical research has been carried out. A variety of sophisticated finite element programs and programs especially for frame analysis are available. All of them are more or less able to solve the problem; however, all programs have their specific advantages and disadvantages. Before starting this master thesis, I was not aware of the influence that the disadvantages or shortcomings of a specific program could have.

In contrast with the simplification in chapter 6, the numerical analysis toke a lot of time and caused a delay on the time schedule. The understanding of the mechanical behaviour of the system was not the reason for this, but the understanding of all different programs and dealing with their specific disadvantages was a time consuming issue during this thesis.

Since the master thesis is part of the study, from an educative point of view this delay is not that bad, since I learned a lot about many programs which are used by an engineer. In this appendix all these experiences are mentioned. A summary is given in table A.1.

In the beginning FX+ (pre-post processor) for DIANA was used. I had already some experience with this finite element program, since I passed the master course CT5148, Computational Modelling of Structures, for which **FX+ for DIANA** was used to solve some basic problems. It is a very advanced and scientific program. It is even possible to create your own element! In case of non-linear analysis, all sorts of data for every increment are given. Hence, not only the final situation, the intermediate stages can be interpreted as well. However, it is not very user-friendly. One is not able to put in all data by using FX+. To put in sophisticated data, like non-linear material properties, one must use the so-called MeshEditor. The final input for DIANA is a file with the extension ".dat" (data file) and is created by this external MeshEditor. The user is also allowed to change the data file directly by using the keyboard. If an error appears during the calculation it is almost impossible to delete this error, since there is hardly any information about the missing or incorrect data. In contrast with the FX+ manual, the DIANA manual is sufficiently good. If you are able to deal with these disadvantages, FX+ for DIANA is probably the best choice.

A quick try of modelling the structure was done by making use of **Dr. Frame**. This is actually a very simple program with a clear interface. It is not possible to apply curved beams, which is typical for a frame analysis program. A (plastic) hinge can only be modelled with a bilinear relation, which is not accurate enough to model a Janβen joint or a segment. The program is a bit unstable; it crashes frequently without any reason. There is also a bug in the program; for some reason it can not deal with the input when the unity cm has been used.

In the beginning **MatrixFrame** appears to be a quite good program to model the snap through problem for shield driven tunnels. The interface is very easy to use and the program is able to calculate FNL and GNL at the same time. But, later on it became clear that it has unacceptable disadvantages. The FNL + GNL calculations simply can not be combined with any other type of non-linear analysis (Janβen joint). During a GNL calculation, MatrixFrame assumes small rotations and small displacements (Appendix B).

The fourth program that was used is **Scia Engineer**. This is a very user-friendly program, but really extensive. It is impossible to simulate a Janβen joint. The dependency on the normal force can not be included. In case of non-linear analysis, Scia Engineer only shows the results of the last increment (final situation). This is not a big problem since many different load combinations can be calculated at the same time. The users' manual is very basic.

Program	Advantage	Disadvantage
FX+ for DIANA	• Advanced and scientific • Results per increment • DIANA manual	• Input in FX+ is very limited • Deleting errors is difficult • User-unfriendly • FX+ manual
Dr. Frame	• Simple program • Clear interface	• Only straight beams • Only linear or bilinear behaviour for (plastic) hinges • Unstable; it crashes frequently • Can not deal with the unity cm; that is a bug.
MatrixFrame	• User-friendly • Input very easy	• This program simply can not combine FNL + GNL with other types of non-linear analysis (longitudinal joints). • Is able to calculate GNL (second order), but assumes small rotations/displacement. • Only results of the last increment (final situation) are given.
Scia Engineer	• User-friendly • Input relatively easy • Very extensive (modelling and solver options)	• It is not possible to put in more than ten coordinates for a non-linear rotational spring. • Only results of the last increment (final situation) are given. • Very basic users' manual

Table A.1 – Summary of experience by using finite element programs.

B The essence of geometrical non-linear (GNL) calculations

In Chapter 6 the behaviour of the model in figure B.1 is derived. Figure B.2 shows graphically the behaviour of this model when realistic values for the stiffness parameters k, c_1 and c_2 were used. From paragraph 6.2 it turns out that, if $l = r$, the longitudinal joint stiffnesses c_1 and c_2 are relatively unimportant for the behaviour of the model. The soil stiffness k is very dominant. According to figure B.2, a real snap through character has been observed.

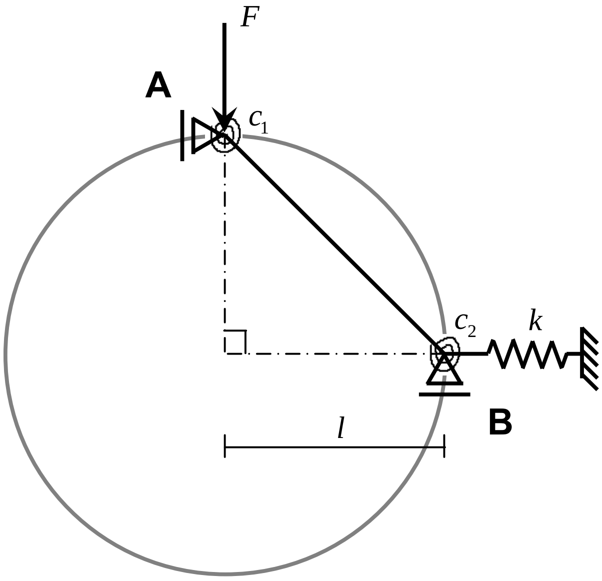

Figure B.1 – Model for the theoretical approach of the mechanism.

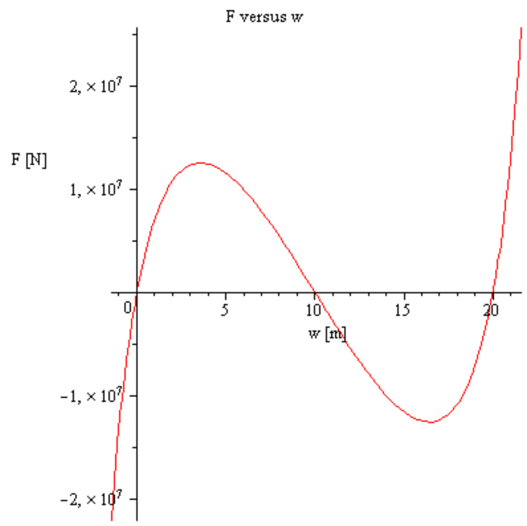

Figure B.2 – More realistic behaviour of the model. k = 9.5MN/m and c_1 and c_2 according to figure 6.8

After this analytical research, the program MatrixFrame was used, in order to simulate this snap through behaviour numerically. The student version of MatrixFrame, which was only available at that time, can only perform calculations based on linear elastic theory. The rotational springs, which represent the longitudinal joints, were not taken into account since they are relatively unimportant. To simulate the geometrical non-linear behaviour, the displacement of point A (figure B.1) was applied in ten equal steps. Every increment is equal to 1m displacement downwards. When a new step was modelled, the final geometry of the previous step was used, as well as the final force in the translational spring k.

After doing this exercise the result has showed the essence of geometrical nonlinear calculations. Figure B.3 shows the analytically calculated behaviour, while figure B.4 shows the numerically calculated behaviour. Both graphs of figure B.3 and B.4 have the same shape. But, two important differences are observed. First of all, the value for the force F is significantly higher in case of the numerical calculation. The second difference is the point of intersection with the horizontal axis. The latter is easy to explain. Since the force F in step i depends on the deformed geometry from step $i-1$, the curve from figure B.4 intersects the horizontal axis one step to "late". Hence, the force in the last step ($w = 11m$) is zero, since the deformed geometry of the beam in de second last step ($w = 10m$) is perfectly horizontal. If the beam is perfectly horizontal, it means that there is no possibility to obtain equilibrium when the vertical force F is not equal to zero. So, the force F must be zero, which is clearly indicated by the last step ($w = 11m$).

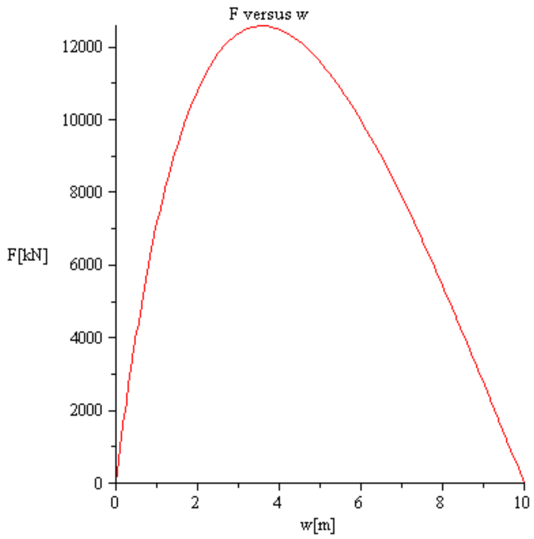

Figure B.3 – Analytically calculated behaviour, see also figure B.2. (continuous)

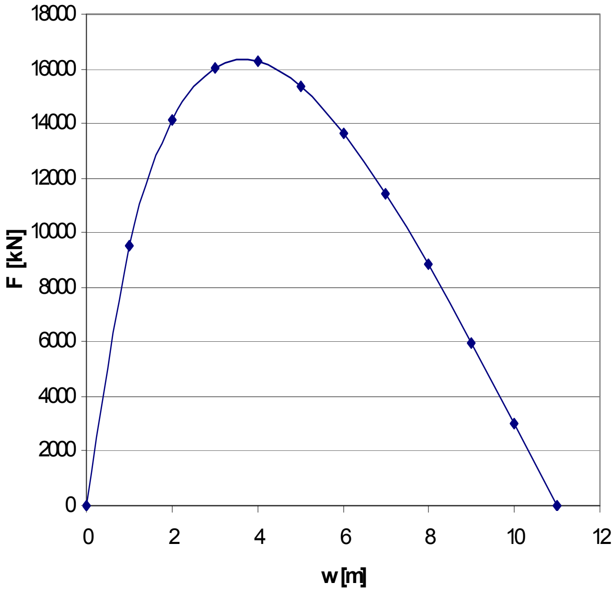

Figure B.4 – Numerically calculated behaviour (discrete, 10 equal displacement steps)

In fact, this is also the reason for the first mentioned difference. However, a more extensive explanation is given. The numerical GNL calculation is done in ten equal steps. But, every step in itself is a geometrical linear (GL) calculation. Hence, in all steps equilibrium of forces is based on the undeformed geometry (initial situation). When deformations are relatively large this becomes a problem for the accuracy of the results. This problem has shown in figure B.5. Point A is pushed downwards as a consequence of the prescribed displacement w. The beam becomes less steep and the translational spring starts to push back, since point B shifts to the right. In order to obtain equilibrium; the resultant reaction force in point B must be directed in the same direction as the beam ($\sum M = 0$) and the vertical component of the reaction force in point B must be equal to the force F ($\sum F_V = 0$). MatrixFrame uses the direction of the undeformed beam (grey) while the direction of the deformed beam (black) must be used. Hence, in reality the prescribed displacement w causes the vertical reaction force $B_{V,d}$ $(= F_{analytical})$, but MatrixFrame calculates $B_{V,ud}$ $(= F_{numerical})$. The latter is larger since the beam is steeper in the undeformed situation. This is indicated in figure B.5 by two closed force polygons, in which the reaction force from the soil has the same size in both force polygons ($B_{H,ud} = B_{H,d}$). This clarifies why the results from the numerical analysis are significantly higher than the results from the analytical analysis. The discretised (or numerical) solution is an approach of the continuous (or analytical) solution and will be more accurate when more steps (smaller increments) are applied.

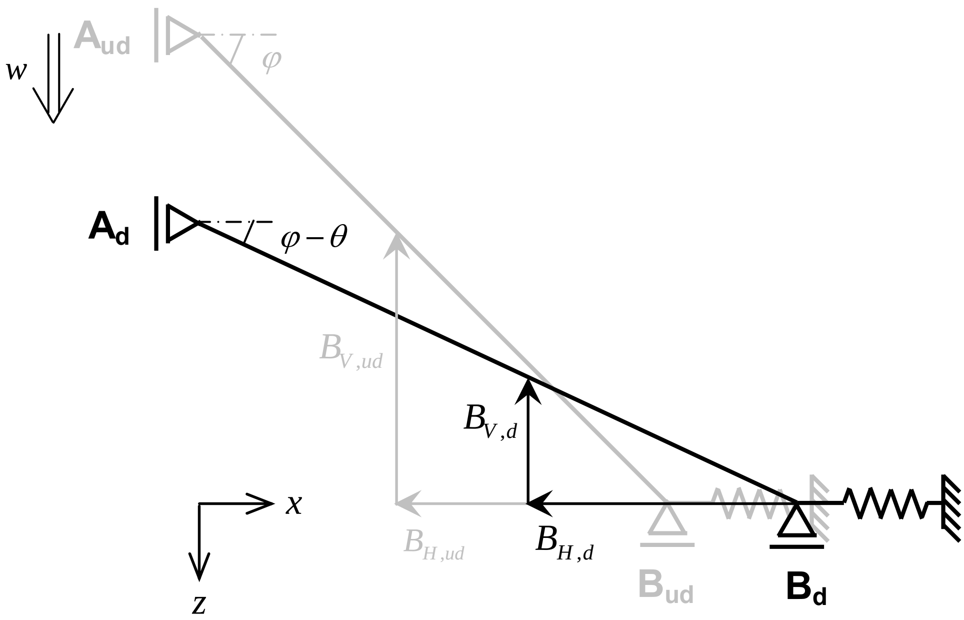

Figure B.5 – Equilibrium of forces based on the undeformed (ud) vs. the deformed (d) geometry for a curtain step i . Grey means undeformed and black means deformed.

MatrixFrame warns the user when deformations become larger than 1m, because the program assumes small deformations/displacements and small rotation angles ($\tan(\theta) \approx \theta$ and $\sin(\theta) \approx \theta$). (This assumption is very typical for linear elastic calculations.) This can be explained by analyzing the coordinates of point A and B in step 1 of table B.1. The coordinate system from figure B.5 is adopted. From the coordinates in step 0, the total length of the beam is calculated: $10\sqrt{2}m = 14{,}14m = \sqrt{200}m$ (Pythagoras). The length is a constant property, because the beam is infinitely stiff. The prescribed downwards directed displacement of point A is 1m in every step. Hence, the coordinate A_z has increased from -10m to -9m. Since one knows the total length of the beam and the length of one virtual rectangle side, the length of the other virtual rectangle side can be calculated by using Pythagoras again: $B_x = \sqrt{200 - 9^2} = 10.91m$. This value for B_x in step 1 is less than the value that MatrixFrame gave, because of the assumption of small deformations.

step	A		B		W	ΔF
	x	z	x	z		
0	0	-10	10,0000	0	0	0
1	0	-9	11,0000	0	1	9500
2	0	-8	11,8182	0	2	14132,23
3	0	-7	12,4951	0	3	16045,53
4	0	-6	13,0553	0	4	16260,67
5	0	-5	13,5149	0	5	15346,13
6	0	-4	13,8848	0	6	13653,65
7	0	-3	14,1729	0	7	11420,37
8	0	-2	14,3846	0	8	8816,85
9	0	-1	14,5236	0	9	5975,08
10	0	0	14,5925	0	10	3003,96
11	0	1	14,5937	0	11	0

Table B.1 – F vs. w and the coordinates of point A and B for all steps of the numerical calculation.

C $M-N-\kappa$ diagram (BRT)

Geometry (figure C.1)
- Cross-sectional area : $A_c = bh = 1000*400mm$ ($h = d_{seg}$)

Material data
- Concrete strength : B45
- Design value compressive strength : $f_{cd}^{'} = 0.6 f_{ck}^{'} = 0.6*45 = 27N/mm^2$
- Young's modulus concrete : $E_c = 22250 + 250 f_{ck}^{'} = 33500N/mm^2$
- α value compressive zone : 0.75 (B15 – B65)
- β value compressive zone : 0.389 (B15 – B65)
- Young's modulus steel : $E_s = 200000N/mm^2$
- Reinforcement area : $A_{s1} = A_{s2} = A_s = 648mm^2 (\omega_0 = \omega_{0,\min} = 0.18\%)$
- Design value tensile strength : $f_{yd} = 435N/mm^2$
- Ratio : $a/h = 0.1$ ($a = c + 0.5\phi = 35 + 0.5*10 = 40mm$)

Load
- Constant normal force (hoop force) : $N = \sigma_0 R = 0.5 \cdot 10^6 * 4.525 = 2262.5kN$

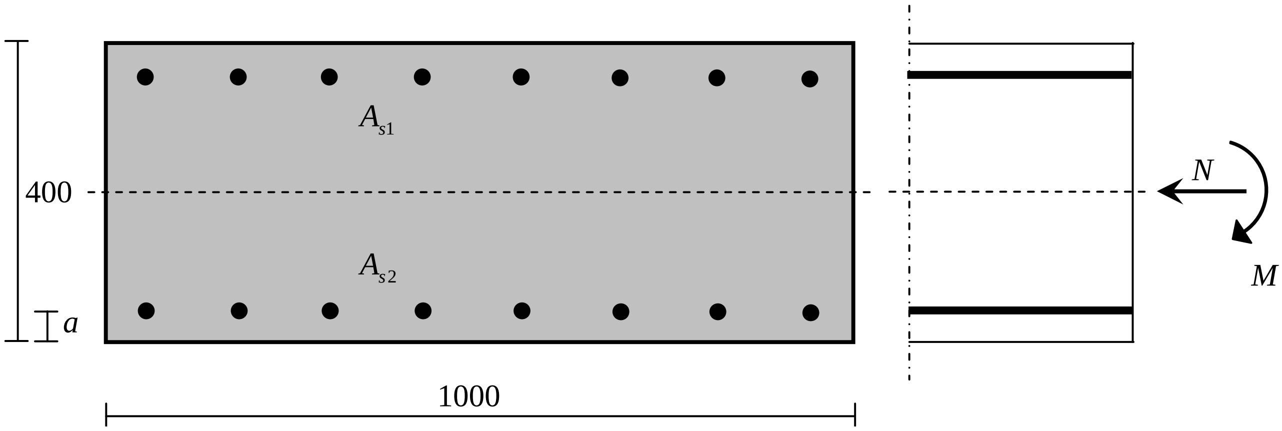

Figure C.1 – Reinforced concrete segment: cross-section and load

Especially in this case four situations must be analysed to determine the $M-N-\kappa$ diagram.

1) The fibre with the highest tensile stress; $\sigma_c = 0N/mm^2$.

2) The reinforcement on the tensile side of the cross-section; $\sigma_{s1} = 0N/mm^2$.

3) The design value for the compressive strength has been reached ($\varepsilon_c = 1.75 \cdot 10^{-3}$).

4) The ultimate limit state of the compressive zone has been reached ($\varepsilon_{cu} = 3.5 \cdot 10^{-3}$).

1) The fibre with the highest tensile stress; $\sigma_c = 0N/mm^2$

The deformations and stresses are given in figure C.2.

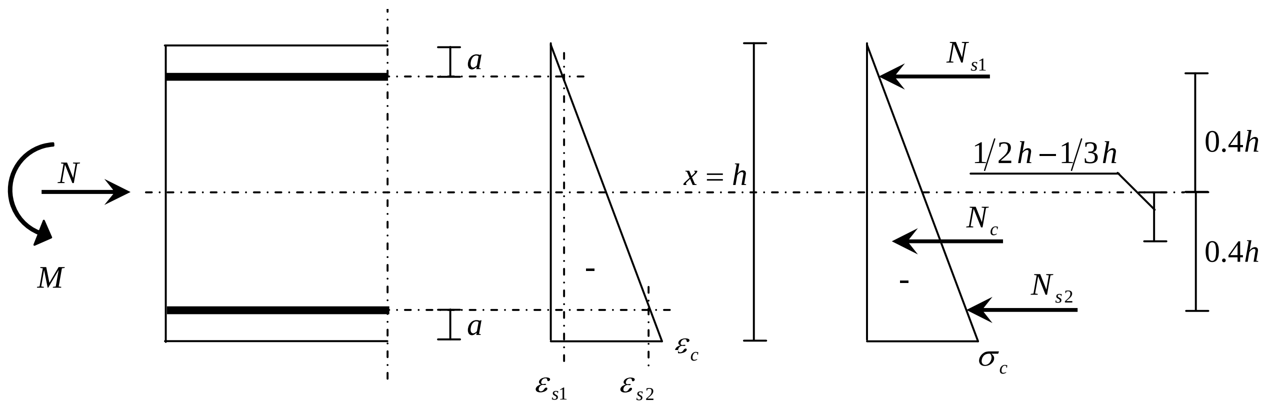

Figure C.2 – Deformations and stresses along the cross-section for situation 1.

The strains ε_{s1}, ε_{s2} and ε_c are three unknown parameters. But, ε_{s1} and ε_{s2} can be expressed in terms of ε_c.

$$\varepsilon_{s1} = \frac{0.1h * \varepsilon_c}{h} = 0.1\varepsilon_c \qquad \varepsilon_{s2} = \frac{(h - 0.1h) * \varepsilon_c}{h} = 0.9\varepsilon_c$$

To ensure equilibrium, the summation of horizontal forces must be equal to zero. From this equilibrium equation the unknown parameter ε_c can be determined.

$$N_{s1} = E_s A_s \varepsilon_{s1} = 200000 * 648 * 0.1\varepsilon_c = 12960000\varepsilon_c$$
$$N_{s2} = E_s A_s \varepsilon_{s2} = 200000 * 648 * 0.9\varepsilon_c = 116640000\varepsilon_c$$
$$N_c = 0.5bhE_c\varepsilon_c = 0.5 * 1000 * 400 * 33500 * \varepsilon_c = 6700000000\varepsilon_c$$

$\sum N = 0$ → $N = N_{s1} + N_{s2} + N_c$

$$2262.5 \cdot 10^3 = (12960000 + 116640000 + 6700000000)\varepsilon_c$$
$$\varepsilon_c = 3.313 \cdot 10^{-4}$$

Check:

$$N_{s1} = 12960000 * 3.313 \cdot 10^{-4} = 4293.4N$$
$$N_{s2} = 116640000 * 3.313 \cdot 10^{-4} = 38640.3N$$
$$N_c = 6700000000 * 3.313 \cdot 10^{-4} = 2219566.3N$$
$$N = N_{s1} + N_{s2} + N_c$$
$$2262500 = 4293.4 + 38640.3 + 2219566.3 \text{ (OK)}$$

The assumption was made that the reinforcement at both sides of the segment does not yield. This must be verified before the results are used in the next calculation.

$$\varepsilon_{s1} = 0.1\varepsilon_c = 0.1 * 3.313 \cdot 10^{-4} = 3.313 \cdot 10^{-5} < \frac{f_{yd}}{E_s} = \frac{435}{200000} = 2.175 \cdot 10^{-3} \text{ (OK)}$$

$$\varepsilon_{s2} = 0.9\varepsilon_c = 0.9 * 3.313 \cdot 10^{-4} = 2.982 \cdot 10^{-4} < \frac{f_{yd}}{E_s} = \frac{435}{200000} = 2.175 \cdot 10^{-3} \text{ (OK)}$$

To ensure equilibrium, the summation of moments must be equal to zero as well. The equilibrium of moments is verified with respect to symmetrical axis of the cross-section.

$$M = N_c\left(\tfrac{1}{2}h - \tfrac{1}{3}h\right) + \left(N_{s2} * 0.4h\right) - \left(N_{s1} * 0.4h\right)$$
$$M = 2219566.3 * \left(200 - \tfrac{400}{3}\right) + \left(38640.3 * 0.4 * 400\right) - \left(4293.4 * 0.4 * 400\right) = 153.47 \cdot 10^6\ Nmm$$

The corresponding curvature can be determined very easy.

$$\kappa = \frac{\varepsilon_c}{h} = \frac{3.313 \cdot 10^{-4}}{400} = 8.282 \cdot 10^{-7}\ mm^{-1}$$

2) The reinforcement on the tensile side of the cross-section; $\sigma_{s1} = 0 N / mm^2$
The deformations and stresses are given in figure C.3.

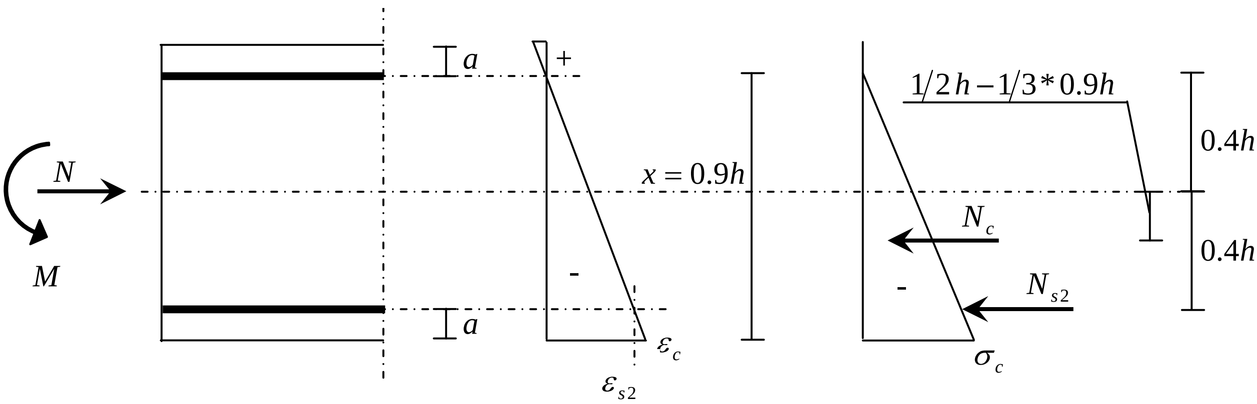

Figure C.3 – Deformations and stresses along the cross-section for situation 2.

In this situation, there are only two unknown parameters: ε_{s2} and ε_c. Again, ε_{s2} can be expressed in terms of ε_c.

$$\varepsilon_{s2} = \frac{h - 2 * 0.1h}{h - 0.1h}\varepsilon_c = \frac{0.8}{0.9}\varepsilon_c$$

To ensure equilibrium, the summation of horizontal forces must be equal to zero. From this equilibrium equation the unknown parameter ε_c can be determined.

$$N_{s2} = E_s A_s \varepsilon_{s2} = 200000 * 648 * \frac{0.8}{0.9}\varepsilon_c = 115200000\varepsilon_c$$
$$N_c = 0.5b * \left(0.9h\right) * E_c \varepsilon_c = 0.5 * 1000 * 0.9 * 400 * 33500 * \varepsilon_c = 6030000000\varepsilon_c$$

$$\sum N = 0 \quad \rightarrow \quad N = N_{s2} + N_c$$

$$2262.5 \cdot 10^3 = (115200000 + 6030000000)\varepsilon_c$$

$$\varepsilon_c = 3.682 \cdot 10^{-4}$$

Check:

$$N_{s2} = 115200000 * 3.682 \cdot 10^{-4} = 42413.6N$$

$$N_c = 6030000000 * 3.682 \cdot 10^{-4} = 2220086.4N$$

$$N = N_{s2} + N_c$$

$$2262500 = 42413.6 + 2220086.4 \text{ (OK)}$$

The assumption was made that the reinforcement at both sides of the segment does not yield. This must be verified before the results are used in the next calculation.

$$\varepsilon_{s1} = 0\varepsilon_c = 0 * 3.682 \cdot 10^{-4} = 0 < \frac{f_{yd}}{E_s} = \frac{435}{200000} = 2.175 \cdot 10^{-3} \text{ (OK)}$$

$$\varepsilon_{s2} = \frac{0.8}{0.9}\varepsilon_c = \frac{0.8}{0.9} * 3.682 \cdot 10^{-4} = 3.273 \cdot 10^{-4} < \frac{f_{yd}}{E_s} = \frac{435}{200000} = 2.175 \cdot 10^{-3} \text{ (OK)}$$

To ensure equilibrium, the summation of moments must be equal to zero as well. The equilibrium of moments is verified with respect to symmetrical axis of the cross-section.

$$M = N_c\left(\tfrac{1}{2}h - \tfrac{1}{3} * 0.9h\right) + (N_{s2} * 0.4h)$$

$$M = 2220086.4 * \left(200 - \frac{0.9 * 400}{3}\right) + (42413.6 * 0.4 * 400) = 184.39 \cdot 10^6\, Nmm$$

The corresponding curvature can be determined very easy.

$$\kappa = \frac{\varepsilon_c}{0.9h} = \frac{3.682 \cdot 10^{-4}}{0.9 * 400} = 1.023 \cdot 10^{-6}\, mm^{-1}$$

3) The design value for the compressive strength has been reached ($\varepsilon_c = 1.75 \cdot 10^{-3}$ *)*

The deformations and stresses are given in figure C.4.

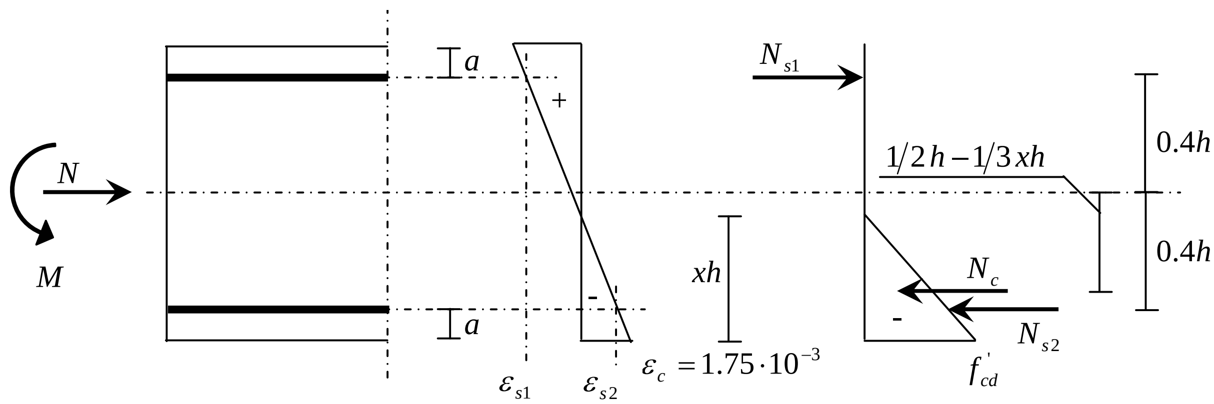

Figure C.4 – Deformations and stresses along the cross-section for situation 3.

The strains ε_{s1}, ε_{s2} and ε_c are again three unknown parameters. The strains ε_{s1} and ε_{s2} can be expressed in terms of ε_c.

$$\varepsilon_{s1} = \frac{0.9h - xh}{xh}\varepsilon_c = \frac{0.9 - x}{x}\varepsilon_c \qquad \varepsilon_{s2} = \frac{xh - 0.1h}{xh}\varepsilon_c = \frac{x - 0.1}{x}\varepsilon_c$$

To ensure equilibrium, the summation of horizontal forces must be equal to zero. From this equilibrium equation the unknown parameter ε_c can be determined.

$$N_{s1} = E_s A_s \varepsilon_{s1} = 200000 * 648 * \frac{0.9 - x}{x} * 1.75 \cdot 10^{-3} = 226800 \frac{0.9 - x}{x}$$
$$N_{s2} = E_s A_s \varepsilon_{s2} = 200000 * 648 * \frac{x - 0.1}{x} * 1.75 \cdot 10^{-3} = 226800 \frac{x - 0.1}{x}$$
$$N_c = 0.5bxhE_c\varepsilon_c = 0.5 * 1000 * x * 400 * 27 = 5400000x$$

$$\sum N = 0 \quad \rightarrow \quad N = N_{s2} + N_c - N_{s1}$$
$$2262.5 \cdot 10^3 = 226800 \frac{x - 0.1}{x} + 5400000x - 226800 \frac{0.9 - x}{x}$$
$$x = 0.4322$$

Check:

$$N_{s1} = 226800 \frac{0.9 - 0.4322}{0.4322} = 245518.2N$$
$$N_{s2} = 226800 \frac{0.4322 - 0.1}{0.4322} = 174320.2N$$
$$N_c = 5400000 * 0.4322 = 2333698.0N$$
$$N = N_{s2} + N_c - N_{s1}$$
$$2262500 = 174320.2 + 2333698 - 245518.2 \text{ (OK)}$$

The assumption was made that the reinforcement at both sides of the segment does not yield. This must be verified before the results are used in the next calculation.

$$\varepsilon_{s1} = \frac{0.9 - x}{x}\varepsilon_c = \frac{0.9 - 0.4322}{0.4322} * 1.75 \cdot 10^{-3} = 1.894 \cdot 10^{-3} < \frac{f_{yd}}{E_s} = \frac{435}{200000} = 2.175 \cdot 10^{-3} \text{ (OK)}$$
$$\varepsilon_{s2} = \frac{x - 0.1}{x}\varepsilon_c = \frac{0.4322 - 0.1}{0.4322} * 1.75 \cdot 10^{-3} = 1.345 \cdot 10^{-3} < \frac{f_{yd}}{E_s} = \frac{435}{200000} = 2.175 \cdot 10^{-3} \text{ (OK)}$$

To ensure equilibrium, the summation of moments must be equal to zero as well. The equilibrium of moments is verified with respect to symmetrical axis of the cross-section.

$$M = N_c\left(\tfrac{1}{2}h - \tfrac{1}{3}xh\right) + \left(N_{s2} * 0.4h\right) + \left(N_{s1} * 0.4h\right)$$
$$M = 2333698.0 * \left(200 - \frac{0.4322 * 400}{3}\right) + \left(174320.2 * 160\right) + \left(245518.2 * 160\right) = 399.44 \cdot 10^6 \, Nmm$$

The corresponding curvature can be determined very easy.

$$\kappa = \frac{\varepsilon_c}{xh} = \frac{1.75 \cdot 10^{-3}}{0.4322 * 400} = 1.012 \cdot 10^{-5} mm^{-1}$$

4) The ultimate limit state of the compressive zone has been reached ($\varepsilon_{cu} = 3.5 \cdot 10^{-3}$ *)*
The deformations and stresses are given in figure C.5.

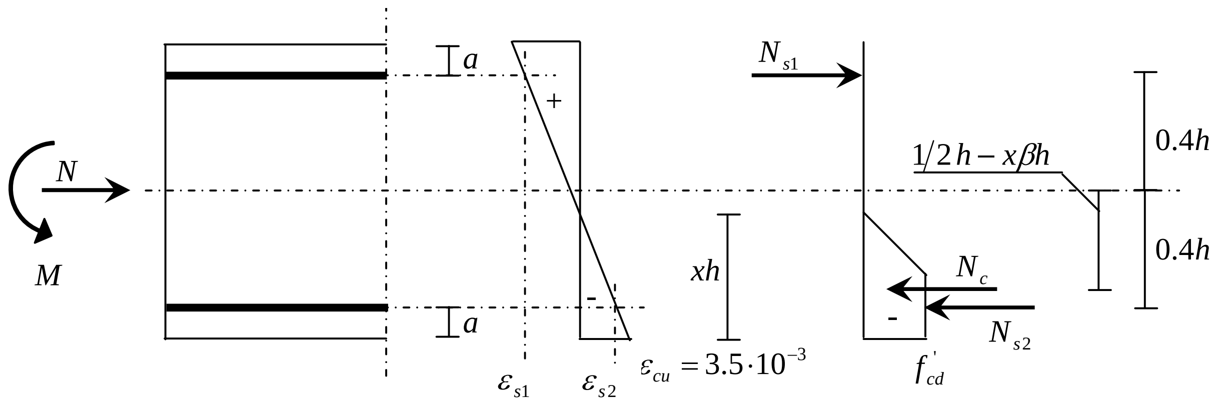

Figure C.5 – Deformations and stresses along the cross-section for situation 4.

To avoid brittle failure, the reinforcement must yield before the compressive zone crushes. So, the minimum amount of reinforcement ($\omega_0 = 0.18\%$) is applied. Especially in the ultimate limit state the assumption was made that the reinforcement at both sides of the segment does yield. To ensure equilibrium, the summation of horizontal forces must be equal to zero.

$$N_{s1} = f_{yd} A_s = 435 * 648 = 281880 N$$
$$N_{s2} = f_{yd} A_s = 435 * 648 = 281880 N$$
$$N_c = \alpha b x h f'_{cd} = 0.75 * 1000 * x * 400 * 27 = 8100000 x$$

$$\sum N = 0 \quad \rightarrow \quad N = N_{s2} + N_c - N_{s1}$$
$$2262.5 \cdot 10^3 = 281880 + 8100000x - 281880$$
$$x = 0.2793$$

The assumption was made that the reinforcement at both sides of the segment does yield. This must be verified before the results are used in the next calculation.

$$\varepsilon_{s1} = \frac{0.9h - xh}{xh} \varepsilon_{cu} = \frac{0.9 - 0.2793}{0.2793} * 3.5 \cdot 10^{-3} = 7.777 \cdot 10^{-3} > \frac{f_{yd}}{E_s} = 2.175 \cdot 10^{-3} \text{ (OK)}$$
$$\varepsilon_{s2} = \frac{xh - 0.1h}{xh} \varepsilon_{cu} = \frac{0.2793 - 0.1}{0.2793} * 3.5 \cdot 10^{-3} = 2.247 \cdot 10^{-3} > \frac{f_{yd}}{E_s} = 2.175 \cdot 10^{-3} \text{ (OK)}$$

To ensure equilibrium, the summation of moments must be equal to zero as well. The equilibrium of moments is verified with respect to symmetrical axis of the cross-section.

$$M = N_c\left(\tfrac{1}{2}h - \beta xh\right) + \left(N_{s2} * 0.4h\right) + \left(N_{s1} * 0.4h\right)$$
$$M = 8100000 * 0.2793 * \left(200 - 0.389 * 0.2793 * 400\right) + 2 * \left(281880 * 0.4 * 400\right) = 444.37 \cdot 10^6\ Nmm$$

The corresponding curvature can be determined very easy.

$$\kappa = \frac{\varepsilon_{cu}}{xh} = \frac{3.5 \cdot 10^{-3}}{0.2793 * 400} = 3.133 \cdot 10^{-5}\ mm^{-1}$$

$M - N - \kappa$ diagram

Table C.1 is an overview of the relations between the bending moment and the deformation. Figure C.6 is the corresponding diagram. The diagram is valid for a normal (or hoop) force of 2262.5kN.

Moment (M) [kNm]	**Kappa** (κ) [mm^{-1}]	**Bending stiffness** ($EI = M/\kappa$) [kNm^2]
153.47	$8.282 \cdot 10^{-7}$	185305
184.39	$1.023 \cdot 10^{-6}$	180244
399.44	$1.012 \cdot 10^{-5}$	39470
444.37	$3.133 \cdot 10^{-5}$	14184

Table C.1 – M - κ relation and the corresponding bending stiffness for a constant normal force of 2262.5kN (BRT)

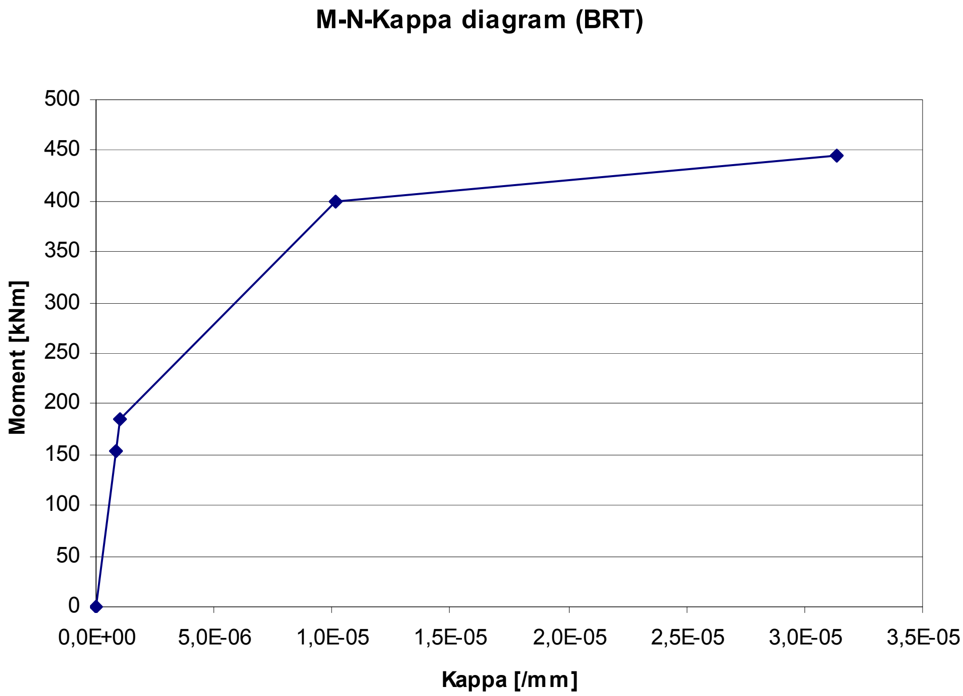

Figure C.6 – M - N - κ relation for a constant normal force of 2262.5kN (BRT).

D Janβen joint

The analytical solution for the rotational stiffness of a longitudinal joint is expressed by two formulas, each corresponding to a specific situation. Figure D.1 shows a Janβen joint and some definitions.

1) As long as the stress due to the compressive normal force (hoop force) is larger than the maximum stress due to the bending moment, the rotational stiffness is constant and the joint is closed. Hence, there is no gap in the joint: the rotational stiffness is constant (not depending on the occurring rotation in the joint).

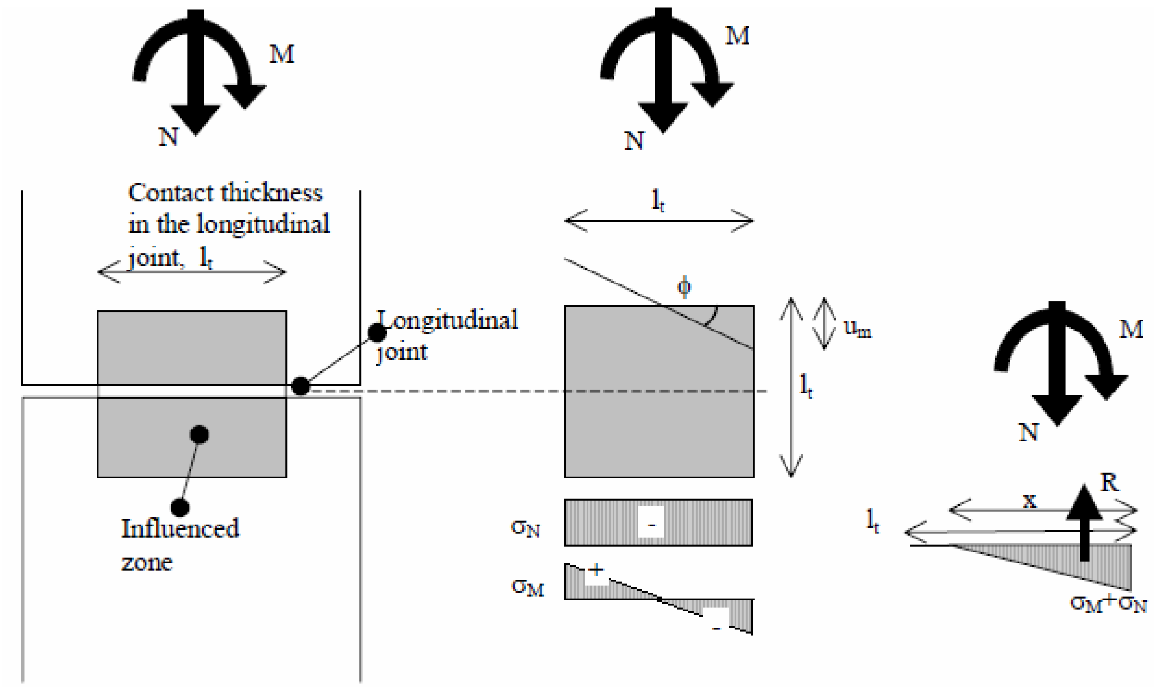

Figure D.1 – Longitudinal joint with the contact thickness l_t and the influenced zone.

The maximum stress in the influenced zone due to the bending moment:

$$\sigma_M = \frac{M}{W} = \frac{6M}{bl_t^2} \tag{1}$$

The maximum strain in the influenced zone due to the bending moment:

$$\varepsilon_M = \frac{\sigma_M}{E_c} \tag{2}$$

The deformation in the influenced zone due to this strain:

$$u_M = \varepsilon_M l_t \tag{3}$$

The relative rotation of the influenced zone:

$$\phi = \frac{2u_M}{l_t} \tag{4}$$

Substitution of (1), (2) and (3) in (4) will result in:

$$\phi = \frac{12M}{E_c l_t^2 b} \tag{5}$$

The mathematical relation between the tangential bending moment and the rotation is:

$$M = c_r \phi \qquad \Leftrightarrow \qquad c_r = \frac{M}{\phi} \tag{6}$$

Substitution of (5) in (6) results in the constant rotational stiffness:

$$c_r = \frac{b l_t^2 E_c}{12} \tag{7}$$

It is obvious that the constant stiffness is only influenced by the Young's modulus of the concrete and the contact surface in the longitudinal joint.

2) A gap will develop if the normal force is out of the neutral force centre of the joint's cross-section. The developed tensile stress due to the bending moment exceeds the compression stress due to the normal force. If this is happening a gap starts to develop and the rotational stiffness will also depend on the rotation itself and becomes non-linear. The bending stiffness of the ring reduces even more. Hence, there is a gap in the joint: the rotational stiffness is reducing as a function of the rotation. Equation (8) shows the condition for this second stage. Equation (10) is a more specific condition for the second stage.

$$\sigma_M \geq \sigma_N \tag{8}$$

The stresses due to the normal forces are:

$$\sigma_N = \frac{N}{b l_t} \tag{9}$$

Substitution of (1) and (9) in (8) results in the limit for which the gap occur:

$$M \geq \frac{N l_t}{6} \tag{10}$$

Hence, if this condition is fulfilled, the rotational stiffness will also be depending on the rotation.

There must be a normal force equilibrium at all time:

$$\sum N = 0 \qquad \Leftrightarrow \qquad N = R \tag{11}$$

For the reaction force R is written:

$$R = \frac{\sigma b x}{2} \tag{12}$$

Substitution of (12) in (11) will give:

$$x = \frac{2N}{\sigma b} \tag{13}$$

There must be bending moment equilibrium at all time:

$$\sum M = 0 \qquad \Leftrightarrow \qquad M + N\frac{x}{3} - \frac{N l_t}{2} = 0 \tag{14}$$

Substitution of (13) in (14) will give:

$$\frac{1}{\sigma} = \frac{-3 b l_t}{4N}\left(\frac{2M}{N l_t} - 1\right) \tag{15}$$

The acting strains can be derived from:

$$\varepsilon = \frac{\sigma}{E_c} \tag{16}$$

The deformation u is related to the strains by:

$$u = \varepsilon l_t \tag{17}$$

The rotation of the influenced zone as relation of the deformation is:

$$\phi = \frac{u}{x} \tag{18}$$

Substitution of (13), (15), (16) and (17) in (18):

$$\phi = \frac{8N}{9bl_t E_c \left(\frac{2M}{Nl_t} - 1 \right)^2} \tag{19}$$

De reducing rotational stiffness is derived by substituting (19) in (6):

$$c_r = \frac{9bl_t E_c \left(\frac{2M}{Nl_t} - 1 \right)^2}{8N} M \tag{20}$$

From the equations (19) en (20) it is clear that the rotation has a non-linear relation with to the bending moment; the rotational stiffness is non-linear. When the bending moment is known the rotational stiffness can be determined easily. However, when the rotation is known, the rotational stiffness is more complex to determine. The analytical solutions are based on force equilibrium. The solution for the rotational stiffness as function of the rotation is not given here.

E Maple sheets

E.1 Load versus displacement

> $restart;$

> $E_{oed} := 38e6:$

> $k := 0.5\sqrt{2}E_{oed}:$

> $r := 4.525:$

> $\varphi := \frac{\pi}{7}:$

> $l := r \cdot \cos\left(\frac{\pi}{2} - 2\varphi\right):$

> $m := \frac{l}{\cos(\varphi)}:$

> $a := m \cdot \cos(\varphi - \theta) - l:$

> $h := m \cdot \sin(\varphi):$

> $w := m \cdot \sin(\varphi) - m \cdot \sin(\varphi - \theta):$

> $R := k \cdot a:$

> $M_1 := 220000 \arctan(1400\theta):$

> $M_2 := 220000 \arctan(1400\theta):$

> $F := \frac{M_1 + R \cdot (h - w) + M_2}{l + a}:$

> $plot\left(\left[w, F, \theta = 0..\frac{\pi}{3.2}\right], title = \text{"F versus w"}, labels = [\text{"w[m]"}, \text{"F[N]"}, color = [red]\right);$

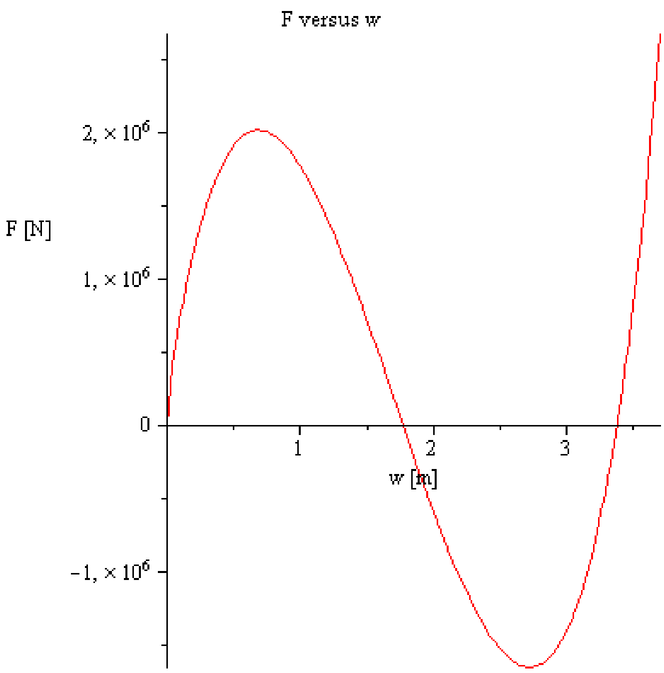

E.2 Janβen joint

This Maple sheet must be used to simulate a Janβen joint or to create a plastic hinge by using the function $M(\theta)=x\cdot\arctan(y\cdot\theta)$. The result is the input for M_1 and/or M_2 mentioned in the Maple sheet in appendix E.1.

> $restart;$

> $M := c_0\cdot\theta:$

> $$eq := c_0 = \frac{9\cdot b\cdot l_t\cdot E\cdot\left(\frac{2\cdot M}{N\cdot l_t}-1\right)^2}{8\cdot N}\cdot M:$$

> $solve(\{eq\},\{c_0\});$

$$\{c_0=0\},\left\{c_0=\frac{1}{6}\,\frac{\left(3bE\theta l_t+2\sqrt{2}\sqrt{bENl_t\theta}\right)N}{bE\theta^2}\right\},\left\{c_0=\frac{1}{6}\,\frac{\left(3bE\theta l_t-2\sqrt{2}\sqrt{bENl_t\theta}\right)N}{bE\theta^2}\right\}$$

> $$c := \text{'}if\text{'}\left(\theta<\frac{2\cdot N}{E\cdot b\cdot l_t},\frac{b\cdot l_t^2\cdot E}{12},\frac{1}{6}\cdot\frac{\left(3\cdot b\cdot E\cdot\theta\cdot l_t-2\cdot\sqrt{2}\cdot\sqrt{b\cdot E\cdot N\cdot l_t\cdot\theta}\right)\cdot N}{b\cdot E\cdot\theta^2}\right):$$

> $N := 2262500:$

> $b := 1:$

> $E := 15000000000:$

> $l_t := 0.340:$

> $plot([220000\arctan(1400\theta), c\cdot\theta], \theta=0..0.01, y=0..400000,$
> $title=\text{"Janβen joint"}, labels=[\text{"θ[rad]"},\text{"M[Nm]"}], color=[red,blue]);$